HIGH RESOLUTION LITHOGRAPHY-COMPATIBLE MICRO-ELECTRO-DISCHARGE MACHINING OF BULK METAL FOILS FOR MICRO-ELECTRO-MECHANICAL SYSTEMS

by

Mark Thomas Richardson

A dissertation submitted in partial fulfillment
of the requirements for the degree of
Doctor of Philosophy
(Electrical Engineering)
in The University of Michigan
2009

Doctoral Committee:

Professor Yogesh B. Gianchandani, Chair
Professor Khalil Najafi
Professor Albert J. Shih
Professor Kensall D. Wise

To my family, old and new.

ACKNOWLEDGEMENTS

I am grateful for the love and support given by so many people over the years. My family: Mom, Dad, and Keith, aunts, uncles, and cousins have always been there in every way. For my grandparents, who inspired me to work hard and become an engineer.

To Radhika- I couldn't have imagined a better way to close one chapter and begin a new one in our lives together. Thank you for sharing this *jo*urne*y* with me.

Thank you to my friends and coworkers in the YG group, EECS, and everywhere else, especially my officemates. Working, hanging out, and traveling with you all were some of my best memories from this experience. Snow storms in Istanbul, karaoke in Kobe, beach soccer at Hilton Head, mopeds in Greece, hiking through cacti, the finer things and tea time; these all don't have meaning without you.

For my committee: Prof. Wise and Najafi, for starting the WIMS center which has been a huge positive influence in both my education and career; Prof. Shih for your insight and flexibility.

Finally, I want to acknowledge all the opportunities that Prof. Gianchandani has given me over the years. It has been a privilege to work closely with him starting with undergraduate research through completing a Ph.D.

This work was supported in part by the National Science Foundation (NSF), the NSF Wireless Integrated Microsystems Engineering Research Center (WIMS-ERC), Sandia National Laboratories, and the University of Michigan. I appreciate the work done by the staff at each of these organizations who ease the burden of every grad student.

TABLE OF CONTENTS

LIST OF FIGURES

LIST OF TABLES

LIST OF APPENDICES

ABSTRACT

HIGH RESOLUTION LITHOGRAPHY-COMPATIBLE MICRO-ELECTRO-DISCHARGE MACHINING OF BULK METAL FOILS FOR MICRO-ELECTRO-MECHANICAL SYSTEMS

by

Mark Thomas Richardson

Chair: Yogesh B. Gianchandani

The application of batch mode micro-electro-discharge machining (μEDM) to the fabrication of micro-electro-mechanical systems has opened the door to lithographically compatible precision machining of all bulk metals. High volume applications in biomedical, communications, and consumer electronics devices are enabled by this technology. This dissertation explores the capabilities, limitations, and further improvement of high density batch mode μEDM. There are four parts to this effort described below.

A machining resolution study of high density features in stainless steel identifies the design space. Lithographically fabricated copper tools with single cross, parallel line, and circle/square array features of 5-100μm width and 5-75μm spacing were used. The observed discharge gap varies with shape, spacing, and feature location from 3.8-8μm.

As tool feature density is increased, debris accumulation effects begin to dominate, eventually degrading both tool and workpiece.

Two new techniques for mitigating this debris build-up are separately investigated. The first is a silicon passivation coating which suppresses spurious discharges triggered from the sidewalls of the machining tool. By this method, for high density batch machining, mean tool wear rate decreases from a typical rate of about 34% to 1.7% and machining non-uniformity reduces from 4.9μm to 1.1μm across the workpiece. The second involves a two-step machining process that enhances the hydraulic removal of machining debris and therefore throughput.

Wireless RF signals are inherently emitted by the micro-discharge process. This thesis describes the first reported wireless detection of debris accumulation during μEDM, enabling direct monitoring of machining quality in real time with 5dBm signal drop. The first wireless detection of the interface between two stacked metals during μEDM is also reported giving a 10dBm signal change. The technique enables direct monitoring of the discharge without the influence of terminal parasitics.

Finally, the first study of the residual stress due to the recast layer left behind by μEDM is presented. The recast layer stress-thickness product ranged from 0.5-6 GPa-μm for discharge energies from 0.03-20μJ. The recast layer thickness ranges from 0.2-3.3μm. Low energy discharges allow precision microstructures to be fabricated from bulk metals. Application of μEDM technology to RF switches and stents is in the appendices.

CHAPTER 1

INTRODUCTION

The application of lithographically based microfabrication techniques to the manufacture of traditionally machined devices has many benefits. From reduced size, improved reliability, and systems integration to increased throughput, lower cost, and fundamental science advances; Micro-Electro-Mechanical Systems (MEMS) devices such as accelerometers, pressure sensors, and digital micro-mirrors have all blossomed from tools originally designed for silicon CMOS processes. While each of these devices represent advances over their predecessors, the tools used to fabricate them have inherent limitations in material selection that prevent further application to other devices.

Devices requiring thick patterns of metal are especially challenging. For example, the contact resistance of a communications device like an RF switch is affected by the choice in material used as well as its shape [Cou06]. Biomedical devices for implantation such as stents also have limited options for material selection due to biocompatibility requirements. Titanium, platinum, and stainless steel are the most common metal implant materials. They are machined with traditional methods such as Computer Numerical Control (CNC) milling, lasers, and Electrical Discharge Machining (EDM) depending on shape and resolution requirements. This work investigates lithographically compatible techniques for micromachining bulk metal MEMS devices.

The first section is a historical perspective on micro-electrodischarge machining (μEDM). In section 1.2, the other bulk metal micromachining technologies are presented and compared using a variety of metrics. Next, in section 1.3 some of the applications for high resolution bulk metal micromachining are presented. Finally, section 1.4 identifies the challenges in high density batch μEDM that are addressed in the rest of this thesis.

1.1 Micro-Electrodischarge Machining

Micro-electrodischarge machining uses controlled, sequential, spark discharges between a tool and workpiece in a dielectric fluid to pattern microstructures with any conductive material [Mas90, Ho03]. These include non-traditional bulk materials that are typically difficult to machine such as stainless steel, tungsten carbide cobalt, and permalloy. Stainless steel in particular is one of the few materials which are biocompatible, enabling use in medical implants. Feature sizes down to 5 μm with a position accuracy of 0.1 μm are possible [Sma09]. Typical uses for serial μEDM are to precision drill high aspect ratio holes for fuel injector nozzles or ink-jet printer nozzles, mould and die manufacture, and various aerospace and surgical components.

Sir Joseph Priestley first observed metal erosion by spark discharges as early as 1768 [McGe88]. Low frequency arc discharges were eventually used for removal of broken drills and taps. Electrodischarge machining as a fabrication technique has been utilized for more than 65 years. In 1943, B.R. and N.I. Lazarenko realized that controlled spark discharges in a dielectric oil, which caused wear on switch contacts they were investigating, could be used for machining [McGe88]. They developed a relaxation

circuit to control the discharge energy and the first application of EDM was for machining hard materials since Russia did not have a large supply of suitable diamonds for milling at the time. Conventional tools were retrofitted with RC spark generators in the 1950s but had limited removal rates.

A 9 µm hole machined in 50 µm thick cemented carbide alloy by T. Masuzawa in 1967 brought EDM into microfabrication [McGe02]. Controlling the discharge energy by keeping the stray capacitances to the 100 pF range was the key. Greater understanding of the principles of operation emerged in the 1970s and 80s along with servo control and CNC operation. Wire electrodischarge grinding made generating 5 µm diameter tungsten tools a repeatable process [Mas90, Masu85]. Pulse generator circuits improved throughput for large scale roughing operations but the best surface finishes were and still are obtained with the RC circuit. The first flushing techniques for debris removal were also developed in this time period. Batch mode die-sinker EDM had also been investigated by this time but could not achieve the same tolerances as serial mode [McGe88].

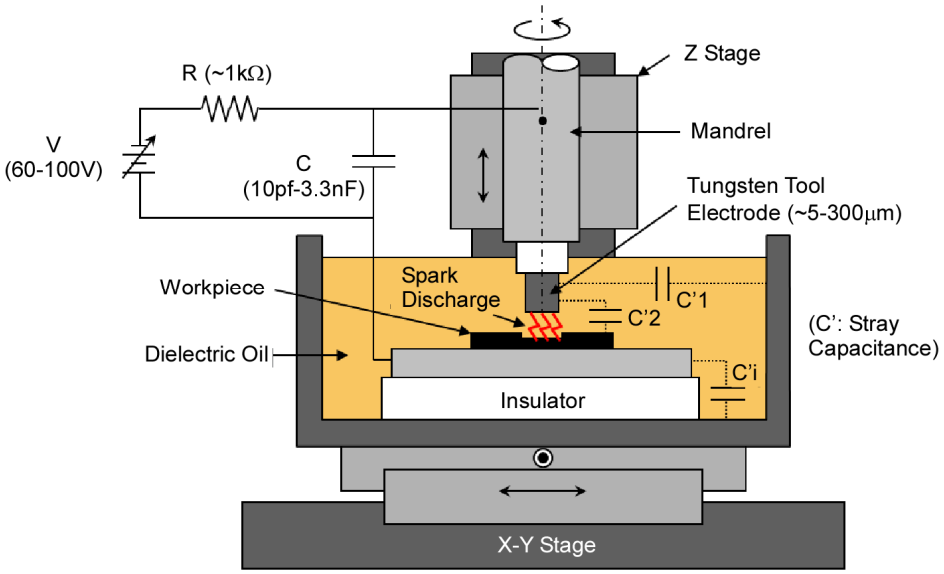

Fig. 1-1: Electrical configuration and setup for µEDM adapted from [Tak05].

Today, while traditional serial μEDM has good feature resolution, it has limited throughput. The configuration for the Panasonic MG-ED72 μEDM is shown in Fig. 1-1 [Tak05]. A sharpened wire tip is scanned across the surface of the workpiece while immersed in a dielectric oil medium to define the pattern. The discharge gap adds a machining tolerance of 1-3 μm to the tool diameter depending on the selected discharge energy [Tak05]. It would be beneficial to take the advantages of serial μEDM, e.g. material selection and feature size, and blend them with the advantages of a lithographic process, e.g. high throughput.

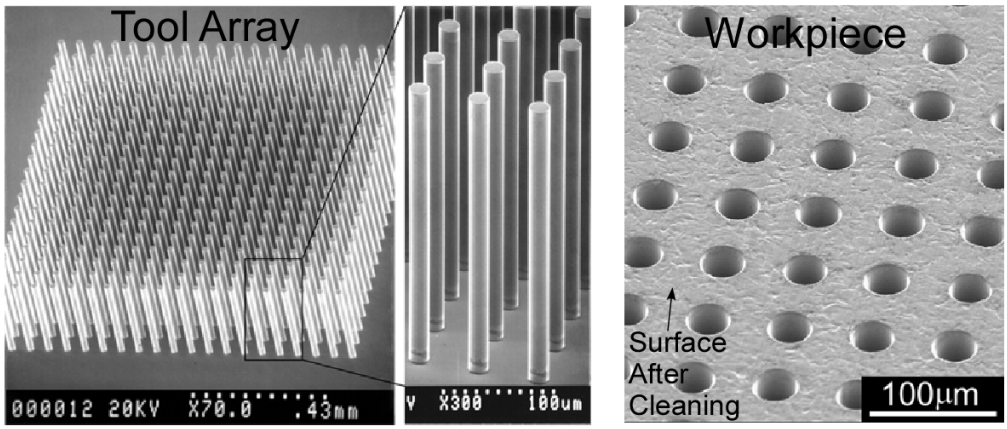

Fig. 1-2: Left: Electroplated copper tools for batch μEDM fabricated by LIGA. Right: Resulting stainless steel workpiece after machining [Tak05].

Batch mode μEDM uses lithographically patterned metal, as cookie-cutter type tools to machine many features in parallel. In the late 1990s LIGA (Lithographie Galvanoformung Abformung) processing enabled tall, high aspect ratio electroplated metal structures which could be used for batch mode μEDM (Fig. 1-2) [Ehr96, Koch00, Tak05]. By utilizing multiple discharge circuits connected to segmented electrode arrays, batch mode can increase throughput by up to 100x over serial mode [Tak02].

A theoretical model for these multiple discharge circuits in batch μEDM was developed by Takahata using an SCR model for the spark discharge and parasitic elements between adjacent circuits (Fig. 1-3) [Hu80, Tak05]. The discharge voltage is set by the SCR breakdown voltage while the arc voltage is set by the Zener diode. The current and voltage pulse shapes are defined by R_p and L_p which are found by fitting to measured signal traces. The RC_e timing circuit originally proposed by Lazarenko is used to control the discharge energy of each individual circuit. The capacitors C_{p1a-f} are parasitic capacitors that cause crosstalk between adjacent circuits. The parasitics also lower the pulse freqeuency from 3.4 MHz to 1.8 MHz and increase the peak current by almost 3x, which causes higher surface roughness and thicker recast. The additional capacitance can be used to replace C_e and lower the discharge energy to the expected levels. Signal traces for an 80 V 100 pF discharge are shown in Fig. 1-4. The discharge model will be discussed further in chapter three for debris dominated machining.

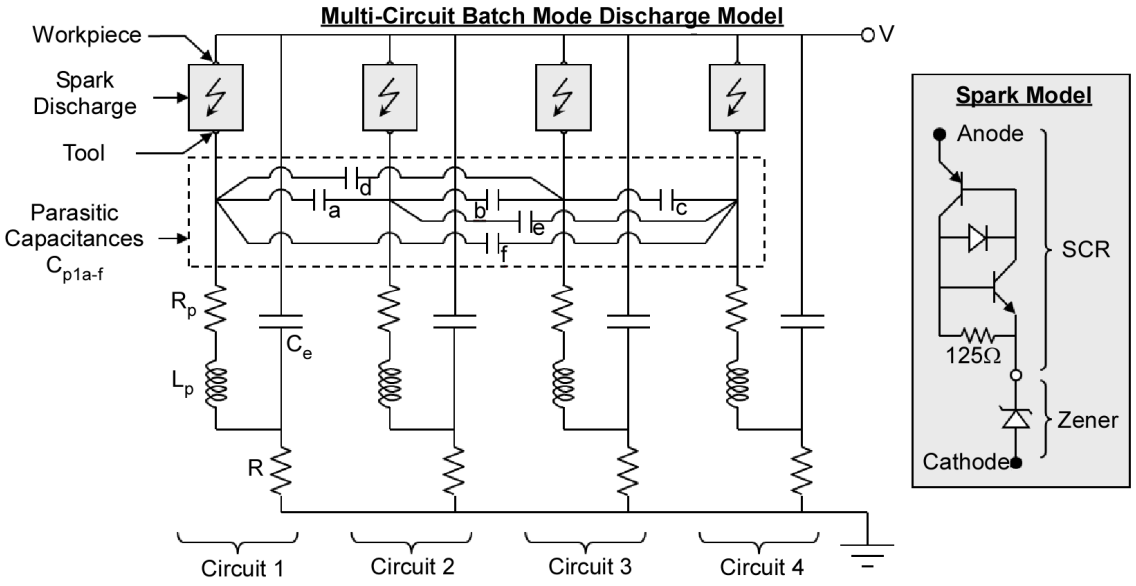

Fig. 1-3: Theoretical model for multiple circuit batch μEDM has parasitic capacitances between adjacent circuits. Adapted from [Tak05].

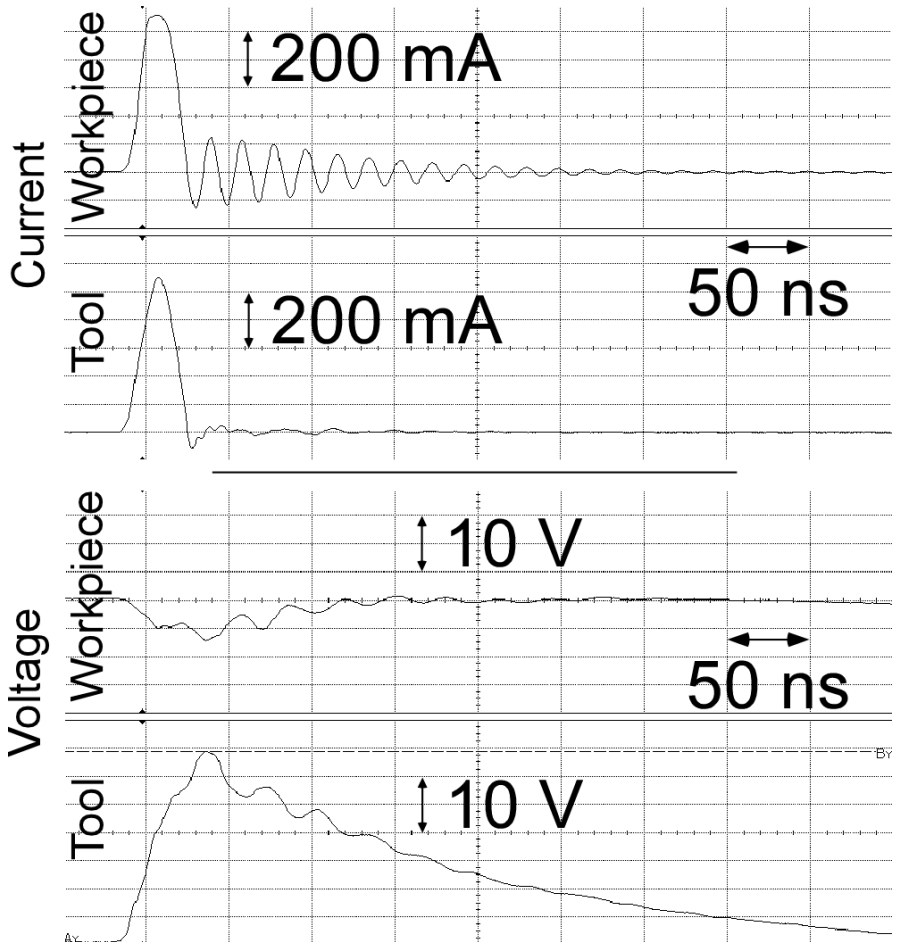

Fig. 1-4: Typical current and voltage probe measurements of μEDM discharges with 80V 100pF discharge energy.

In the last few years, SU-8 UV LIGA processing in our group has enabled relatively tall (100 μm) electroplated metal structures to be processed without the use of expensive synchrotron X-ray radiation sources (Fig. 1-5) [Ude06]. The current challenge in batch mode μEDM that this work addresses is in machining high feature densities and large patterns to achieve high throughput with small feature sizes.

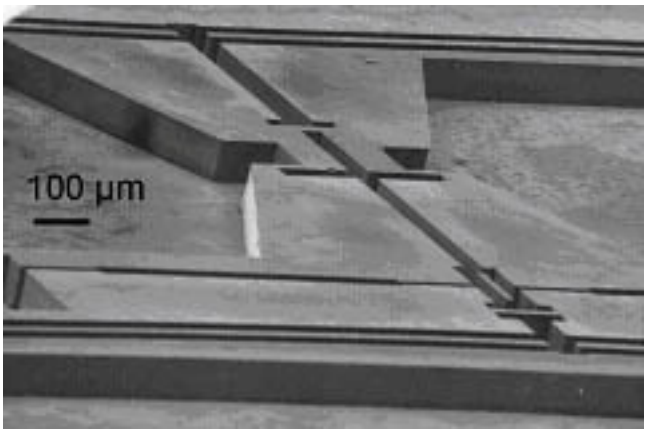

Fig. 1-5: An SU-8 UV LIGA electroplated copper tool is 100 µm tall with 10 µm minimum features has a 10:1 aspect ratio.

1.2 Comparison of Micromachining Technologies

All fabrication processes can be classified by the addition or subtraction material, serial or parallel operation, mechanism of operation, and by minimum feature size. In general, processes that add material require careful process characterization and control to ensure consistent material properties. Material selection is constrained by the chemistry of the deposition process and often by diffusion constants as feature sizes decrease. Examples of additive processes are electroforming e.g. LIGA and masked thin film deposition e.g. sputtering, evaporation, and chemical vapor deposition (CVD).

Subtractive processes, in contrast, follow the material properties of the bulk material. For example, the material properties of devices fabricated by masked wet etching of bulk silicon are very close to the original silicon. Bulk material properties are easier to control than a deposited material but may vary at the location of machining. Thermal processes such as EDM and laser machining leave a residual heat affected zone. Mechanical processes such as Computer numerical control (CNC) micro-milling may leave significant residual stress. Precision micromachining of bulk metals widens the material

suite to alloys such as platinum-rhodium, stainless steel, and tungsten-carbide cobalt that are not practical with an additive process.

The primary benefit of using batch (lithographic) processes is that many devices can be fabricated in parallel, increasing throughput. However, the material selection of metals and precision for most lithographic processes such as masked wet etching, plasma etching and LIGA (electroforming) are limited by chemistry. A comparison of many traditional and non-traditional machining methods is shown in Fig. 1-6 [Bro98, El-Ho05, Tak05].

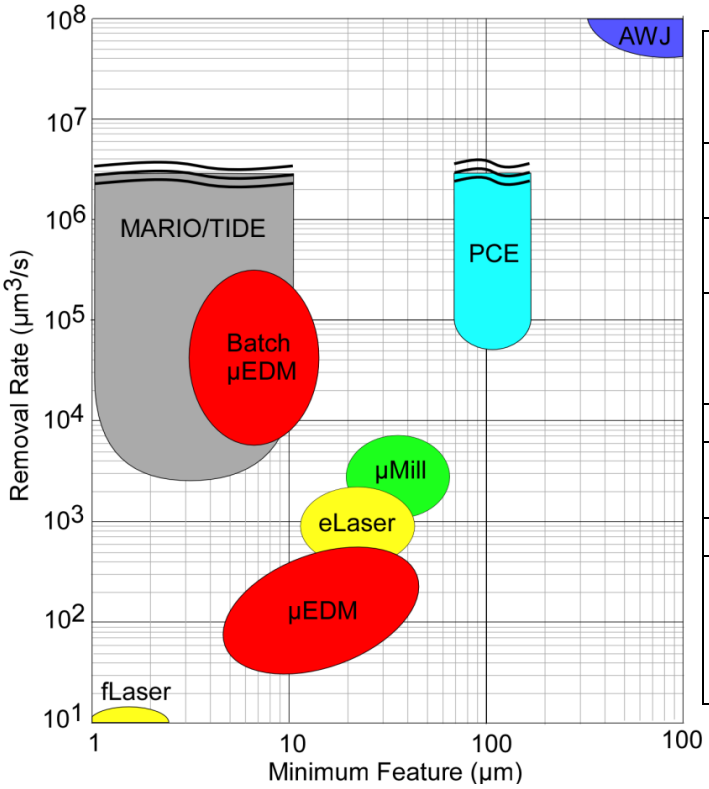

AWJ	Akk09, Bro98, Chap02, El-Ho05
eLaser	Chap02, El-Ho05, Tak05
fLaser	El-Ho05, San07, Tak05
µEDM	Bro98, Chap02, El-Ho05, Kur08, Tak05
Batch µEDM	Tak02, Tak05
µMill	Chap02, Fri96, Tak05
MARIO/TIDE	Aim04, Park05
PCE	Bro98, Chap02, El-Ho05, McGe88, Rao07

Fig. 1-6: Performance map of tradition serial micromachining techniques for bulk metals. Batch mode µEDM increases throughput by 100x over serial mode µEDM and is lithographically compatible. PCE and MARIO also have very high removal rates.

Wet etching of metals is isotropic, limiting the maximum depth and aspect ratio for photochemical etching (PCE). The metal anisotropic reactive ion etching with oxidation (MARIO) and titanium inductively coupled plasma deep etch (TIDE) processes can etch bulk titanium with high aspect ratio but not other metals [Aim04, Park05]. They are both similar to deep reactive ion etching (DRIE) in that they use plasma enhanced etching cycled with passivation of the sidewalls. Like other DRIE processes, throughput is scalable to several wafers at a time and so removal rate is dependent on the specific pattern. This is also true for PCE and is accounted for in the comparison of Fig. 1-6. LIGA is limited to materials that can be electroplated or molded. Photochemical etching has a wide range of material options but is also limited in resolution to around 0.7x the sample thickness. For a 100 μm thick sample this is 70 μm.

Serial processes are inherently slower than parallel techniques for complex patterns since each feature is traced out sequentially but are still in use because they can offer benefits in other areas such as minimum feature size and material selection. For example, laser machining has excellent minimum feature size (~100s of nm) and since it is a thermal process, can be used with many materials. However, the material removal rate is much lower for small features and materials with large thermal coefficients and/or high reflectivity. Computer numerical control (CNC) micro-milling physically removes material but imparts a significant residual stress on the workpiece and suffers from fast tool wear for hard materials. As can be seen, the serial processes in the lower half of Fig. 1-6 have a tradeoff between minimum feature size and material removal rate.

Abrasive water jet (AWJ) does not suffer from low material removal rate, but is limited to about 300 μm minimum feature size. High pressure water mixed with abrasive

granules focused with a small nozzle is used to erode the workpiece. It is most effective for ceramics and brittle materials but can be used on metals. The machinery requires regular maintenance because of the steady buildup of debris from the workpiece and machining fluid coupled with the high pressure components that are used.

As described in the previous section, μEDM is a thermal process using spark discharges to pattern microstructures from any conductive material [Mas90, Ho03]. Feature sizes down to 5 μm with a position accuracy of 0.1 μm are possible. Traditional serial mode μEDM has limited throughput. A sharpened wire tip is scanned across the surface of the workpiece while immersed in a dielectric oil medium.

Batch mode μEDM takes the advantages of these serial processes, e.g. material selection and feature size, and blends them with the advantages of a lithographic process, e.g. high throughput. Batch mode (die sinker) μEDM uses lithographically patterned, e.g. LIGA electroplated copper, as cookie-cutter type tools to machine many features in parallel. By utilizing multiple discharge circuits connected to segmented electrode arrays, batch mode can increase throughput by up to 100x over serial mode [Tak02] as shown in the upper left of Fig. 1-6.

Another dimension of comparison between these processes is the material suite available for machining. The y-axis of Fig. 1-7 encapsulates the machining performance information from Fig. 1-6. An ideal process would have a high material removal rate with a small minimum feature size. The x-axis is a subjective assessment of the materials available for machining. The MARIO process is to the far left because it only etches titanium. Micro-milling is susceptible to rapid tool wear when machining hard materials and the overall performance is tied to the mechanical properties of the workpiece and tool.

Photochemical etching (PCE) is masked isotropic wet etching of a metal sheet. It can be used to machine most metals but is still limited by etching chemistry and has large minimum features (0.7x sample thickness).

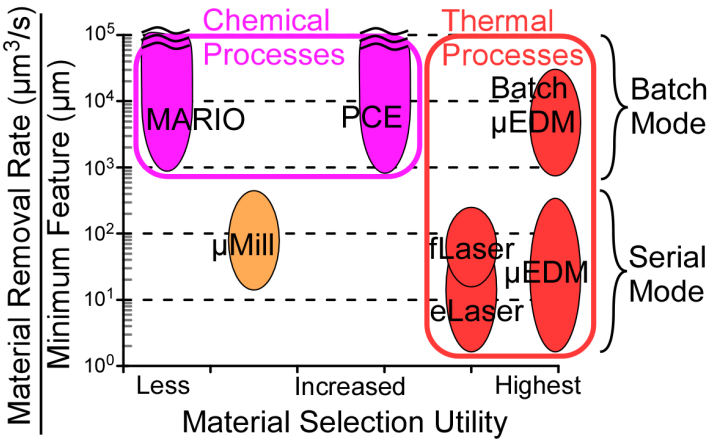

eLaser	Chap02, El-Ho05, Tak05
fLaser	El-Ho05, San07, Tak05
μEDM	Bro98, Chap02, El-Ho05, Kur08, Tak05
Batch μEDM	Tak02, Tak05
μMill	Chap02, Fri96, Tak05
MARIO /TIDE	Aim04, Park05
PCE	Bro98, Chap02, El-Ho05, McGe88, Rao07, Tak05

Fig. 1-7: Comparison of subtractive bulk metal micromachining technologies based on overall performance and breadth of material selection. Processes with the combination of high material removal rates and small minimum feature sizes as well as greater selection of useful materials are desired. Batch mode μEDM greatly increases the throughput compared to serial mode μEDM with the same selection of bulk materials. (AWJ not shown because of large minimum features)

Laser machining and μEDM are both thermal processes but laser machining high thermal coefficient and reflective material like metal becomes more difficult [McGe88]. Highly focused light must superheat the metal to the point of evaporation. As the thermal coefficient increases, the heat travels away from the light spot more quickly and the surface does not reach the same peak temperatures. In μEDM, the heat generation mechanism is a spark discharge, which heats the surface of the metal beyond the melting point and then ejects the molten material as the plasma channel collapses [El-Ho05]. This means that μEDM should be less affected by thermal conduction into the bulk of the metal than laser machining. It also can more easily machine sharp edges and corners.

Both laser and μEDM will machine metals with low melting points faster than those with high melting points.

In terms of resolution and throughput, batch mode μEDM complements other subtractive machining technologies like photochemical etching, and laser machining [Bro98, Chap02, El-Ho05, McGe88, Tak05]. Note that all the batch mode processes have higher cumulative machining performance than the serial mode processes. This is because the pattern size can be easily increased to improve the material removal rate while keeping around the same minimum feature size. The pattern for batch mode μEDM can be increased to several cm and MARIO can be increased to wafer size while PCE can be increased even more.

Table 1.1: Cost comparison of micromachining processes. Highlighted blocks are the most significant costs for the machining process. References in Figs. 1-6, 1-7.

	MARIO	**Laser**	**Serial μEDM**	**Batch μEDM**
Non-Recurring	Cleanroom	Apparatus	Apparatus	Apparatus
	DRIE, Lithography	Controller	Controller	Controller
Recurring	Cleanroom Staff	Operator setup	Operator setup	Operator setup
	Maintenance	Maintenance	Maintenance	Maintenance
	Workpiece Materials	Workpiece Materials	Workpiece Materials	Workpiece Materials
			Tool Materials -Tungsten wire -Brass wire (WEDG)	Tool Fabrication -Sputter deposition -Lithography -Electroplating -Lapping -RIE
			Tool shaping (WEDG)	Tool Mounting

Throughput and resolution are two of the most important factors in choosing a process for a commercial product because they are closely related to cost per part. Table

1.1 outlines a general cost factor comparison for MARIO, laser machining, serial mode μEDM and batch mode μEDM with the most important component highlighted. For example, the MARIO process relies on lithography and deep reactive ion etching for machining. The major cost comes in operating and maintaining several tools in a production cleanroom environment. The DRIE tool in particular can develop problems because of constant cycling of gas mixtures to passivate the sidewalls and etch the bottom surface. Different recipes and gases are needed to etch different materials.

Laser machining is commonly used in biomedical devices at feature sizes that are achievable with serial μEDM but does not have as many recurring costs. For dimensions smaller than 300 μm, serial μEDM uses the WEDG process to reduce the diameter of the tool. The WEDG process uses the μEDM apparatus, significantly increasing the total time to finish a part and requires an operator to monitor progress. For this reason, given a pattern that laser and serial μEDM are equally capable of machining, laser machining is potentially attractive on cost per part. The utility of serial μEDM is in machining geometries that are difficult for laser machining, such as deep high aspect ratio holes for nozzles, sharp edges, and sidewalls.

In contrast, batch μEDM has the potential to compete in other ways. Machining large patterns with small features requires significant machining time for laser, increasing the cost per part. Batch mode μEDM requires significant cost overhead to fabricate the tools, but many tools can be made at the same time by lithography. The process does not use the same apparatus like WEDG in serial mode μEDM. If the tool can be used several times before replacement, the cleanroom costs would be minimized and total cost may be less than using DRIE (MARIO) to machine each workpiece individually.

Batch μEDM may also be able to compete directly with laser machining if the tool fabrication costs are offset by lower machining time, giving lower total cost per part. At high volumes, the difference in cost per part becomes more and more significant. An application that demonstrates this approach would create wider acceptance in industry. In the next section a few applications for bulk metal MEMS fabrication are presented.

1.3 Bulk Metal MEMS Applications

The fabrication of MEMS devices requiring thick patterns of metal is very challenging. For example, the contact resistance of communications devices like RF switches and portable electronics devices like DC-to-DC boost converters is affected by the choice in material used as well as its shape [Ude07]. The ideal material choice would have high mechanical hardness, electrical conductivity, thermal conductivity, and corrosion resistance. Platinum-rhodium is a strong choice but it cannot be deposited in large thicknesses. Commercial RF switches use a structural metal with a thin film contact material deposited on top but are much larger than a microfabricated device. Microfabricated RF switches typically use gold or gold alloys that are co-sputtered with electrostatic actuation. A MEMS thin film device often will have limited power handling, high parasitic capacitance and low standoff voltage. Both approaches require careful process control of the thin film process to get reliable high yield devices. Stress characterization and compensation can be difficult to maintain over long periods of time.

Batch mode μEDM enables the use of Pt-Rh foil or other alloys as a structural MEMS material. Since it is a subtractive process it removes the concern of thin film process control. A bi-stable mechanical structure increases the standoff voltage and lowers

parasitic capacitance but increases the required actuation force and displacement necessary. Electrothermal actuators have both high displacement and high force. A bi-stable electrothermally actuated stainless steel RF switch is presented in the appendix.

Biomedical implant devices such as antenna stents also have limited options for material selection due to biocompatibility requirements. Stents are structures used to scaffold an artery (or other vessel) open after balloon angioplasty, relieving a constriction. They are most often constructed from #316L stainless steel and permanently expanded by a balloon to the proper diameter. Occasionally, the artery will reclose (restenose) over time. While drug-eluting coating technology has reduced the occurrence of restenosis, the long term effects are still being studied. Unfortunately, there currently is no non-invasive way to follow-up and monitor the environment around the stent after it has been implanted. It would be beneficial to have a long term sensor to detect if there is restenosis before an intervention is critical.

A stent is typically patterned by laser machining perforations into a solid tube to form a wire mesh. A planar metal foil can also be patterned to form a stent. The planar approach opens the door to lithography compatible machining and also to mounting sensors. The stent itself can also be used as an inductive antenna, forming a resonant tank with a capacitive sensor. Past work by Takahata and DeHennis et. al. offered hybrid pressure sensor solutions on an antenna stent platform [DeH04, Tak03, Tak05]. Challenges in form factor and wireless link power were encountered along the way. The feasibility of a high-Q antenna stent for pressure monitoring using biocompatible bulk stainless steel is discussed in Appendix A. The fabrication of a bi-stable stainless steel RF switch is presented in Appendix B.

1.4 High Density Batch Mode µEDM Challenges

While batch mode µEDM has a lot of promise, this thesis largely focuses on identifying and addressing the fundamental scaling limits associated with machining patterns with high feature densities at high precision. As feature size is decreased, feature spacing reduced, and pattern size increased, machining debris begins to affect overall machining performance. When debris accumulates, it causes unwanted secondary discharges that can diminish both the workpiece and tool. The impact on scaling resolution and uniformity is investigated in chapter 2.

Two solutions for handling debris accumulation effects are in chapter 3. First, a sidewall passivation coating prevents spurious discharges in undesirable locations. Next, a hydraulic through-workpiece flushing method uses the bubbles naturally formed during the discharge cycle to pull debris away from the discharge gap, significantly improving throughput.

The next chapter presents a wireless method for monitoring not only debris accumulation, but the depth location of an interface between two metals. The current method of monitoring the discharge quality is to use voltage or current probes on the terminals of the discharge circuit. Probes at these locations can both be affected by electrical parasitics and cause parasitic loading at low discharge energies. An alternative method of monitoring the discharge is to use the wireless signal inherently generated by the spark discharges.

Another issue encountered in large scale EDM is the residual stress in the recast on the machined surface. The residual stress study in chapter 5 is important because it is the first to study the low energy discharge recast of µEDM. This study will help improve the

microfabrication of precision metal parts because residual stress is often relieved by bending that can cause damage during machining. For example, in high density patterns debris related spurious discharges could cause machining on the top surface of the workpiece, creating a stress gradient that is relieved through vertical bending and potentially contacting the tool.

The main thesis work finishes with conclusions and future work in chapter 6. Appendices A and B then present two applications for batch mode μEDM: a high-Q antenna stent with integrated pressure sensors and a stainless steel bi-stable RF switch.

CHAPTER 2

HIGH DENSITY BATCH MODE μEDM

2.0 Introduction

Micro-electro-discharge machining is a thermal process similar to laser machining in that it leaves a recast layer on the surface after machining. The basic setup is to apply a voltage across a tool cathode and workpiece anode in a dielectric fluid. A spark discharge occurs at constant distance (discharge gap) and thermally erodes the anode side more than the cathode.

Proper spark discharging is a complex sequence of events which is still being debated after more than 60 years [Alb96, Desc06, Kan97, Lew03, Mur70, Pom92, Schul01, Schum04] of use. The stages after a sufficient voltage is applied between the tool and workpiece are electron migration, ionization and electron avalanching (Fig. 2-1). Eventually a streamer (plasma channel) is formed between the electrodes allowing extremely high currents to pass, which primarily heat the anode (workpiece) side well above the melting point. When the current through the channel can no longer be sustained due to the RC timing circuit, the channel collapses. The violent implosion of the channel forces the molten spot in the workpiece into a crater formation, ejecting debris.

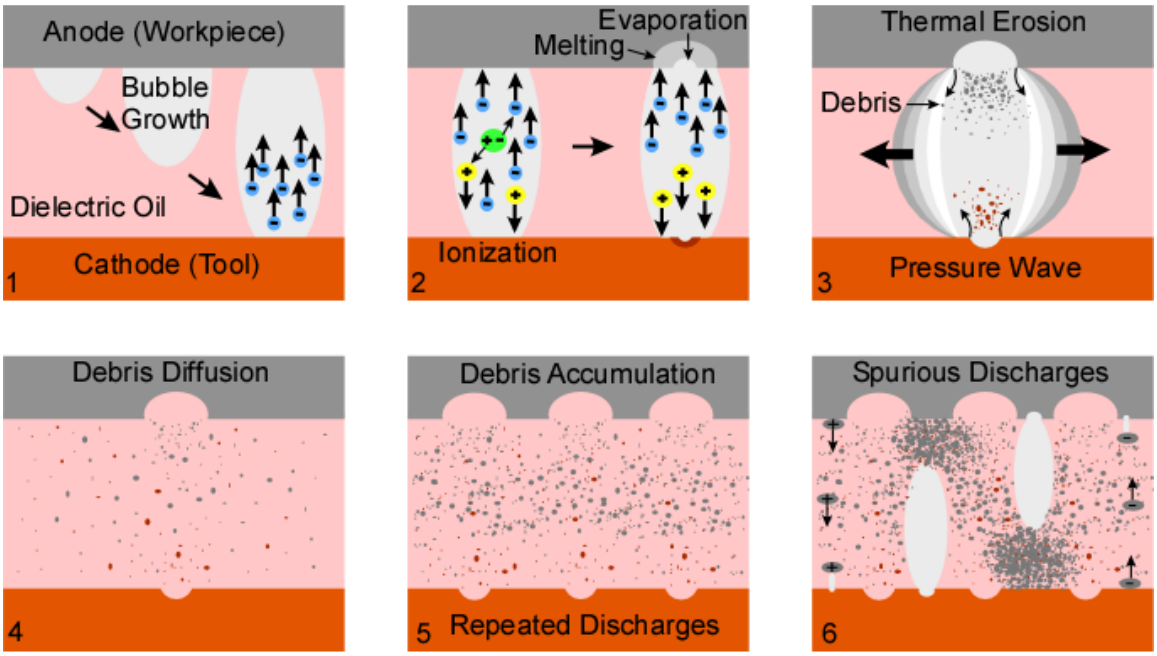

Fig. 2-1: Machining mechanism of µEDM. Steps 1-4 describe normal discharges. In step 5, repeated discharges lead to debris accumulation. Finally, excess debris causes spurious discharges through clusters of debris (middle) as well as by individual debris particles (edges).

Understanding and exploiting these events has led to many improvements in machining performance. The pertinent steps for this work are the plasma channel initiation, plasma temperature, and gas evolution. A point of contention among several studies is the precise mechanism for the plasma channel initiation. In water, one study points to the primary initiator as hydrogen bubbles from hydrolysis [Desc06]. In oil, bubbles from hydrolysis do not occur as readily but debris particles seem to contribute. Regardless if this is the true mechanism, several studies have noted that a higher concentration of debris particles increases the likelihood of a discharge [Desc06, Schum04, Tak02].

In [Alb96, Desc06, Ho03], optical spectroscopy of the plasma shows the electron temperature is on the order of 10,000 K. With metal contaminants the temperature decreases to around 2,700 K [Desc06]. Residual debris particles from the tool and

workpiece cause variation in discharge characteristics not only in location, but also in energy.

One point that may affect batch mode µEDM much more than serial mode is gas evolution. For each spark discharge, a small amount of hydrogen gas in the plasma channel is left behind. In serial mode this gas naturally coalesces into larger bubbles that eventually rise out of the discharge gap, entraining debris as they go [Kan97, Mur70]. In batch mode, the tool areas are very large with only small separation from the workpiece. The bubbles tend to become trapped within the tool features. As noted before, gas bubbles could initiate discharges in water but if they are trapped in the discharge gap this may also be true in oil [Desc06, Pom92]. They can also have the effect of more densely concentrating debris in the discharge gap.

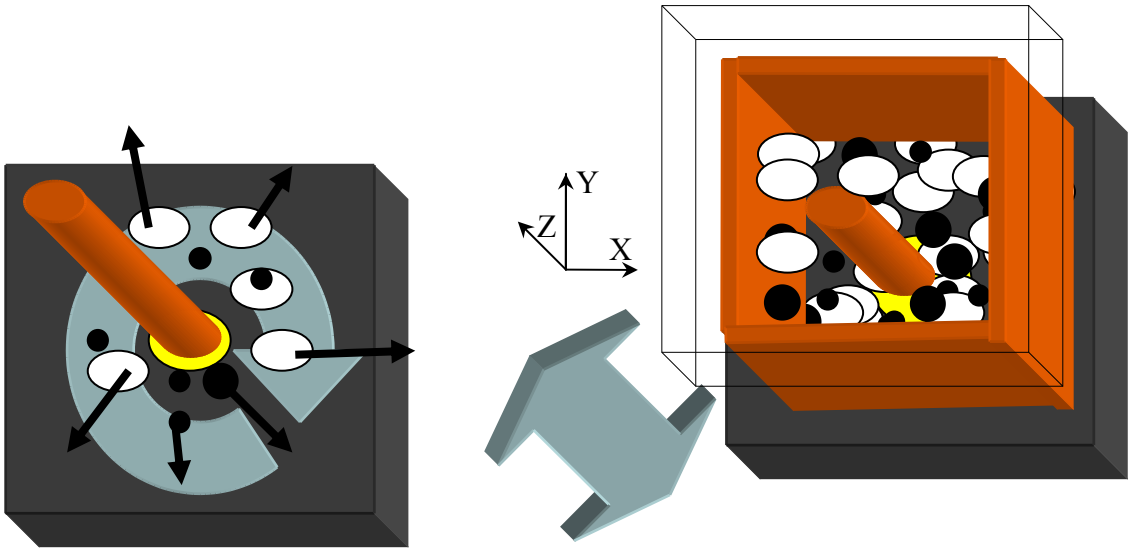

Fig. 2-2: Serial mode µEDM uses rotation to eject debris and gas bubbles away from the discharge gap. Batch mode µEDM can only use a vertical dither that is not as effective. Gas and debris are trapped in large patterns and can deteriorate machining quality.

Self-created machining debris are critical in determining tolerances for both serial mode and batch mode µEDM [Tak05]. In serial mode, the machining tool can be both

rotated and vertically dithered to flush out debris (Fig. 2-2). However, in batch mode, the tool movement is limited to a vertical dither motion. The large planar extent of the tool and its high-aspect ratio features limit traditional options for flushing.

When the density of features increases in batch mode, debris accumulation leads to spurious discharges that damage the workpiece surface and cause excessive tool wear [Tak05]. Eventually, debris accumulation between the tool and the workpiece causes uncontrolled arcing, and stalls machining indefinitely. While the dielectric oil that separates workpiece from tool during machining does help dissipate heat, fluid flow is severely restricted in batch μEDM. As machining progresses, local temperatures may increase.

For batch mode μEDM, copper electroplated into a photolithographically defined mold is a convenient material choice for the tool. The benefits of copper are its high electrical and thermal conductivity as well as its process compatibility. While the melting point of copper is >1000° C, it softens at much lower temperatures (~280° C) [Kao04]. The high local temperatures soften and recast the tool into a mushroom shape, which is then transferred to the workpiece. As feature density increases, the problem limits both vertical cutting depth and lateral resolution.

Various methods for handling the debris buildup have been attempted. The main alternatives are adding vibration to the stage or tool [Gao03, Kan97, Kan00, Lim03, Yeo99A, Yeo99B, Yu02, Zha04, Zhan04], integrating dielectric flushing to the stage or tool [Kum03], and/or tool coatings [Aoy99, Kum03]. Stage vibration cyclically forces the tool toward the workpiece so that the dielectric oil and debris are pushed out of the discharge gap. The return stroke then pulls fresh oil into the gap. Increasing dither

amplitude can increase flushing, but also increases the pressure applied on the tool features. Lateral movement error may also increase. Applying a planetary motion to the tool improves the maximum aspect ratio but increases the minimum feature size [Kan97, Yu02, Zha04]. Integrated dielectric flushing involves a nozzle shaped tool/workpiece that forces fresh dielectric oil into the discharge by positive or negative fluidic pressure [McGe88]. However, the flow region of debris tends to increase the discharge gap in those areas. Tool coating/encasing allows for a hybrid of material properties such as wear resistance and high cutting precision on a single tool [Kum03]. While these methods have been applied to both macro and micro scale serial mode EDM, only a ~10 μm vertical or planetary stage vibration with frequencies in the 10s of hertz has been reported for batch mode.

This chapter examines scaling trends associated with debris generation in batch mode μEDM on a Panasonic ED-72 μEDM using a parametric study which is described in section 2.1. By varying tool width and tool spacing, trends are found that point to improved designs. Machining trends associated with cross patterns are investigated in section 2.2. In section 2.3, parallel lines are used. Finally in section 2.4, arrays of squares are presented. Two solutions for handling debris buildup are then presented in the following chapter. A passivation tool sidewall coating reduces spurious discharges and a two-step machining approach allows gas bubbles generated during machining to hydraulically flush debris away from the discharge gap.

2.1 Batch Mode µEDM Machining Resolution Study Definition

Three different classes of features are presented in this study: isolated crosses, parallel lines, and square arrays. All three are commonly used lithography patterns. Each feature adds different complexity to the microfluidic path for debris to exit from the discharge gap.

2.1.1 Tool Fabrication

Copper tools ranging from 175-200 µm tall were fabricated at Sandia National Laboratories, CA using polymethylmethacrylate (PMMA) LIGA on a low-Z titanium oxide seed layer (Fig. 2-3). The process begins with depositing the electroplating seed layer on a thick (1-2 mm) silicon wafer substrate and solvent bonding PMMA on top. X-ray exposure was done at the Advanced Light Source at Lawrence Berkeley National Laboratory. After developing the PMMA into a mold, copper was electroplated into it and lapped back to the finished thickness. After dicing, the PMMA mold was released in acetone, leaving the electroplated copper.

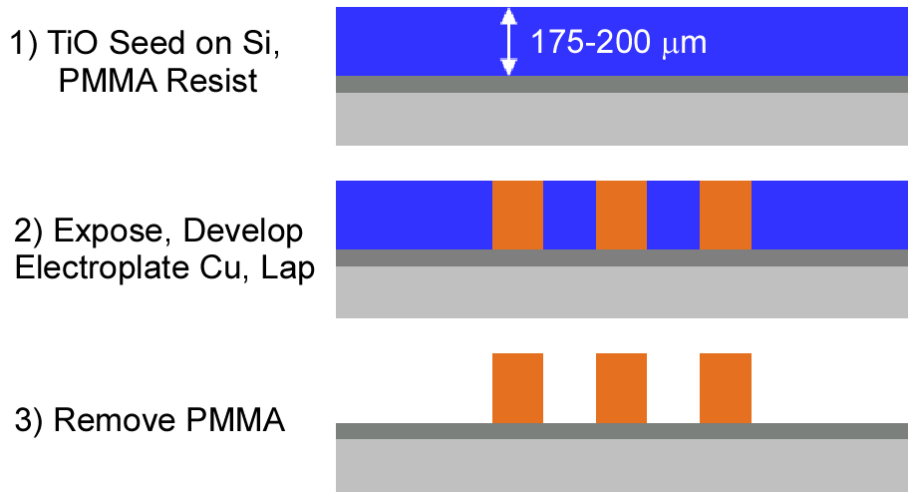

Fig. 2-3: LIGA process for batch mode µEDM tool fabrication.

These tools were used to machine patterns 30 μm deep into 100 μm-thick, #316L stainless steel foil workpieces with a Panasonic MG-ED72 μEDM. The height of the tool did not influence the machining. The end of a 5 mm diameter aluminum mandrel was planarized using the WEDG process [Masu85] and the workpiece was mounted to the mandrel using silver epoxy. The sample had a flatness of approximately 2 μm after mounting.

2.1.2 Experiments

The isolated cross, parallel line, and square array patterns used in this study each investigate different effects of debris on machining. Varying the size of a single cross shows the debris effects when the ratio of machined surface area (debris volume) and feature edge length (microfluidic resistance of escape path) is changed. Parallel lines of varying width and spacing add the interaction of adjacent features to the escape path of the debris. Finally, a 2D array pattern of varying width and spacing adds another axis of interaction to the escape path.

Table 2.1: Machining conditions for parametric study.

Voltage	70V
Capacitor	10pF
Resistor	5kΩ
Z-Feed	0.2μm/s
Stage Dither	~10 μm

Machining parameters for these experiments are given in Table 2.1 and were chosen for surface smoothness and edge finish at the expense of machining time. Kerosene-

based μEDM dielectric oil separated the tool from the workpiece during machining for heat dissipation, debris removal and discharge energy regulation. Electrical contact was made to the tool through the seed layer. Since the tool could not rotate as in serial EDM, the stage was dithered vertically to improve debris removal.

Lateral dimensions at the top of tool and workpiece features were measured under high magnification on an optical microscope. SEM images showed that sidewalls were vertical with around 2-5 μm of rounding at the bottom of the workpiece features that corresponded to tool wear rounding. Measurements of tool height and workpiece depth were taken using the glass slide scale on an optical microscope by focusing on the top then bottom surfaces. Tool plunge depth measurements during machining were recorded from the μEDM controller. It is important to note that this is simply the distance traveled from the first discharge and does not account for losses due to tool wear. Depth measurements were recorded at timed intervals but the timing of erratic events was also recorded.

2.2 Crosses

The isolated feature study used 600 x 600 μm long cross patterns to investigate the impact of varying tool widths, from 10-100 μm, on discharge gap due to self generated debris. It also shows how machined feature edges vary in the middle of a cross arm compared to the end. All features were machined at once, ensuring the same conditions for comparison. Cross pattern tools were used because they are more mechanically robust during mold stripping compared to free standing line patterns in the LIGA process. Prior to machining, the top surfaces were planar from lapping.

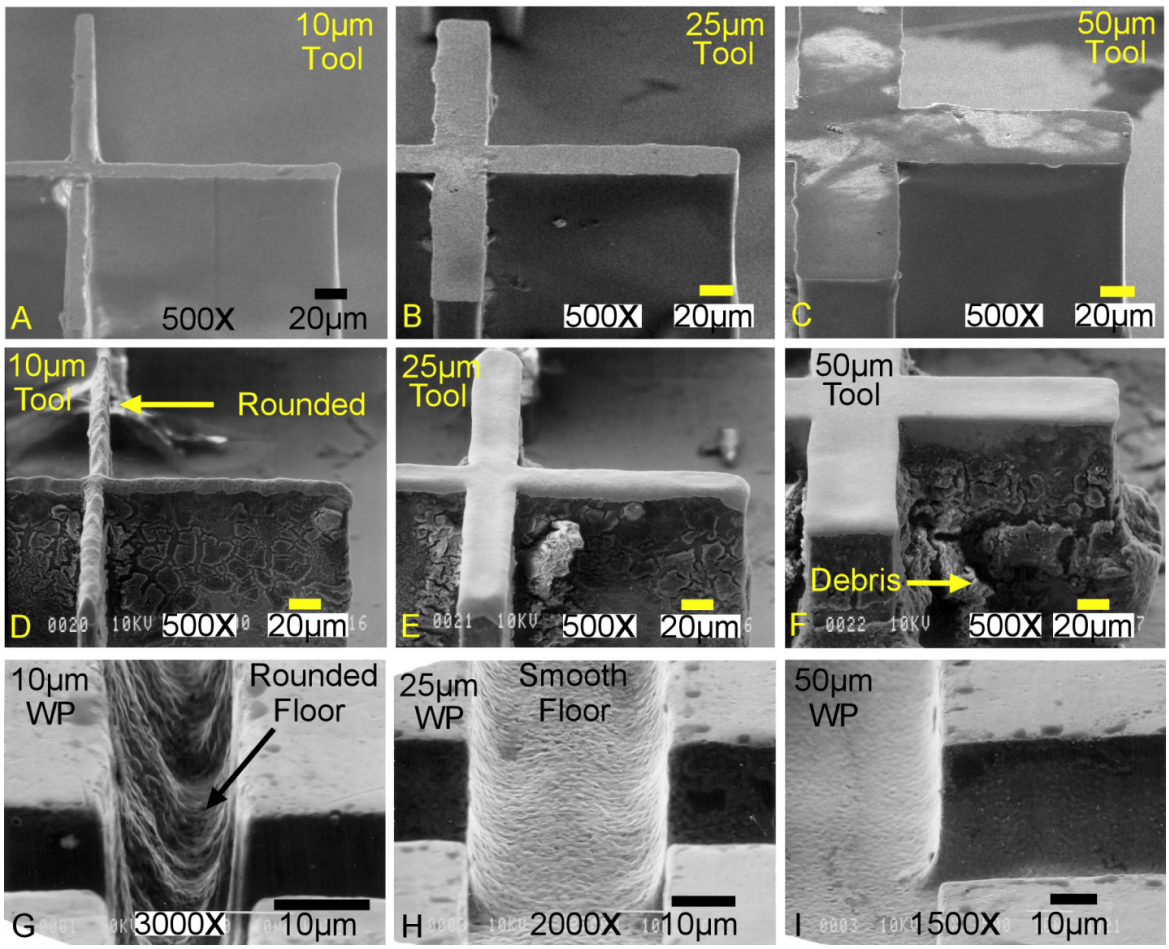

Fig. 2-4: SEM image survey of 600x600 µm cross features with varying widths of 10, 25, and 50 µm. The top row (A-C) shows freshly fabricated (unused) tools, the middle row shows tools that have been worn by the machining process, and bottom row are machined workpiece features. Note the rounding of the tools after they have been used. Note the amount of debris along the sidewalls in F compared to D and E. G shows effects of tool wear at bottom of workpiece. A-F are at 500x magnification, while the remaining images at higher magnification.

2.2.1 Results

The SEMs of the tools and corresponding workpieces in Fig. 2-4 show that the 25 µm width tool provides a good compromise between good finish and low debris buildup. (The tool was not cleaned after machining but the workpiece was cleaned in an ultrasonic bath.) In comparison, the 10 µm tool had considerably more wear and rounding as a fraction of the total width, which transferred to the workpiece. However, it also had very

little residual debris. If the intent were to machine through the entire workpiece and the tool were much taller than workpiece, this tool width could still be acceptable. The wider tools all show progressively better edge and surface finish albeit with some minor footing at the bottom of the workpiece and increasing residual debris. The images of the 75 and 100 µm wide tools (not shown) were similar to the 50 µm tool.

The discharge gap vs. tool width data for isolated crosses in Fig. 2-5 was taken using a filar eyepiece at 500x magnification. Each data point represents the subtraction of the mean initial tool dimension from the mean finished workpiece dimension, divided by two (n=20) and the error bars are at +/- one standard deviation.

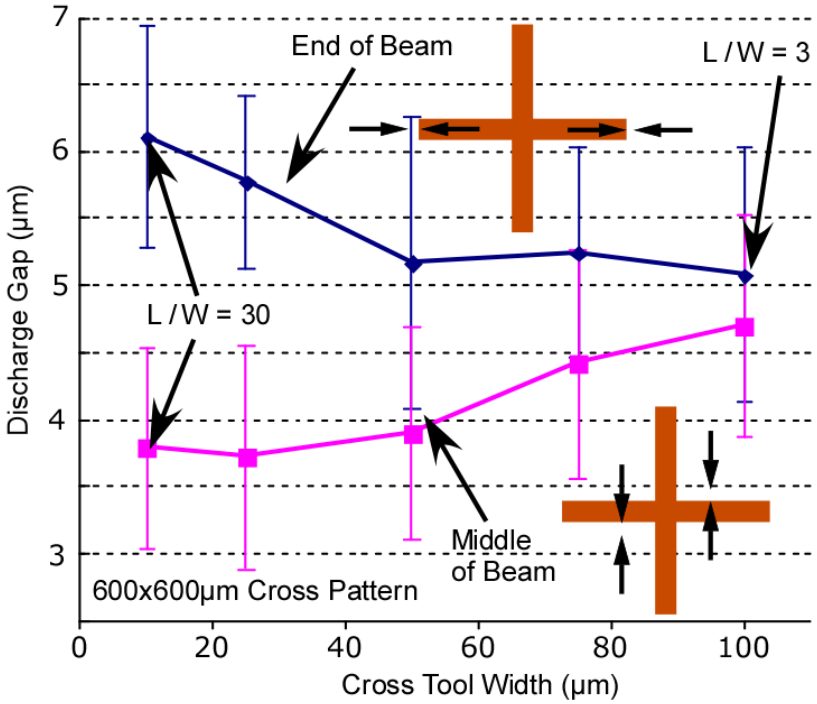

Fig. 2-5: The discharge gap at the ends of the machined features (upper lines) were larger than at the center (lower line). However, for 600x600 µm long features, as the feature widths change from 10 µm to 100 µm, the discharge gaps at these two locations become comparable. Discharge gap were determined by subtracting the tool width from the machined workpiece width and dividing by 2. Error bars are one standard deviation from the mean (n=20 for each data point).

There are two distinct trends which depend on the region of the tool. In the array of patterns that was tested, the tool feature width was increased, while the length of the features remained fixed. The ratio of feature width to feature length (L/W) varied from 3 to 30. The discharge gaps at the ends of the tools were generally larger than at the center. It was noted that when the ratio was small, the discharge gaps at the two locations became more similar (Fig. 2-5). Figure 2-5 shows that the discharge gap measurements are repeatable with less than 1 µm variation for the 3 different 100 µm crosses.

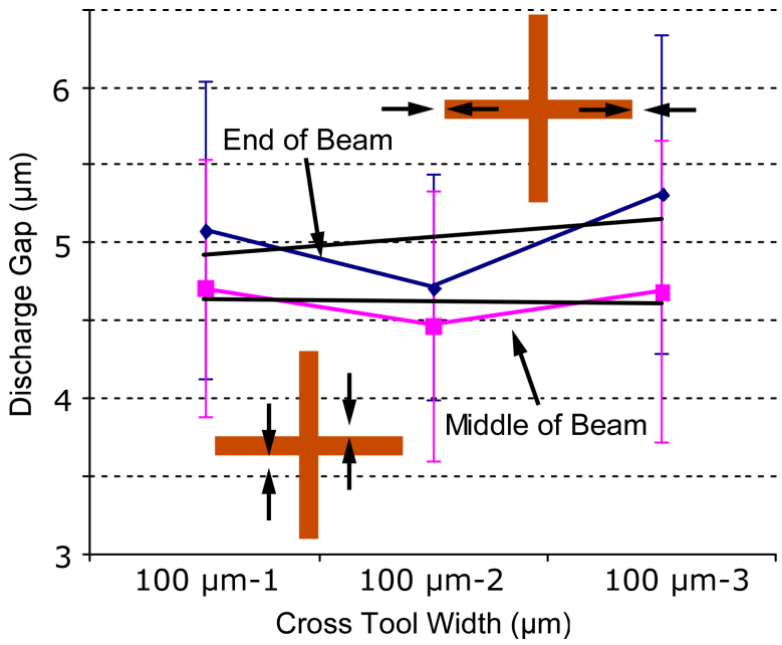

Fig. 2-6: Discharge gap is repeatable for 3, 100 µm feature width tools with less than 1 µm variation between them.

Lateral (edge) tool wear at the same locations was investigated to determine if the discharge gap trends were related. In Fig. 2-7 it can be seen that the tool wear was

consistent for all tool widths. There was more average tool wear in the middle of the beam than the end, which is the opposite of the discharge gap data in Fig. 2-5. Note the large error bars from the rounded edges of the tool after machining. However, the 3 100 µm beams gave consistent results in Fig. 2-8. These figures indicate that the opposing discharge gap trends were not due to variations in tool wear when tool width increased, but were due to an unexpected variation in the resulting pattern machined into the workpiece. In addition, it can be seen from the SEM images in Fig. 2-4 that the tool wear was less than the 30 µm machined depth. This means the top surface of the workpiece would have been exposed to the full width of the tool.

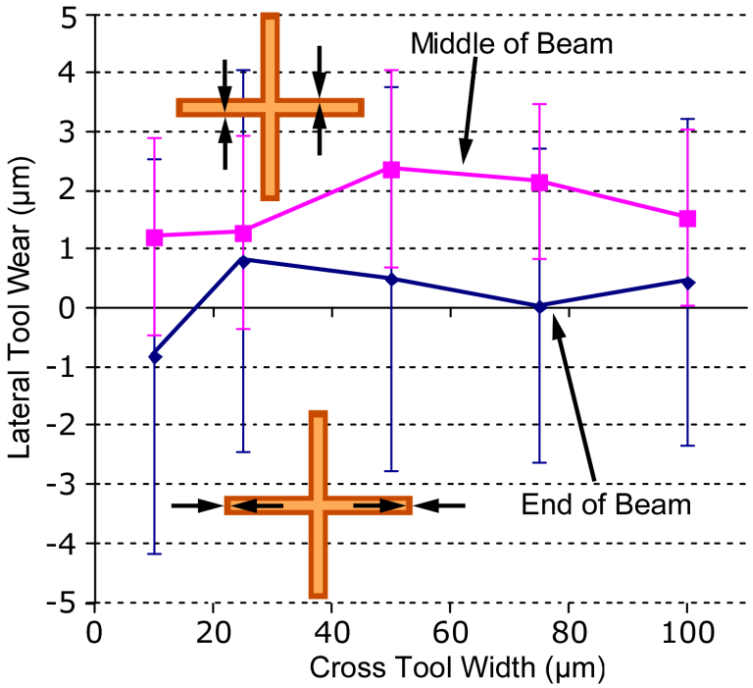

Fig. 2-7: Lateral tool wear was fairly consistent for different tool feature widths. Large error bars are due to the rounded tool edges.

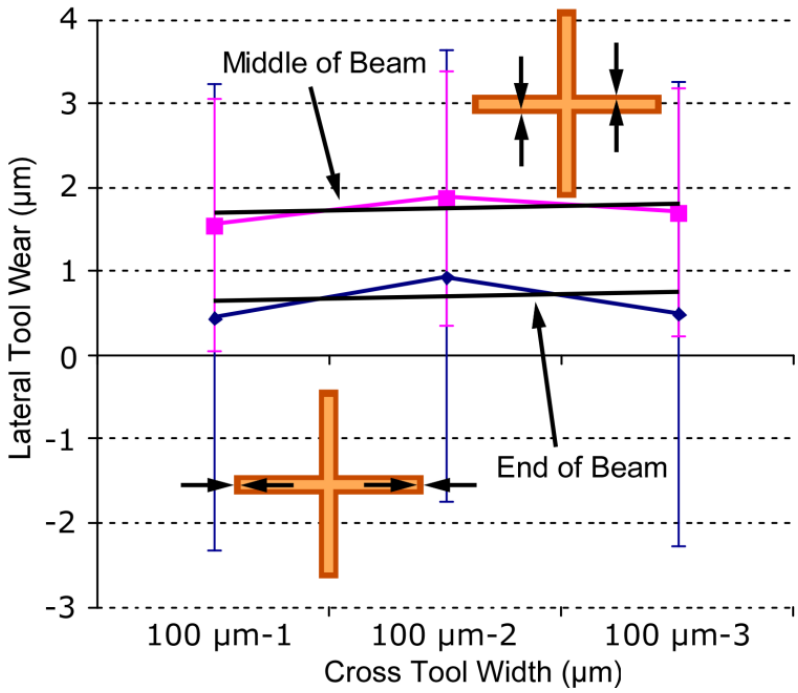

Fig. 2-8: Lateral tool wear was fairly uniform for 3 100 µm wide tools. The large error bars are due to the rounding of the tool edges.

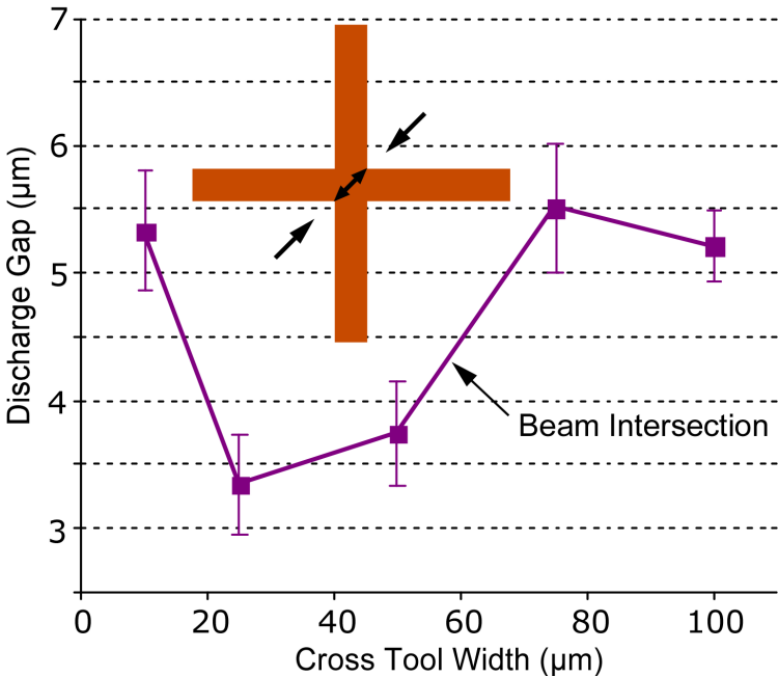

Fig. 2-9: Discharge gap vs tool feature width at the intersection of the cross beams is non-linear.

Finally, the diagonal discharge gap and tool wear at the intersection of the beams were investigated. Figure 2-9 shows that, unlike the middle and end beam measurements, the intersection discharge gap did not follow a linear trend with increasing tool width. When the lateral tool wear is plotted though, the inverse pattern in Fig. 2-10 indicates that tool wear tracked the variations in discharge gap. In this case, the sum of the discharge gap and the lateral tool width is nearly constant (~1 µm), unlike the middle and end of the beams.

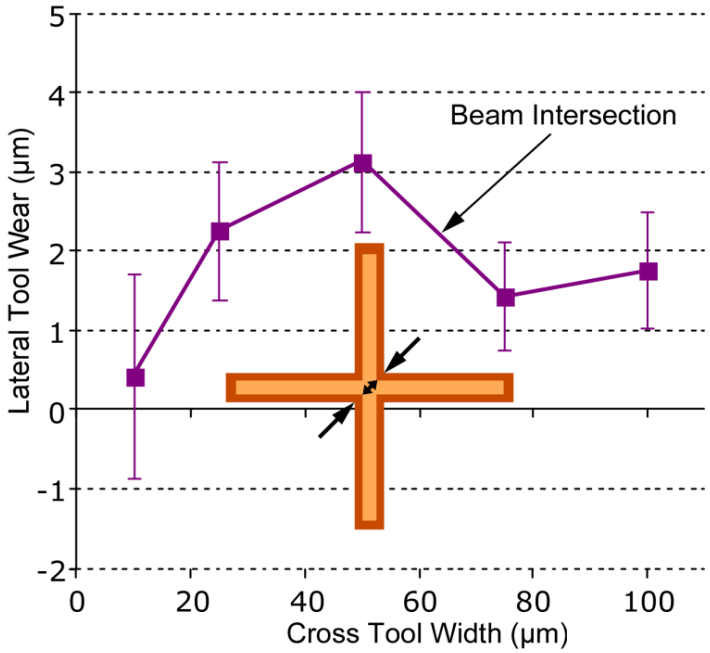

Fig. 2-10: Tool wear at the intersection of the cross beams is also non-linear, agreeing with the discharge gap plot.

2.2.2 Hydraulic Resistance Modeling

Fluent™ simulations were performed to determine if the hydraulic resistance for debris to escape could be related to the different discharge gap trends in Fig. 2-5. Single, 300 µm long lines (one cross beam) with variable widths were simulated. Eight fluidic pressures were applied at the inlet of a 30 µm tall (channel length) annular rectangular

channel and the integration of the flow at the outlet gave the total flow. The discharge gap (channel height) was 6 µm, viscosity 1.4 cP and specific gravity of 0.798. The Fluent™ simulation uses the Navier Stokes equation and the continuity equation to solve the flow. Laminar flow with a no-slip boundary condition at the walls was assumed.

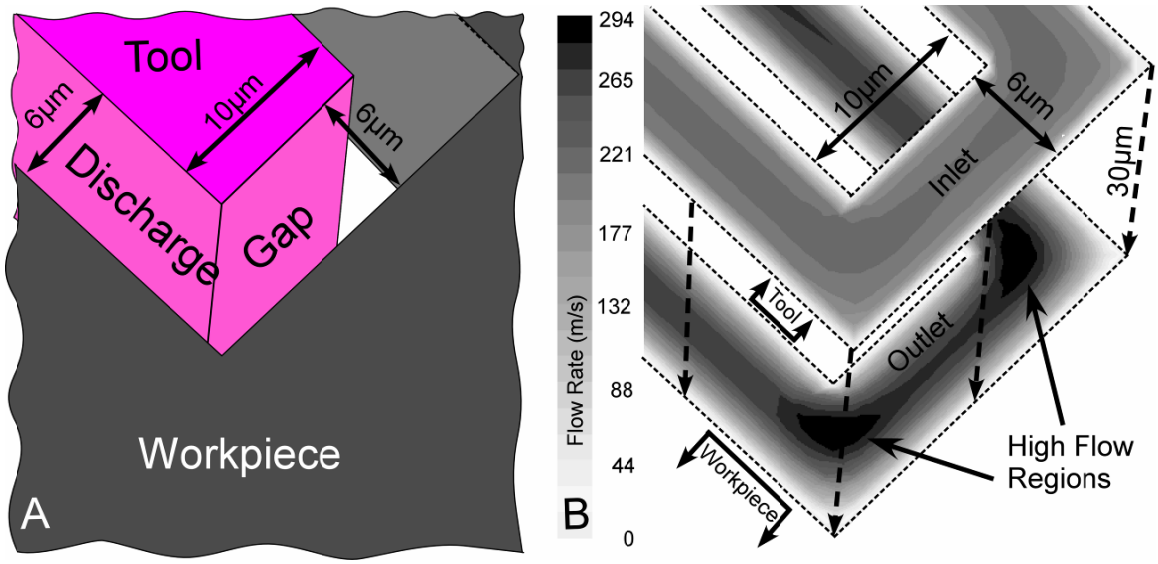

Fig. 2-11: Fluent™ simulation of dielectric oil flow profile for discharge gap surrounding a 10x300 µm tool. A) Simulation dimension definition. B) High flow region occurs at the sharp corners and on the edge connecting the corners. Increased debris flow in this region may lead to more spurious discharges that cause an increase in discharge gap.

Figure 2-11A shows the simulation dimensions for a 10 µm wide line tool feature. Figure 2-10B shows the flow profile at the inlet and outlet at 70 kPa. The corners form higher flow regions than the rest of the structure. The linear flow (Q) vs pressure (P) slope corresponds to the hydraulic resistance (R) of the structure since P=QR. As shown in the flow profile, the resistance is lower at the end of the line and more debris will likely tend to pass through that area. Since electrical discharges also tend to occur more frequently at edges and corners, this could lead to a local increase in spurious discharges and tool wear, which would account for the increase in discharge gap. For wider tools,

the flow profile is more evenly distributed and tool wear decreases. In the mid-point of the line, the discharge gap likely increases with tool width because the amount of debris generated (tool surface area) has increased while the local hydraulic resistance has remained nearly the same.

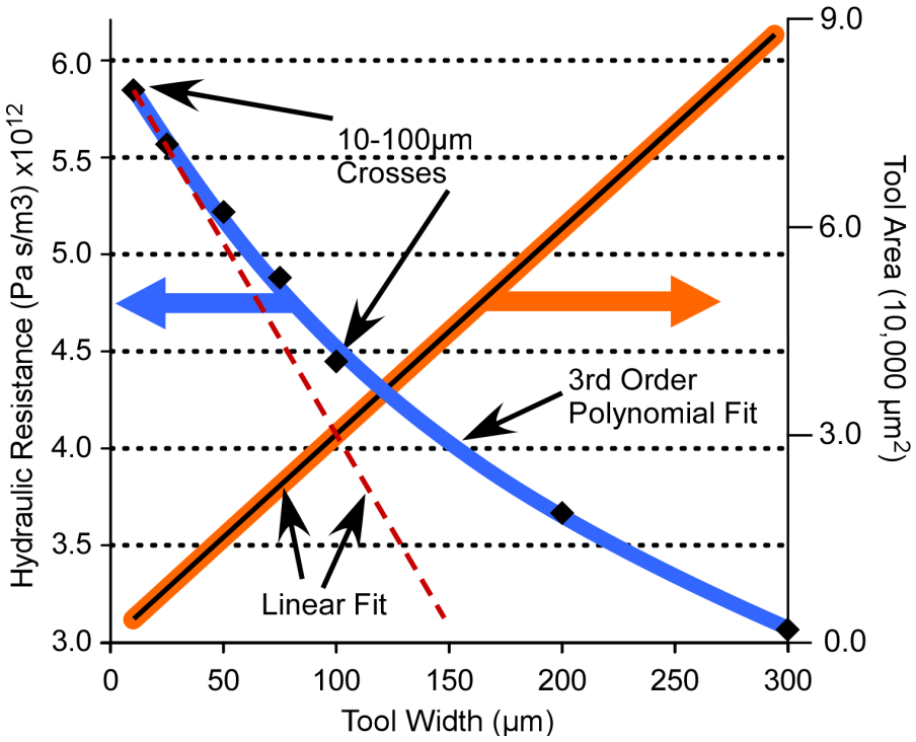

Fig. 2-12: Discharge gap hydraulic resistance of single line tool with a fixed length but variable width calculated with Fluent™ simulations. The area of the tool increases linearly with tool width but the hydraulic resistance does not decrease linearly.

Figure 2-12 shows that as tool width increases, the area for machining increases linearly while the hydraulic resistance of the channel surrounding the tool does not decrease linearly. This suggests the path for the debris to escape may not be widening as fast as the amount of debris generated is increasing. As more debris accumulates in the discharge gap it will likely widen to accommodate. Note that only the resistance on the side of the tool is accounted for in this model. As the width of the tool increases, the average distance from the actual discharge site to the side of the tool also increases.

Even though there were variations in discharge gap, tool wear was nearly constant in the middle and end of the beam. In these areas, differences in debris accumulation increased the intended workpiece feature size. As tool width decreases, the difference between the feature machined in middle and at the end of the beam increases. However, at the intersection, variations in tool wear caused the changing discharge gap for tool widths less than 75 µm.

2.3 Parallel Lines

The dimensional tolerance of grouped batch µEDM features was evaluated using 600 µm long parallel trenches machined by four parallel lines of 10,15,25, and 50 µm width and 5,10,15,18,20,25, and 50 µm spacing. The layout allowed for machining of 16 different sets of features at once while minimizing debris movement among different size features.

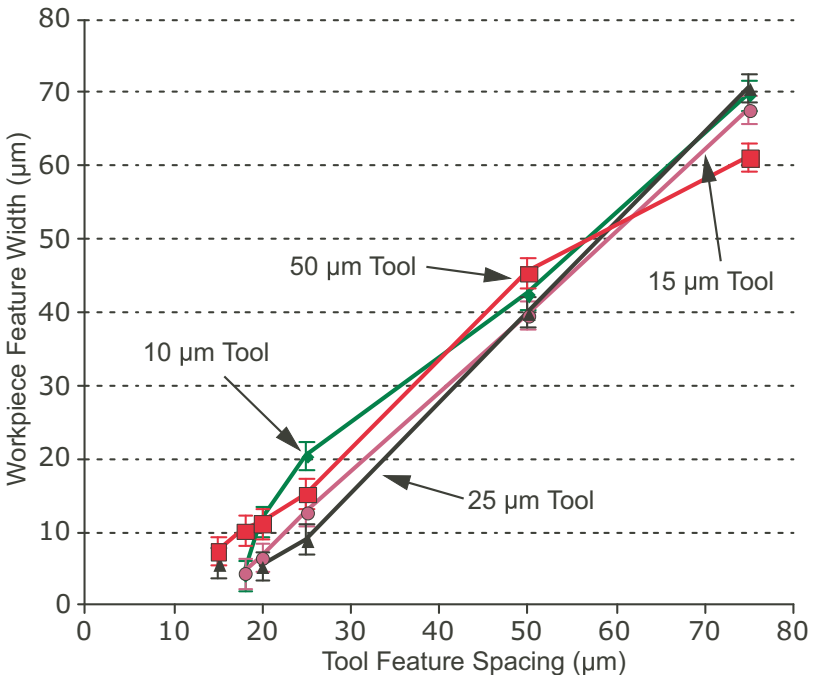

Fig. 2-13: Linear relationship between tool feature spacing and finished workpiece feature for various tool feature widths.

Parallel lines, 600 μm long, with varying widths and spacing were machined with the same conditions as the crosses. Digital imaging was used to measure the width of the tool and workpiece features and compared with a known reference before and after machining. By increasing the spacing between tool features (while keeping tool width constant), the resulting workpiece feature width linearly increases as expected (Fig. 2-13). Examples of tools and workpieces after machining are shown in Fig. 2-14 and Fig. 2-15. Note how differences in tool width can have an effect on debris accumulation between features, even when tool spacing remains the same. For the 10 μm spacing, the combined discharge gap of the lines was too large and there was nothing left at that location on the workpiece.

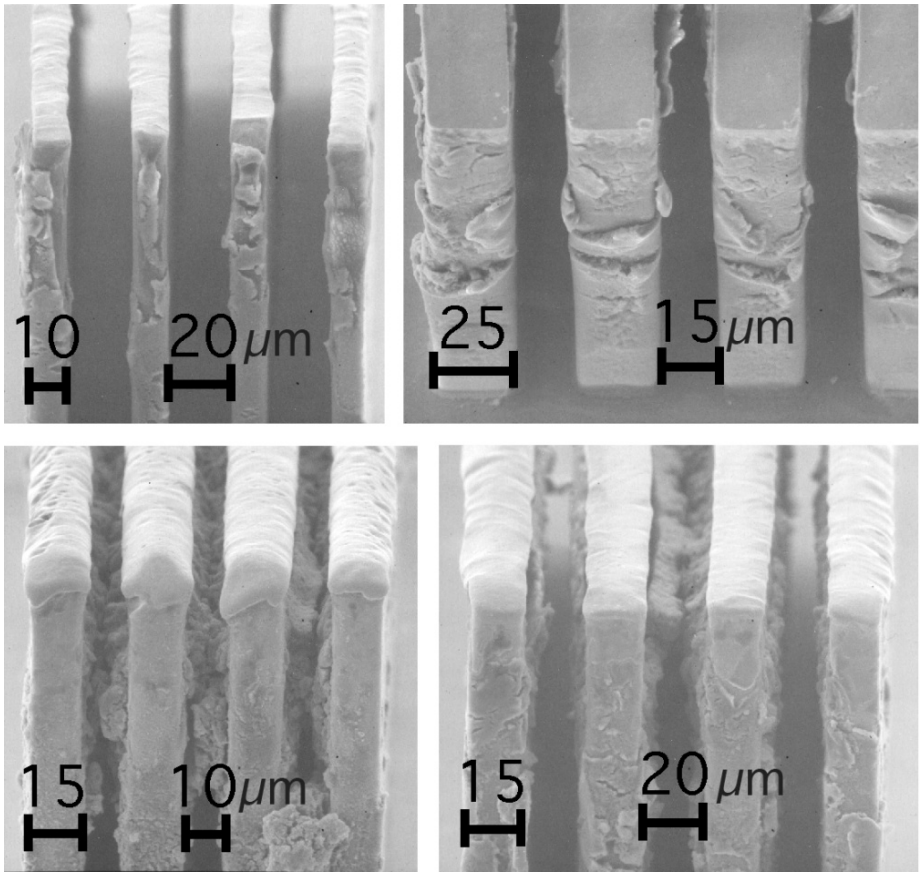

Fig. 2-14: Copper tool features of various widths and spacing after machining. A and B have little debris and wear. C and D have significant debris and some tool feature recasting.

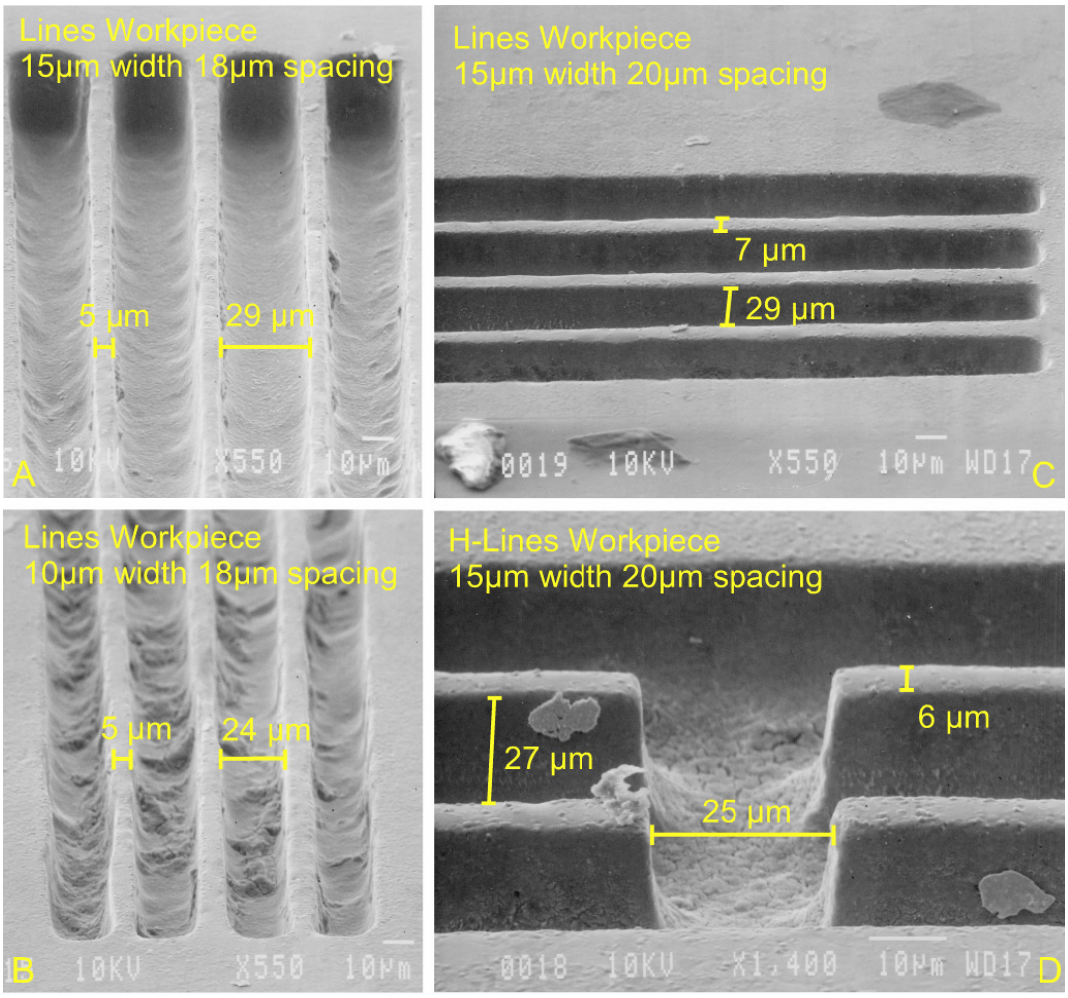

Fig. 2-15: SEM images of workpiece features machined in the resolution study. While debris accumulation may cause larger features, the periodicity of beams and spaces remains constant. The H-line pattern in D added a cross beam to the parallel lines. This additional beam causes a width variation at the intersection.

Figure 2-16 shows the machining tolerance for this test pattern. Machining tolerance is defined as the original tool feature spacing minus the actual machined width. This value is the addition of one discharge gap each from two adjacent line features. Three tool feature spacings are shown for clarity in Fig. 2-16. While 5 µm wide features can be machined, it is notable that the tolerances range from 5 to 17 µm, and have several trends.

Similar to cross features, the debris generation rate of a particular tool feature width does not scale at the same rate as the hydraulic resistance for the path to remove the

debris. For these parallel lines, the small spacing between features forms an additional rectangular channel hydraulic resistance in series with the discharge gap resistance and defined by [Mor01]:

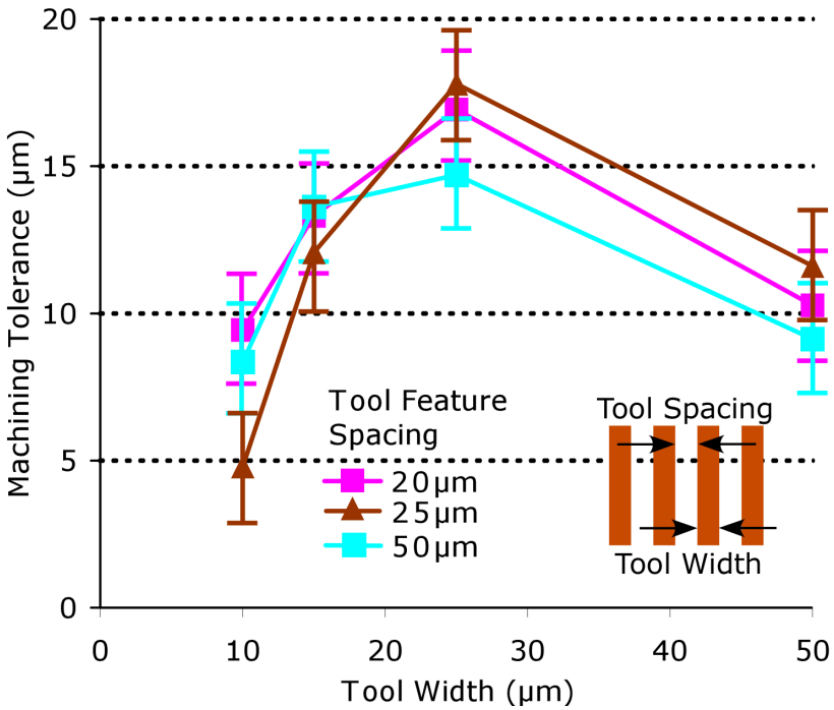

Fig. 2-16: Machining tolerance, (i.e. original tool feature spacing minus machined width), shows a non-linear dependence on tool feature width and ranges from 5-17 µm. It indicates the necessary tool spacing to achieve a desired workpiece feature. Machining tolerance is the sum of two discharge gaps from adjacent features where as discharge gap measurements are taken from the same feature. Error bars are an estimate of the error in the measurement technique (n=3).

$$R = \frac{12\eta L}{H^3 W - \frac{192}{\pi^5} H^4 \sum_{m=0}^{\infty} (2m+1)^{-5} \tanh[\frac{(2m+1)\pi W}{2H}]} \qquad (2.1)$$

where η, L, H, W are viscosity, length, height, and width respectively. At the mid-point of the tool, for 20 µm spacing, 175 µm tall tool and m=500, this resistance is 2.24×10^{12}

Pa-s/m^3 (43% of the discharge gap resistance for a 50 μm tool width). The discharge gap separating the sidewall of the tool and the workpiece is strongly influenced by the width of the tool but is different from the single cross feature in the previous section. The 20, 25, and 50 μm feature spacing data follow the same trend, but there may be further trends. At a constant tool width of 25 μm, as the tool spacing increased, the machining tolerance improved.

For narrow tool features, the debris generation rate is low, the features are easily flushed when reasonably spaced, but tool wear is high as a percentage of total width. As the tool feature widens, more debris is generated and the machined width increases more. Since the debris removal rate may not scale at the same pace, the debris cannot exit the discharge gap fast enough. Debris from adjacent features makes the problem even worse, leading to excessive tool wear.

2.4 Arrays

Arrays of features add another dimension of influence to the analysis. Squares were fabricated in 8x8 arrays with diameters ranging from 20 to 100 μm. In past work, it was found that the discharge gap was larger and tool wear was greater at the center of an array (Fig. 1-2) [Koch00, Tak05]. In this study, the impact of tool diameter was concomitantly investigated. Inter-feature spacing was kept equal to the diameter because the impact of feature proximity was already investigated in the parallel trench study and may have confounded the results. For square arrays this means a 25% feature fill. The arrays were machined 35 μm deep. Examples of tools and workpieces after machining are shown in Figs. 2-17 and 2-18.

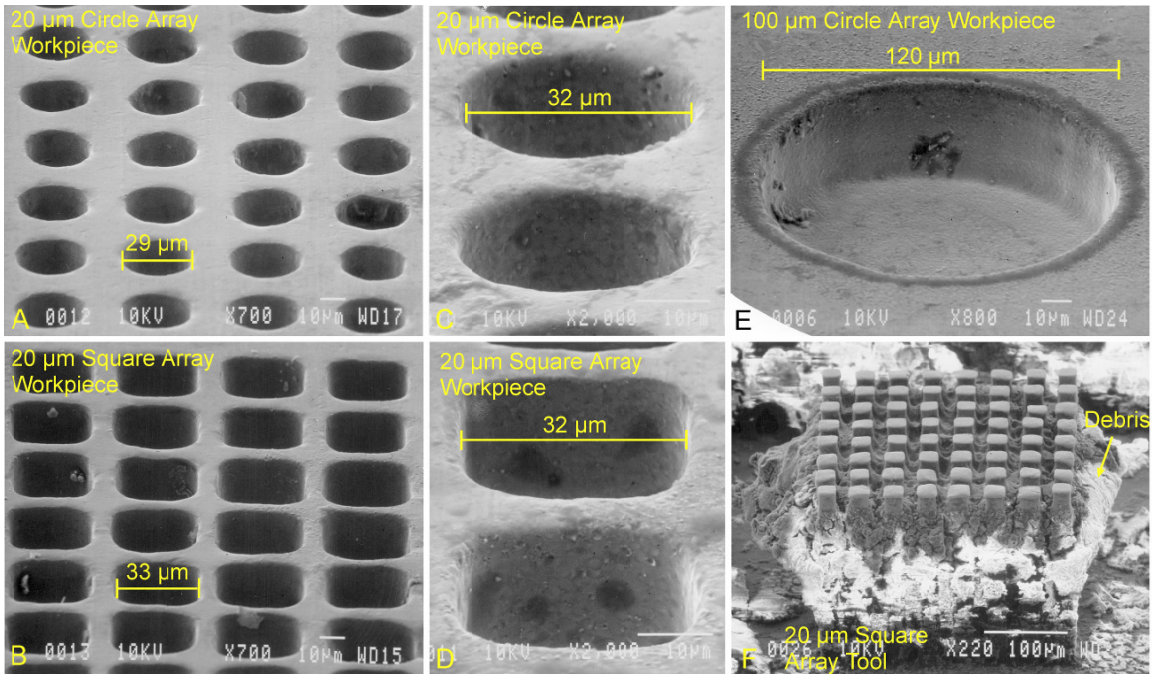

Fig. 2-17: SEM images A-D show workpieces of various widths. F shows the corresponding 20 µm tool for C. Note the extreme amounts of debris accumulated between features.

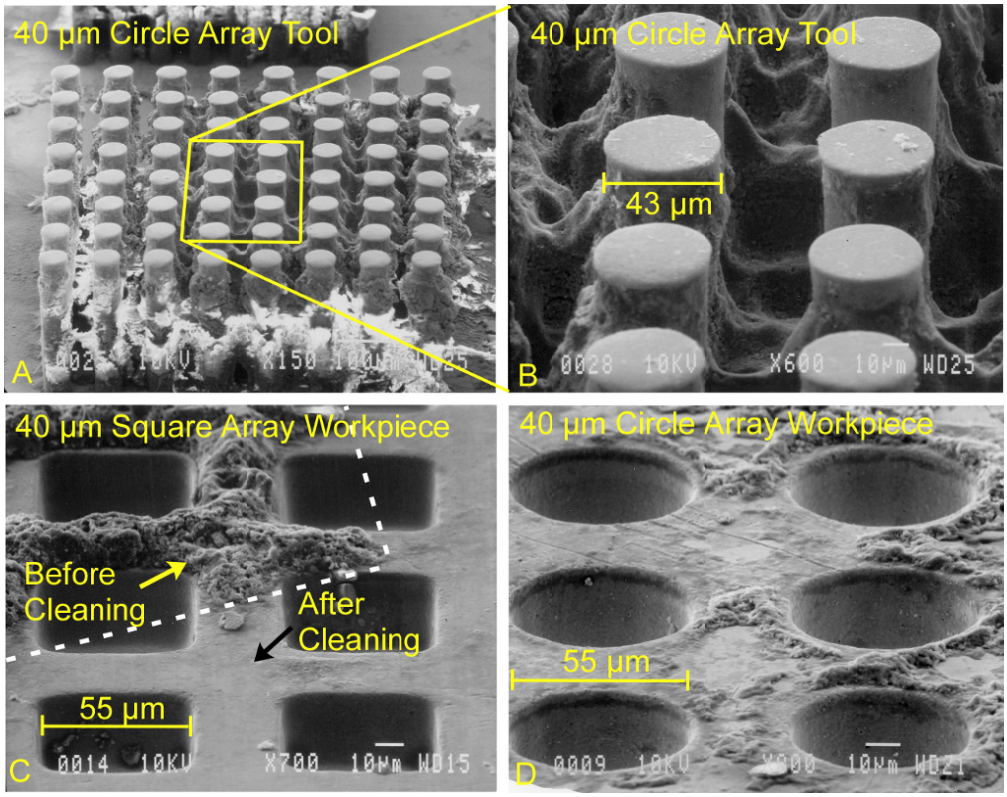

Fig. 2-18: More SEM images show larger 40 µm features. The debris in A is less severe than Fig. 2-14 but still significant. C and D show debris on the surface of the finished workpiece. C shows a section before and after cleaning.

The discharge gap of each feature across the diagonal of every array was measured using a digital filar eyepiece (Fig. 2-19). There are two trends that should be noted. The first is that discharge gap increases with increasing tool diameter, in agreement with the cross feature experiments. The second is that discharge gap increases in the center of each array, also in agreement with past work [Koch00]. Further, comparing the trend lines, the interior gap trend is shown to be even stronger as tool diameter increases.

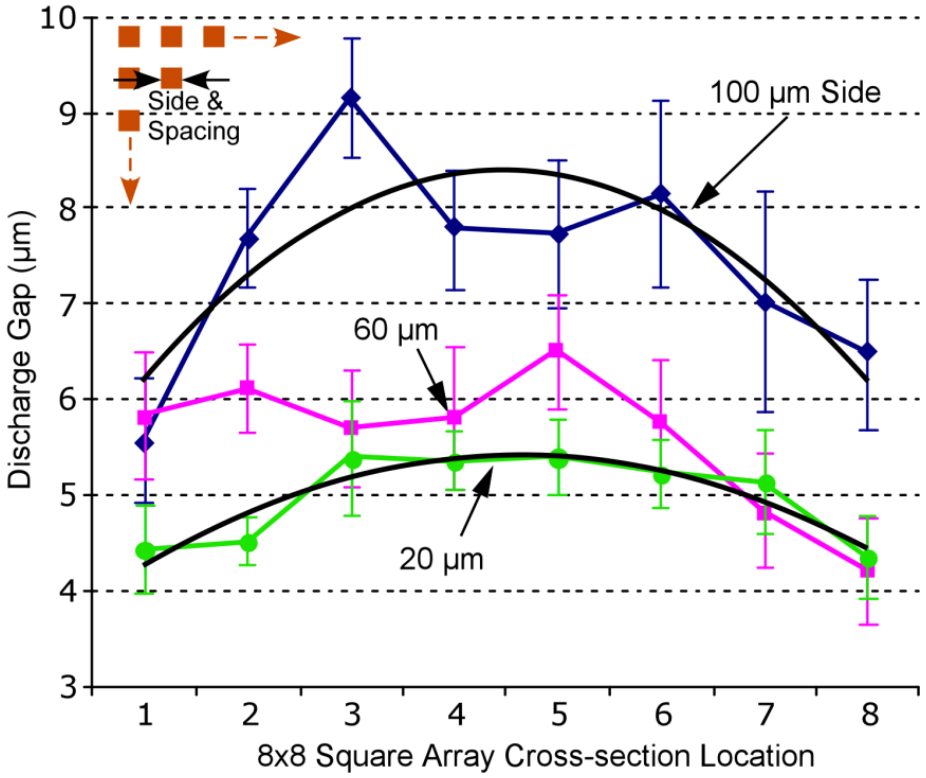

Fig. 2-19: Discharge gap vs. location along the diagonal of 8x8 arrays with 20,60,100 µm side features and corresponding 20,60,100 µm feature spacing. Discharge gap is larger in the center for all feature sizes. This effect is more pronounced as feature size increases, even though feature spacing also increases at the same rate. Error bars are one standard deviation from the mean (n=10).

2.5 Machining Resolution Study Conclusion

The integration of lithographically patterned tools with μEDM has the potential to remove a major throughput bottleneck in achieving precision micromachined patterns in bulk metal foils. The study presented above demonstrated that debris accumulation and gas trapping in high density batch μEDM can constrain precision in a significant way due to a corresponding increase in spurious discharges. By varying tool width and spacing in commonly used lithography patterns, the design space is illuminated.

In the single cross features, debris effects caused uneven discharge gaps and tool wear. Careful consideration should be taken with regard to compensating for tool wear around intersections and corners. Simulations of the hydraulic resistance for isolated line features indicate that debris is more likely to escape along the corners. The increased discharge gap in the center of large patterns should also be compensated. As features were packed closer and closer together in the parallel line features, debris effects increased. It was found that 10 μm lines required the lowest machining tolerance to produce a desired pattern with a tradeoff on tool wear but the 25 μm lines provide a more reasonable compromise. Finally, in the array study, it was shown that the non-uniform tool wear becomes worse as the size of the global pattern increases, even with the same fill factor.

This study provides motivation for developing new debris mitigation techniques that take advantage of the lithographic processes available during tool fabrication. The following chapters demonstrate two solutions for handling debris accumulation in high density batch μEDM.

CHAPTER 3

DEBRIS HANDLING TECHNIQUES

During μEDM, the presence of debris in the discharge gap lowers the threshold to initiate a discharge, causing spurious discharges on the sidewalls and base of the tool [Desc06, Tak05]. Protection from spurious discharges is especially important for high density patterns where debris tends to accumulate quickly. Uncontrolled debris accumulation can eventually cause heating and recasting of the features resulting in a mushroom shape. The new shape compromises not only the resolution of machined features, but also tool lifetime. This phenomenon, previously reported in [Tak05], is illustrated in Fig. 3-1A for the batch μEDM context.

Another factor is that a conductive particle can transport charge from one electrode to another and discharge at the opposite electrode [Tob96]. When this occurs in μEDM, debris particles generated during machining carry charge from the tool to the surface of the workpiece. The particles then discharge and damage the surface and edges of the workpiece. As debris accumulates between workpiece and tool, these discharges occur more and more frequently along with normal discharges. Eventually, a conductive bridge is formed that increases heat generation dramatically. Not only can this condition stall machining indefinitely, but it can also increase the discharge crater size by an order of magnitude and cause local welding of debris to both workpiece and tool [Son94, Tak05].

The plunge depth at which this stalling occured for the control pattern used in this study was approximately 25 µm.

This chapter introduces two techniques for limiting the impact of debris accumulation. Section 3.1 presents a passivated tool sidewall technique including design, fabrication, results and discussion. Section 3.2 introduces a two-step hydraulic debris flushing method for flushing debris away from the discharge gap and minimizing spurious discharges during machining. Experiment design and fabrication, hydraulic resistance modeling, results and a discussion section will be covered.

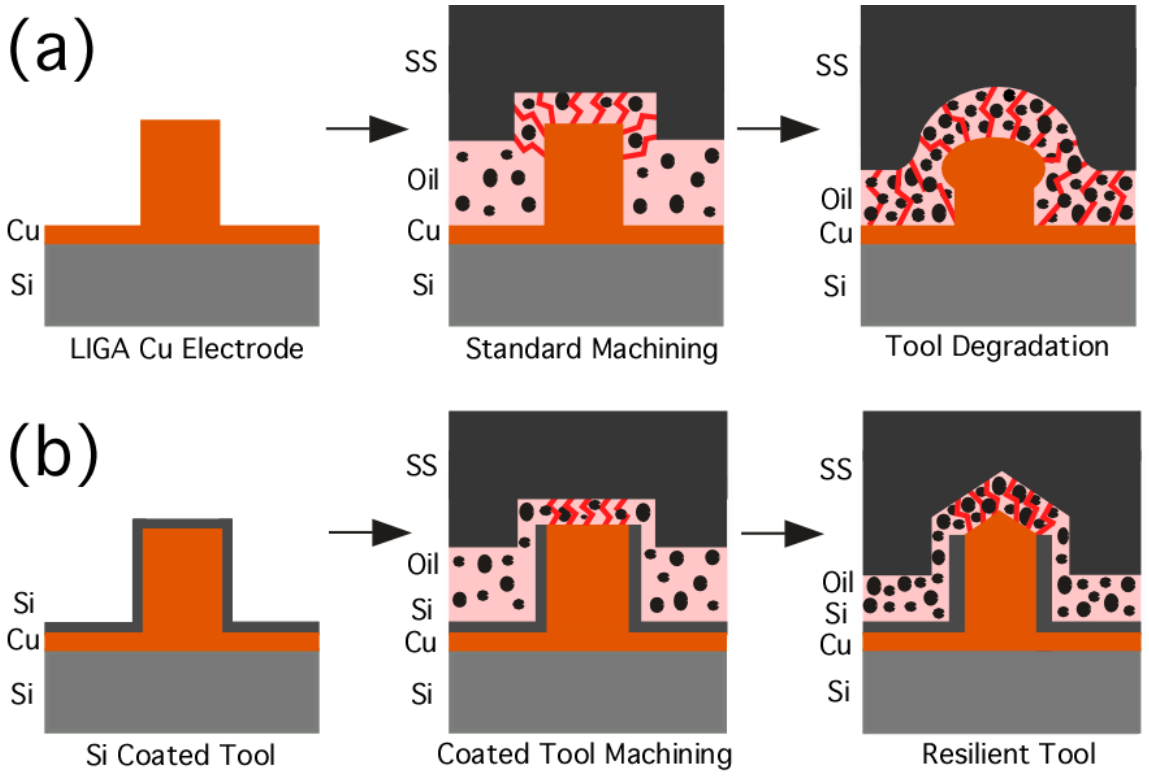

Fig. 3-1: (A) Comparison of machining progression for uncoated tool and (B) passivation coated tool. The coating is selectively removed from the top of the tool by µEDM against a planar surface. Rounded workpiece edges and melted tool result for the uncoated case and selective machining for coated case.

3.1 Tool Passivation Coating

3.1.1 Passivation Coated Tool Design

One way to improve the machining performance of batch mode μEDM is to add an insulating layer on the tool sidewalls to decrease spurious discharges (Fig. 3-1B). In [Kum03], for macro scale serial EDM, a PTFE tube surrounding the tool electrode was used with mixed results. In this study an insulating coating is integrated directly on a lithographically fabricated tool for batch μEDM. The purpose of a tool passivation coating is to provide protection from spurious discharges on the side and bottom surfaces of the tool by locally increasing the series resistance for spurious discharges (Fig. 3-1B). The primary requirements for this coating are a thin film that is conformal, insulating, and selectively removable at the top surface of the tool. Sputtered silicon was chosen for the coating material due to its relatively high resistivity, thermal conductivity, and hardness. At small thicknesses, it is also conductive enough to be selectively removed with μEDM by reversing the machining voltage polarity as the tool surface is brought to a flat workpiece. Then, when machining in normal polarity, discharges will occur preferentially at the top of the (copper) tool which offers the path of least resistance.

The hypothesized effects of spurious discharges and a sidewall passivation coating are added to the spark discharge model in Fig. 1-2 is shown in Fig. 3-2. The ideal discharge uses the reverse breakdown of the SCR breakdown to set the discharge voltage and R_p and L_p to shape the waveform. The discharge energy is set by R and C_e. When significant debris accumulates between the tool and the workpiece, the debris effectively shortens the discharge gap. This creates a parasitic discharge circuit with a lower breakdown voltage in parallel and potentially changing R_p and L_p. Depositing a sidewall

passivation coating adds a series resistance to the parasitic discharge along the sidewalls. The additional voltage drop compensates for the lower breakdown voltage, and discharges occur preferentially at the top of the tool, limiting spurious discharges at the sides.

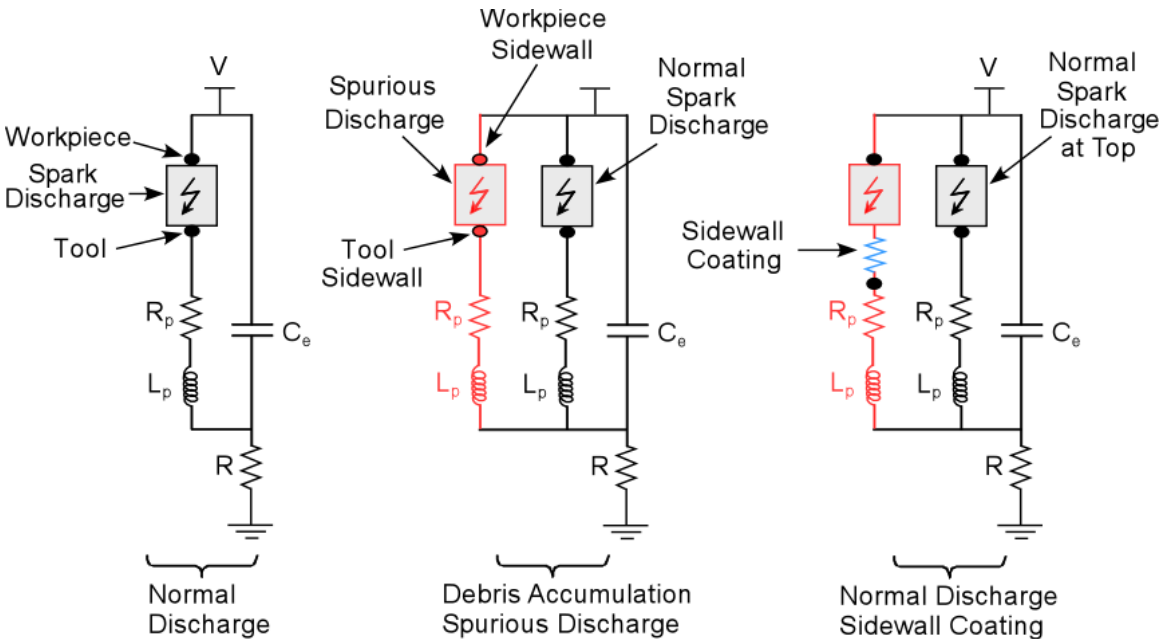

Fig. 3-2: Spark discharge model for ideal, debris dominated, and sidewall coated machining. A parasitic spark discharge is added by debris accumulation. The sidewall coating adds a series resistance to the spurious discharge path to compensate for the lower breakdown voltage.

Other advantages of silicon as a sidewall coating choice include a higher melting point than copper without softening whereas copper softens at 280° C [Kao04]. While silicon and copper do form a eutectic around 650° C [Bok02], this is much higher than the softening temperature of copper. The thin coating allows heat exchange from the copper to the oil but restricts heat generation to only the top surface of the tool where the discharges occur. A silicon coating may also help maintain tool edge resolution by preventing the copper from softening on the sides. As pattern density increases and/or

tool height decreases, even more limited fluid flow would further exacerbate these problems.

3.1.2 Passivated Tool Fabrication

An SU-8 UV LIGA process was used to fabricate 80 μm tall copper tools with 10 μm features. Since the sidewalls were not required to be precisely vertical, SU-8 UV LIGA provided a very economical and fast solution for high aspect ratio molds compared to X-ray LIGA. Microchem SU-8 2025 with various adhesion layers [Ude05] and a copper seed was used as a mold for copper sulfate electroplating. After lapping to planarize the top surface, a CF4 and O2 RIE plasma was used to strip the SU-8, yielding the control experiment structure in Fig. 3-1A. The 2 cm x 2 cm dies were then sputtered with a 500 Å titanium adhesion layer and either 1000 Å or 2000 Å of silicon as in Fig. 3-1B. From a processing perspective, silicon was chosen for the coating material since it is very resistive but still conducts enough to be electro-discharge machined at high voltages. As the copper tool wears down (slower than normal), the silicon coating wears down as well. The die with 2000 Å of Si was used since the coating proved machinable and was more resistive.

Table 3.1: Machining conditions for coating μEDM

	Coating Removal	**Machining**
Voltage (VDC)	90-100	-70
Z-Feed(μm/s)	0.4	0.4
Stage Dither (μm)	None	~10
Plunge (μm)	2	25

A 250-350 µm thick 7 mm x 6 mm #304 stainless steel workpiece cut from a foil was then mounted to the mandrel using silver epoxy. Electrical contact was made to the tool directly on the copper seed in an area which was not coated. Setting the voltage of the coated tool to act as the workpiece, the silicon and titanium on the top surface of the tool were machined off with the stainless steel. In a new area of steel, the polarity was reversed and the tool plunged 25 µm into the steel. Machining parameters are listed in Table 3.1 and were chosen to minimize discharge energy, sacrificing machining time. The silicon coated tool preferentially machined at the top since the resistive path was significantly lower there. The test pattern was similar to that used in an DC-to-DC boost converter [Ude05]. The same pattern was machined using a tool with the coating and a tool without the coating.

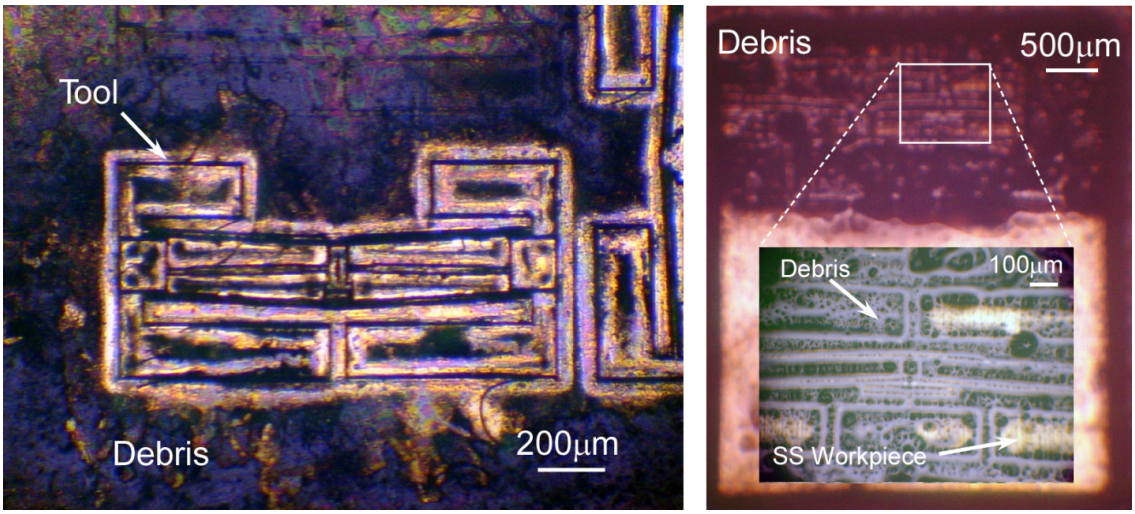

Fig. 3-3: Left: The silicon coated tool after machining with significant debris surrounding. Right: workpiece directly after machining with debris coating surface.

3.1.3 Experimental Results

An example of the debris remaining on the silicon coated tool (left) and workpiece (right) after machining but before cleaning is shown in Fig. 3-3. Simple dither agitation is not enough to flush the debris away during machining. There is enough debris to span the full thickness between the workpiece and tool. Stopping machining to separate and flush the discharge gap can work if the pattern is not too dense, but this takes away the primary advantage of batch μEDM, high material removal rate at precision dimensions.

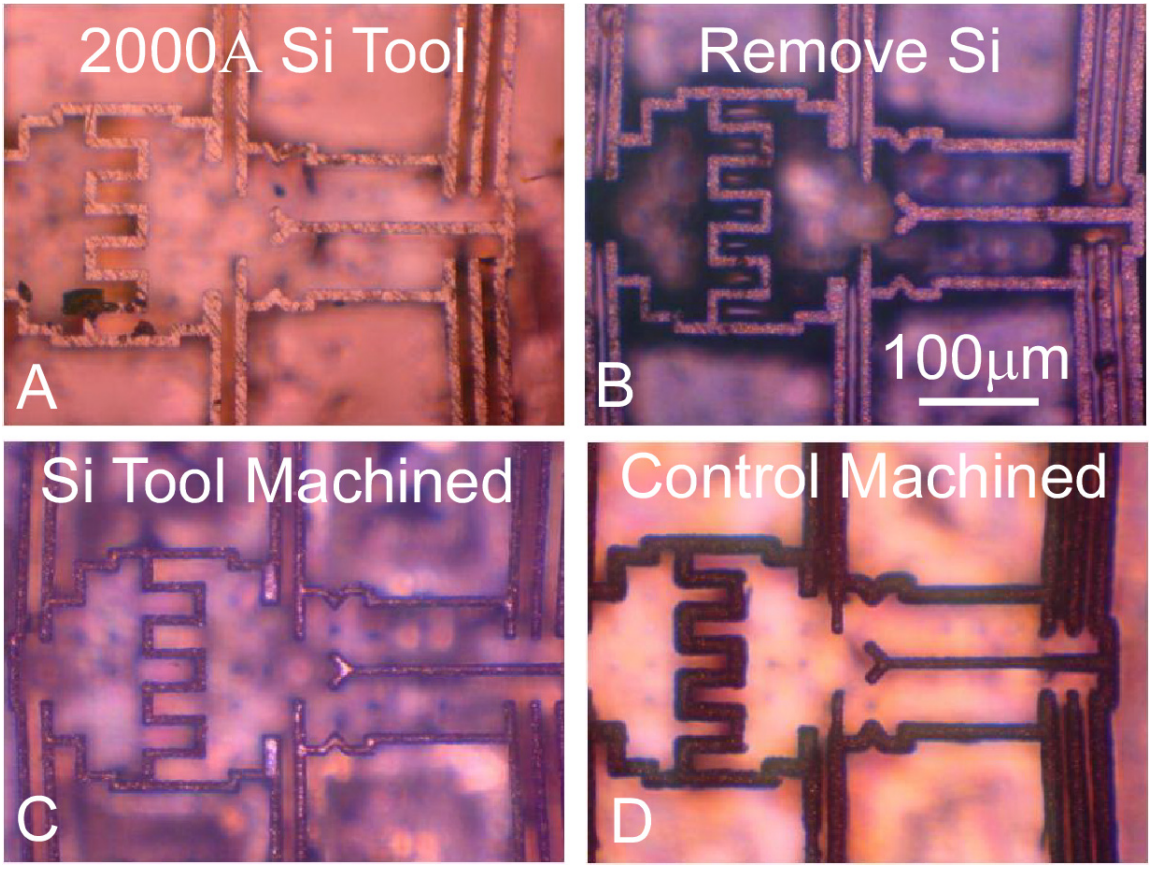

Fig. 3-4: Optical photos of the test pattern. First 2000Å of Si are deposited on the copper tool (A). Next (B) the silicon is removed from just the top surface by reverse polarity EDM. Then machined in C. The uncoated tool in D has much wider after machining.

The magnified optical images in Fig. 3-4 show what is happening in more detail. The copper tool is first coated with 2000 Å of Si in A, then just the top surface is removed by reverse polarity µEDM in B. The tool is used to machine 25 µm of stainless steel and still has well defined edges afterward. The uncoated tool is compared as a control experiment in D and the rounded edges of the tool are easily visible, especially in the more feature dense areas.

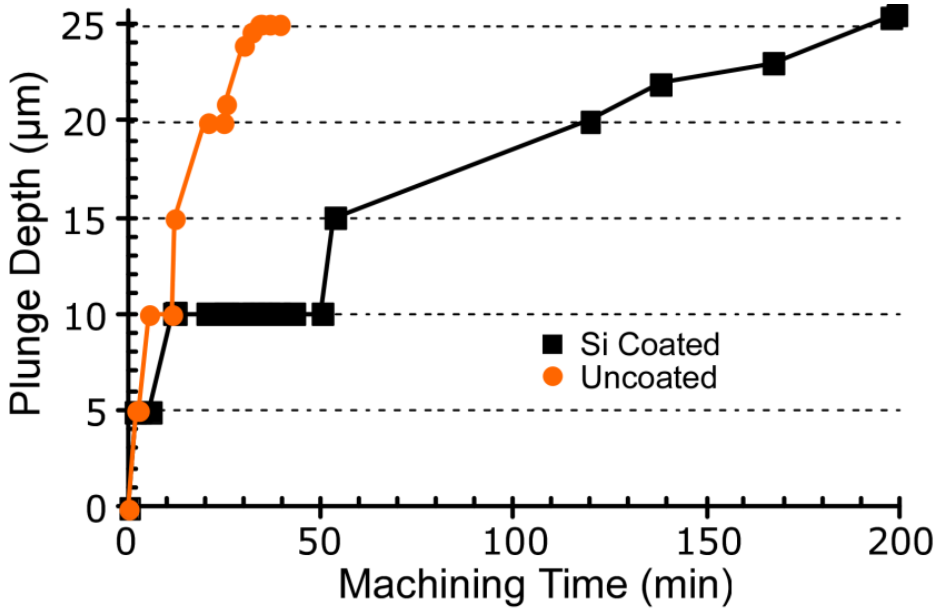

Fig. 3-5: A measurement of plunge depth vs. machining time shows that the uncoated case reached 25µm quickly while the coated case stalled. This is because the uncoated tool wears down rapidly, and provides a machining depth that is much smaller than the plunge depth.

In Fig. 3-5 the time to reach a plunge depth of 25 µm was 34 minutes for the uncoated tool and 3 hours, 18 minutes for the coated tool. The uncoated machining (plunge depth) progressed steadily with only minor pauses until reaching the 25 µm mark. The coated machining meanwhile stalled for about 45 minutes before progressing at a slower rate past 10 µm. A stall is defined as the EDM control unit cyclically separating the tool from the

workpiece because a short circuit was detected and then attempting to resume machining. While the uncoated tool machined faster, this result is misleading. As will be described, the uncoated tool destroyed itself as it machined and did not actually achieve the plunge depth. The coated tool did and remained intact.

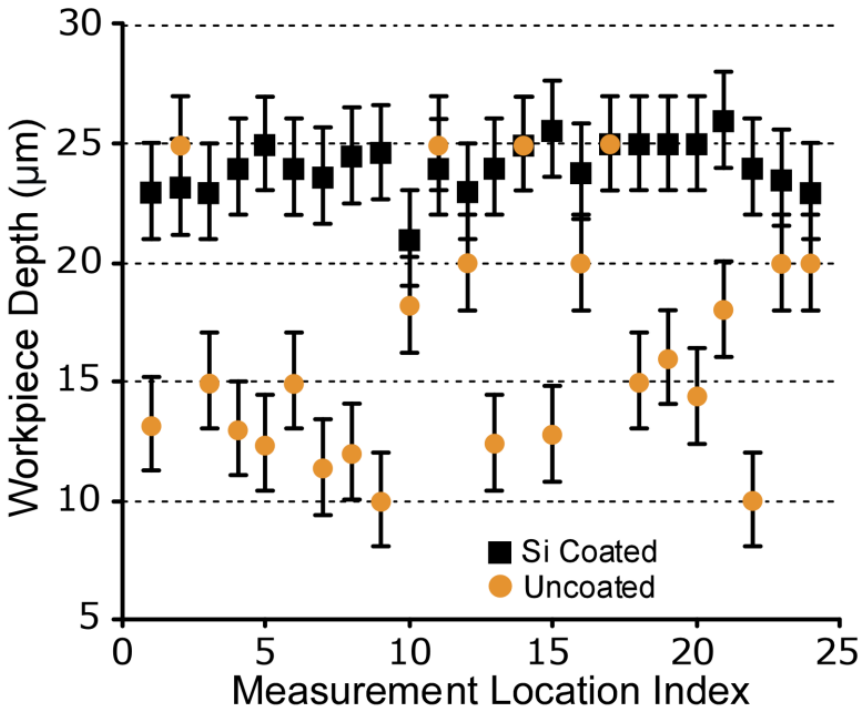

Fig. 3-6: Comparison of machined workpiece depth at several locations across test pattern after plunging the tool 25 µm. The uncoated workpiece did not machine the full 25 µm in most areas and also varied excessively across the pattern compared to coated case. This difference in machined depth would account for the faster machining time for the uncoated case. Error bars are an estimate of the error in the measurement technique (n=5).

Figure 3-6 shows data on the actual workpiece machining depth for various locations. Measurements were taken by focusing on the top surface of the workpiece at 500x magnification, focusing on the bottom surface of the measurement location, and recording the difference on the glass scale on a Karl Suss probe station. Each data point

represents the average of five measurements. The mean actual machined depth for the uncoated tool was 16.6 µm while the coated tool was 24.1 µm. This corresponds to depth errors of 33.6% and 3.6% respectively for an expected depth of 25 µm. This large difference can explain why the uncoated machining reached the target plunge depth so quickly. The uncoated tool was not machining the entire depth. The depth of machining was also more uniform for the coated case. A standard deviation of 4.9 µm was calculated for the uncoated case compared to 1.1 µm for the coated, which is a 78% improvement.

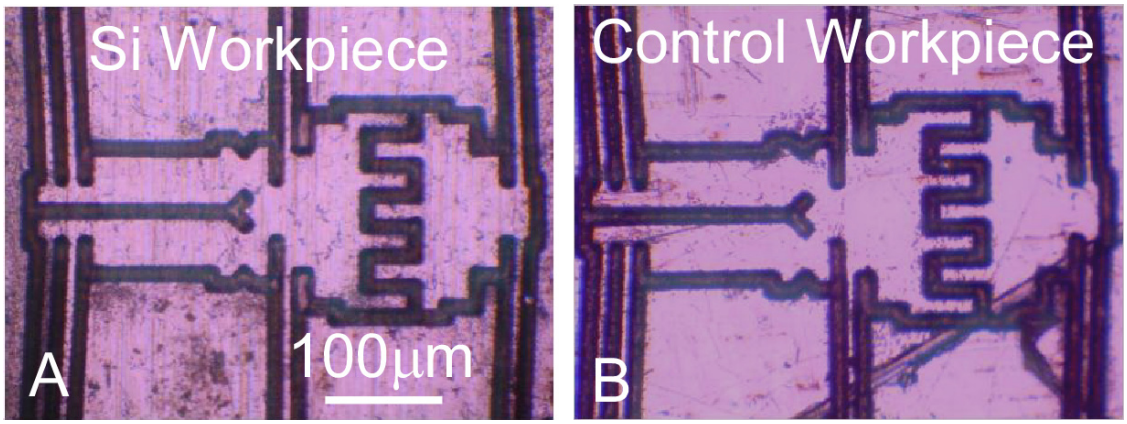

Fig. 3-7: Differences in the optical images of workpieces (A,B) are difficult to see without SEM magnification.

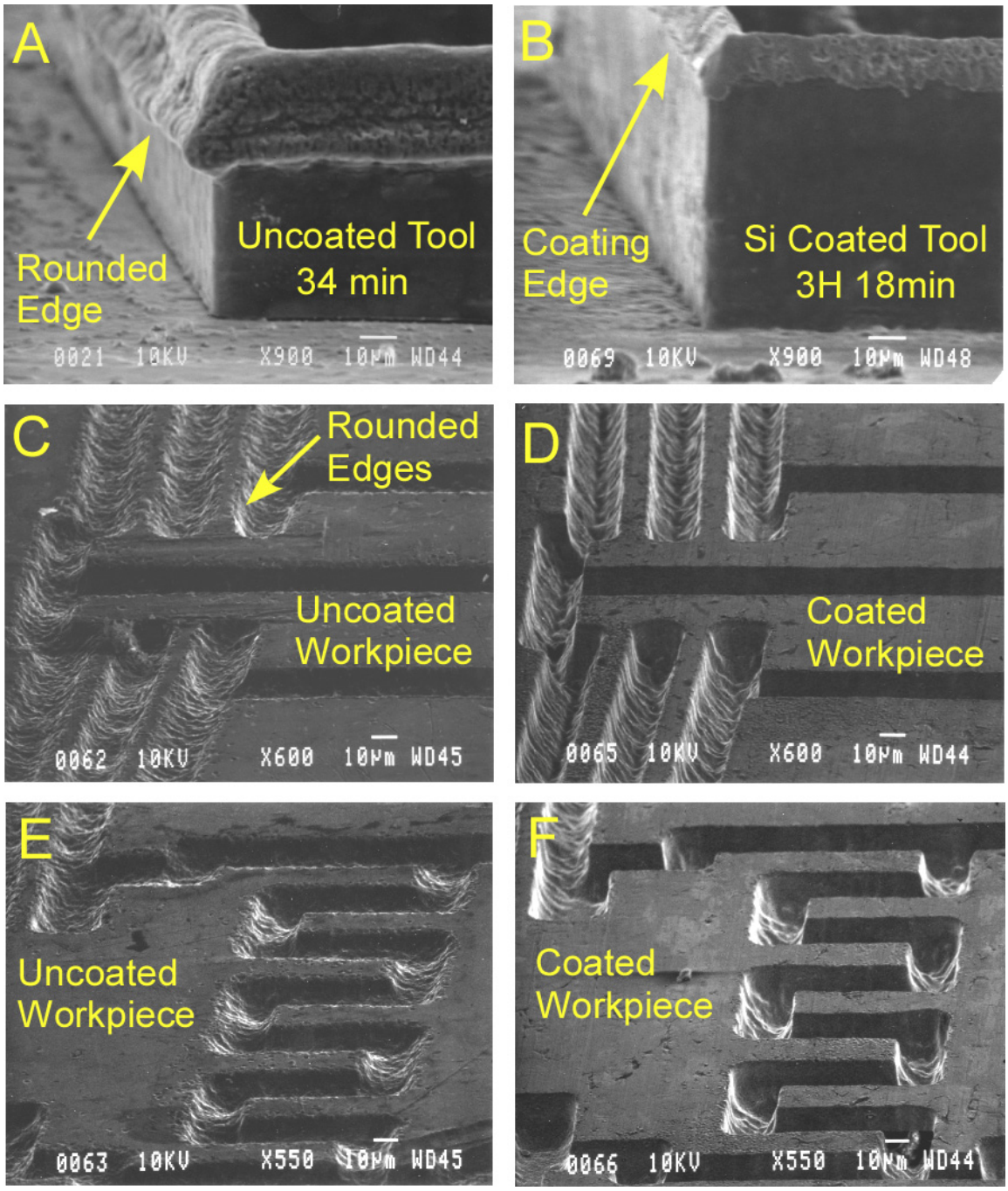

Fig. 3-8: A: Uncoated tool recasts into a mushroom shape after machining. B: Silicon coated tool has negligible wear. C,E: Uncoated workpiece with feature rounding, edge rounding, and rough surfaces. D,F: Coated workpiece with sharp features, sharp edges especially on corners, better surface finish, and much deeper machining.

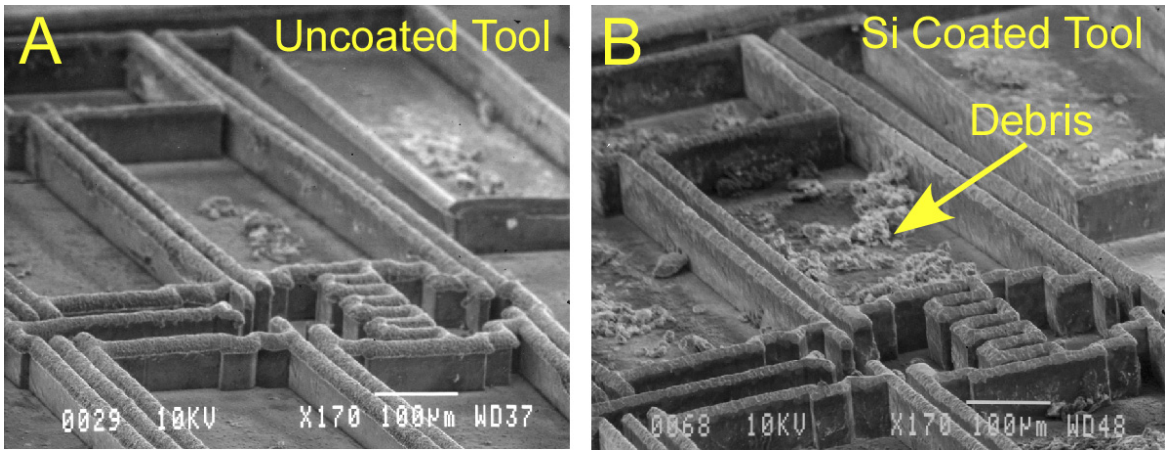

Fig. 3-9: A: Used uncoated tool has rounded edges across all features. B: Used coated tool with low wear and large debris on surface.

The workpieces in 3-7 A and B look very similar but the long beams look wider for the silicon tool. More detail can be seen in the SEM images. Figures 3-8A and 3-9B show typical 80 µm tall tool features after plunging 25 µm. The mushroom shape at the top of the tool is believed to have caused rounding of the workpiece edges in Fig. 3-7C,E. The silicon coated tool remained vertical despite machining for a significantly longer time. The edge of the coated tool is also visible a short distance from the top surface. This indicates that the coating probably does not interfere with a normal discharge from occurring at the top but does prevent discharges along the sides as intended.

The workpiece from the coated tool machining in Fig. 3-8D,F has very sharp edges, smoother surfaces, and is visibly deeper. From the lower magnification view in Fig. 3-9A and B the rounded edges of the tool are visible across the entire pattern. There is also a significant amount of residual debris trapped within the pattern of the silicon coated tool after machining. This debris is another factor to consider when comparing the long machine time of the coated tool case.

Another SEM image comparison of uncoated vs coated machining workpiece results is shown in Fig. 3-10. These are similar results to Fig. 3-8C,D but note the 4.5 µm wide been is 1 mm long. The top surface is much smoother and the edges are more distinct in the silicon coated case. The impact of the damage on the top surface of the structure is covered in chapter 5.

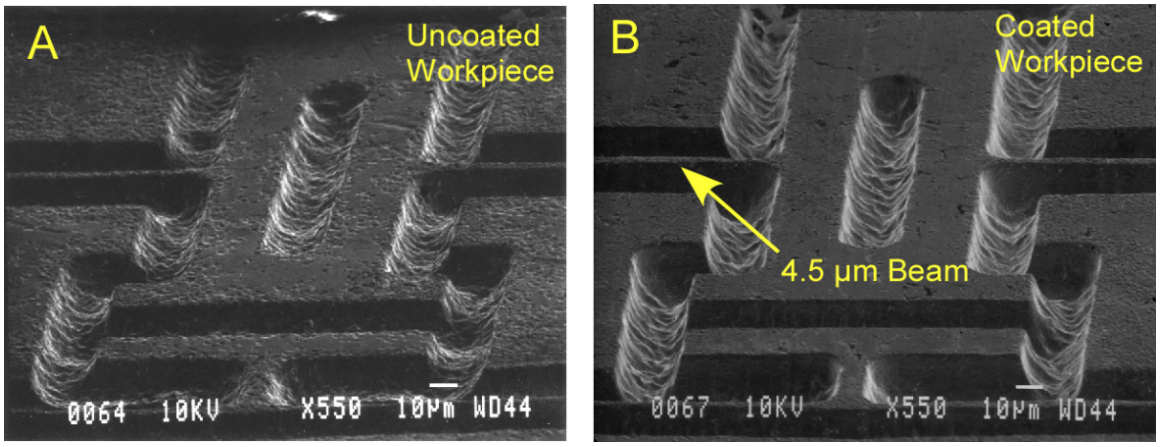

Fig. 3-10: A) Workpiece for uncoated case with much more surface roughness than B) coated case. 4.5µm wide, 1mm long beams.

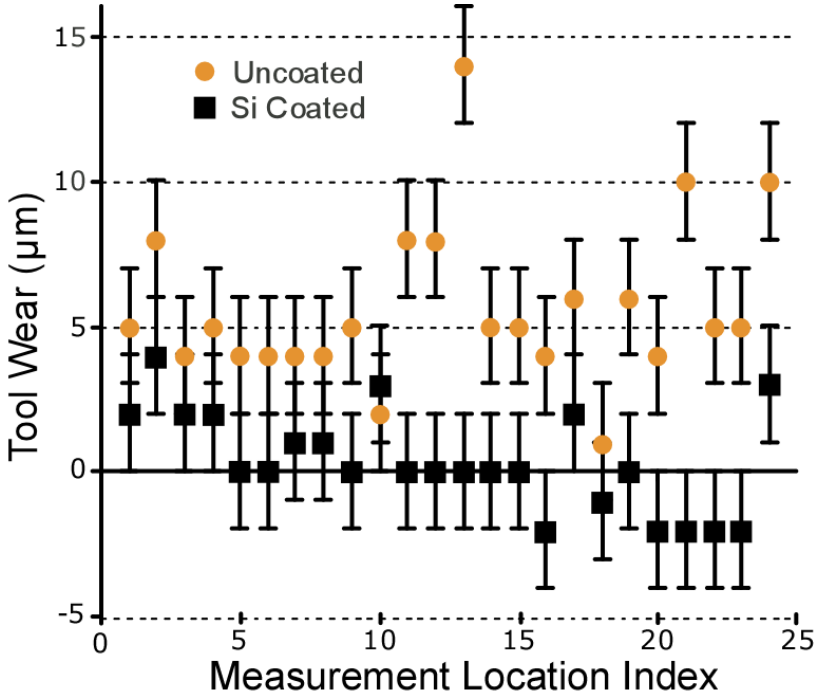

Fig. 3-11: Si coated tool wear was less than uncoated tool.

The tool wear at the same locations from Fig. 3-6 is shown in Fig. 3-11 and used the same measurement technique except with the base of the tool as the zero point. The mean control tool wear across all data points was 5.7 µm for the uncoated tool compared to 0.4 µm for the coated tool. The tool wear rate is the mean tool wear divided by the mean actual machined depth. The uncoated case had a typical tool wear rate of 34% and the coated case had a typical rate of 1.7% despite machining significantly deeper and longer.

Figure 3-12 shows the transition between a section of tool that was used during machining and a section that was not. The workpiece did not cover the entire tool for this experiment. The edge rounding of the uncoated tool is clearly visible when contrasted with the unmachined section. Figure 3-12B is a side profile of the transition for the coated tool. The edge of the silicon coating and the low tool wear can be seen.

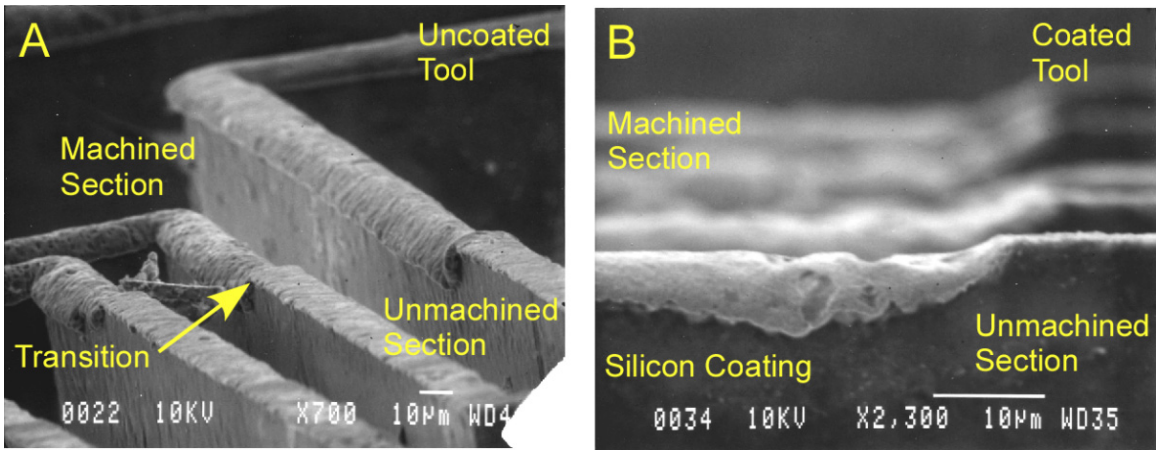

Fig. 3-12: A) Uncoated tool transition from unmachined (bottom) to rounded shape (top). B) Si coating wears down as copper wears slowly. Right side is unmachined, left side shows exposed copper top.

3.1.4 Discussion

As feature density increases, debris accumulation becomes a major concern because there is no efficient mechanism for removal. Machining took longer with the coated tools, presumably because debris accumulated in the discharge gap are slowly pulverized and flushed away. Debris accumulated in the tool shown in Fig. 3-9B may have also contributed to slow machining. The EDM controller repeatedly detected short circuits and backed the tool out completely before progressing slowly to remove the blockage. Spurious discharges on the sidewalls may in fact provide a mechanism to break down debris into finer pieces and facilitate better flushing. In uncoated tools, the mushrooming may have also allowed for comparatively more efficient debris removal by limiting the actual depth of machining. However, the faster machining time in these tools comes at the cost of surface quality, machining depth, depth uniformity, and tool wear. At even greater machining depths, debris accumulation and mushroom shaped recasting exacerbate the problems further.

A new passivated tool electrode process for batch mode μEDM was investigated that preliminarily addresses these problems. It is easily integrated with any die-sinker or serial type electrical machining process to significantly reduce spurious discharges. This could include machining techniques outside of μEDM such as electrochemical discharge machining. While machining time increased due to debris accumulation, mushroom shaped recasting was eliminated and tool wear was negligible. The workpiece machined with the coated tool had significantly better feature and edge definition, smoother surfaces, was deeper, and more uniform than the uncoated workpiece. The test patterns included

4.5 μm wide, 25 μm tall and 1 mm long unreleased stainless steel beams. A silicon passivation coating provides one component of a high density batch μEDM solution. It extends the usable life of a tool but does not eliminate the debris. By combining a passivation coating with an integrated flushing technique, described next, a more complete solution for batch mode μEDM emerges.

3.2 Hydraulic Flushing

As noted in sections 3.1 and 3.1.4, debris accumulation in the discharge gap leads to spurious discharges that can damage the tool and workpiece. Even with a passivated tool sidewall coating, the speed of machining is severely degraded. Removing debris entirely is therefore a priority for high quality and high efficiency machining. Unfortunately, traditional dither flushing becomes more and more inefficient when feature densities increase as well as when the patterns are enclosed. An example of an enclosed pattern is a solid wall feature around the perimeter of other, internal, features which will prevent fluid flow and trap debris inside.

This section introduces a two-step hydraulic debris flushing method for flushing debris away from the discharge gap and minimizing spurious discharges during machining. By first batch machining narrow through-holes in the workpiece, a path is created for the debris to escape when the second, overlaid finishing pattern, is machined (Fig. 3-13). Self-generated bubbles from the discharge process entrain debris particles and carry them away from the discharge gap [Kan97, Yu02].

Section 3.2.1 presents the design approach and tool fabrication. Section 3.2.2 models the effectiveness of the new flushing method compared to standard dither flushing.

Section 3.2.3 presents the experimental results with and standard and hydraulic flushing. Finally section 3.2.4 is a discussion of the impact this technique can have on batch mode μEDM.

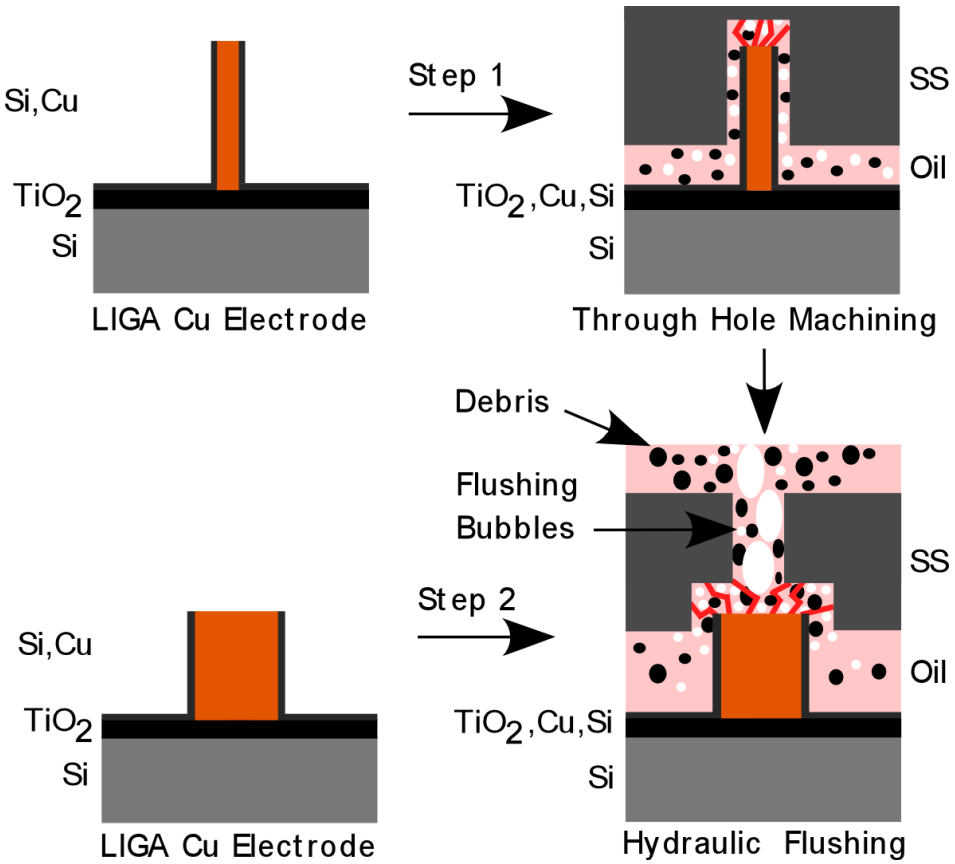

Fig. 3-13: Machining process for 2-step hydraulic debris flushing. Step 1: machine narrow through-holes, Step 2: Overlay workpiece on new tool area and machine finished pattern. Flushing bubbles and tool dither force debris out the through-hole.

3.2.1 Tool Design and Fabrication

The control experiment pattern consisted of four large holes within an enclosed perimeter to represent structures with large machining fill-factors. These patterns are resistant to flushing by the normal vertical tool dither in dielectric oil (Table 3.2). In

these types of patterns, debris generated by µEDM accumulates within the perimeter and forms conductive paths to the workpiece, causing machining to stall indefinitely.

Table 3.2: Debris study machining conditions.

Tool Height	175µm
Finish Hole	120x120µm
Wall Thickness	40µm
Wall Spacing	120µm
Z-Feed	0.2µm/s
Plunge	41, 80µm

In the two-step design, locating the through-holes in the field region of the final die does not disrupt the finished pattern (Fig. 3-14). In this study the through-holes were formed by 60 µm x 60 µm posts located on the tool die next to the actual pattern. Thus, the workpiece was machined sequentially by two different parts of the tool die in separate steps.

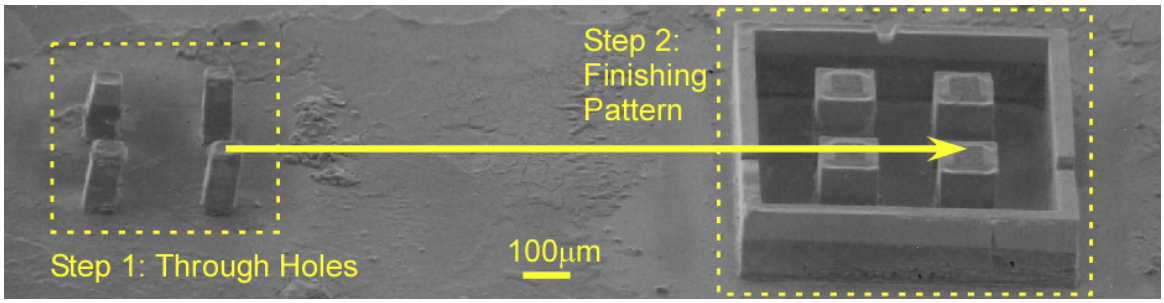

Fig. 3-14: Hydraulic debris flushing test pattern post machining. Through-holes at left while walled finishing structure at right.

Copper tools ranging from 175-200 µm tall for both control, and two-step patterns were fabricated with the process described in the parametric study section. A 2000 Å silicon passivation coating was used as described in the previous section. These tools were used to machine patterns part way into 100 µm 316L stainless steel using the same machining conditions from the parametric study.

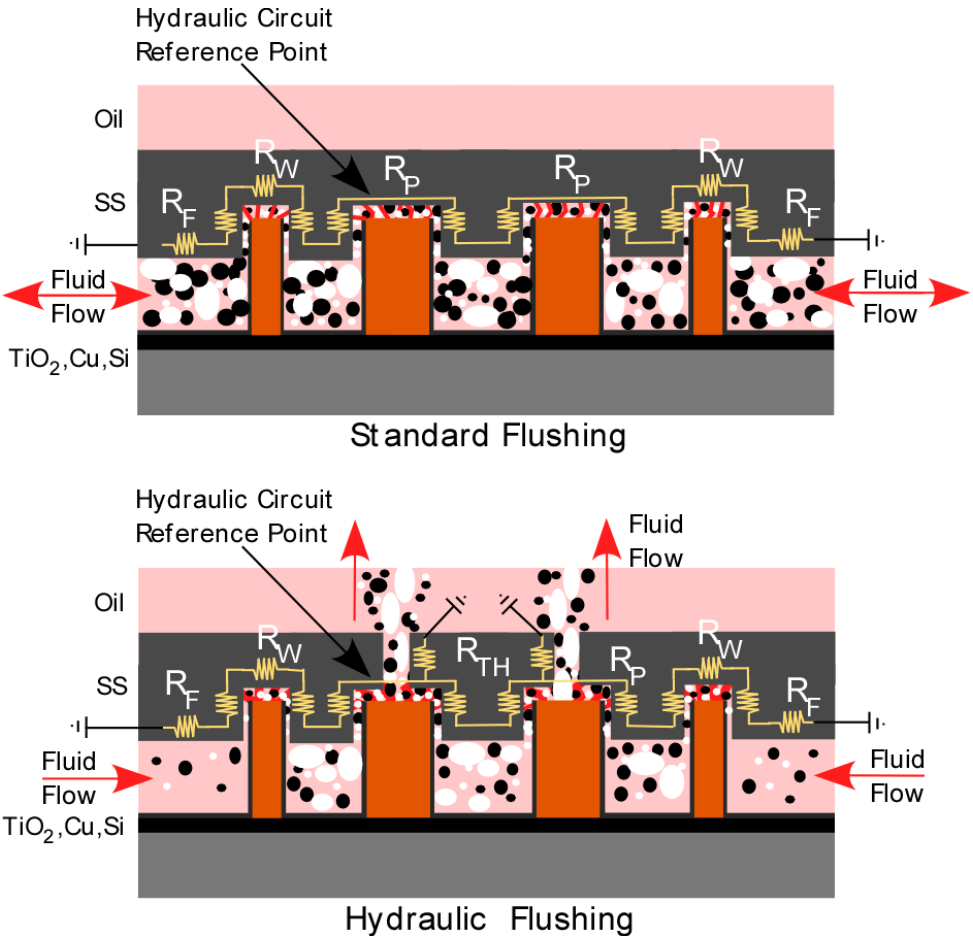

Fig. 3-15: Cross-section of hydraulic resistance circuit for standard dither flushing (top) and hydraulic flushing (bottom). Through-holes provide a shunt path for debris to escape by bubble entrainment.

3.2.2 Modeling

The performance of the hydraulic debris removal technique cannot readily be fully modeled since it is a complex three-phase flow with changing boundary conditions. Gas

and debris particulate generation occurs at unknown rates. Significant but localized fluctuations in temperature and pressure fluctuations result from the spark discharges. The vertical dither of the tool also complicates the model. The standard debris removal mechanism involves fluid flow from the vertical tool dither and gas bubble entrainment. These effects are difficult to quantify with observation in batch mode. However, by assuming laminar flow, we can compare the hydraulic resistance at the locations of debris generation for a single point in time to gain some qualitative insight on the removal rates of the standard mechanism and the hydraulic mechanism.

For laminar flow, the hydraulic resistance of a rectangular channel is given by equation 3.1:

.

$$R = \frac{12\eta L}{H^3 W - \frac{192}{\pi^5} H^4 \sum_{m=0}^{\infty} (2m+1)^{-5} \tanh[\frac{(2m+1)\pi W}{2H}]} \tag{3.1}$$

For a preliminary comparison it is sufficient to examine the relative impact on an equivalent uniaxial hydraulic resistance. A cross-section of the hydraulic circuit for the enclosed perimeter is shown in Fig. 3-15 and the full pattern is shown in Fig. 3-17C,D. The point of reference for the model is at an inner post with plunge depth of 40 μm and a discharge gap (channel height H) of 6 μm. To simplify the calculation for R_{Wall}, the outer wall can be represented as a rectangle of width W and flow channel length L_{Wall}. Here, W is the perimeter of the feature whereas

$$L_{Wall} = 2 \times (Plunge\_Depth) + (Wall\_Width) \tag{3.2}$$

A similar method is used for R_{Post} and R_{Field}. (Note that this equivalent width approach for square annular hydraulic resistance is about 36% too low compared to the Fluent™ simulations from the parametric study). Therefore, these calculations can be easily compensated to obtain good accuracy with much less simulation time. Since the area of the workpiece field is much larger than the machined feature, a channel length of 2 mm is assumed for R_{Field}. The total hydraulic resistance for the standard flushing method is then:

$$R_{ST} = R_{Post} + R_{Wall} + R_{Field} \qquad (3.3)$$

The total resistance for hydraulic flushing is:

$$R_{HY} = (R_{Post} + R_{Wall} + R_{Field}) // R_{TH1} // (R_{TH2-4} + 2R_{Post}) \qquad (3.4)$$

Where R_{TH1-4} represent the four through-hole fluidic channels. Using the dimensions stated in Table 3.2 and using m=1-10^5, the analytically estimated resistances are: R_{Post}=6.96x10^{12}, R_{Wall}=4.39x10^{12}, R_{Field}=6.50x10^9, and R_{TH}=2.31x10^{11} Pa-s/m^3. This gives R_{ST}=1.14x10^{13} and R_{HY}=2.16x10^{11}, a 53x reduction in steady state hydraulic resistance.

3.2.3 Results

The enclosed perimeter patterns were machined into the workpiece as deep as possible. The standard flushing pattern stalled indefinitely at a tool plunge depth of 41.3 µm due to debris accumulation. The hydraulic pattern plunged 125 µm for the through-holes and then 80 µm for the walled structure before being stopped manually. During the second step, the bubbles generated during machining coalesced almost exclusively within the wall perimeter. Very few bubbles were visible escaping out the sides. As the bubbles rose up the through-holes they entrained debris particles and flushed them out (Fig. 3-16). Bubble size is important because in fluidization column systems, the larger the gas bubbles, the more efficient the solid particle removal [Kan97, Yeo99A].

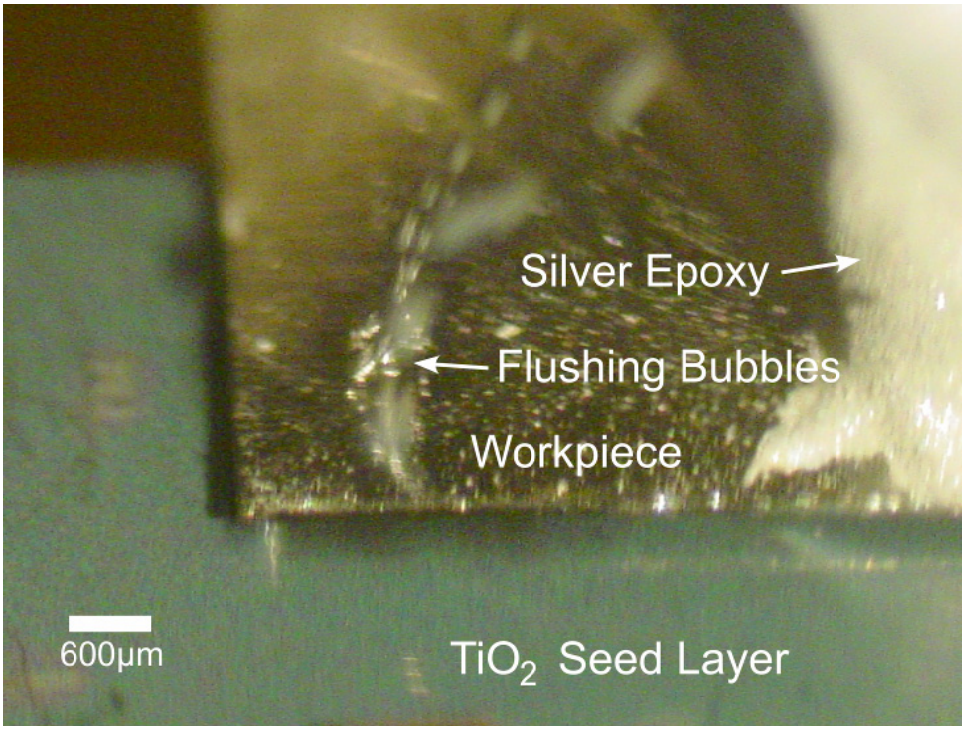

Fig. 3-16: Hydraulic debris flushing through workpiece utilizing bubbles from discharge and vertical dither of tool.

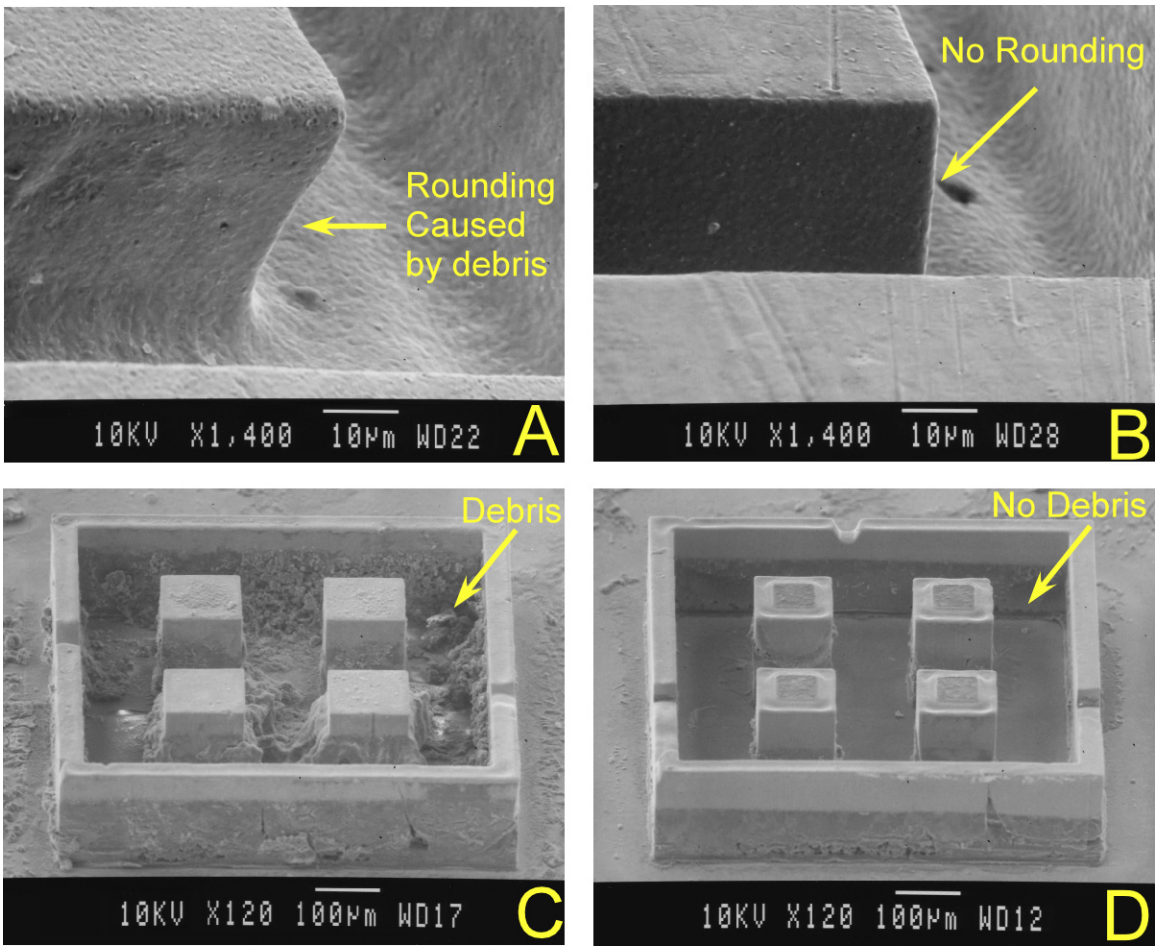

Fig. 3-17A-D: Enclosed workpiece (41 µm deep, 1h43m) (A) with no flushing. Rough surface on top and sidewalls, angled corner edge. Flushing workpiece (80 µm deep, 1h59m) (B) shows clean sidewall and top surface, sharp corner. Grain structure is still visible on top surface. Enclosed tool feature after machining (C) has a lot of residual debris while flushing tool feature (D) does not. Both utilized Si coated sidewalls.

SEM images of the machined workpiece and tools show that the two-step procedure had a dramatic impact on dimensional tolerance, sidewall angle, surface finish, and device height (Fig. 3-17). While the top surface of the standard flushed workpiece has very rough surfaces the original grain structure is still visible on the top surface of the hydraulically flushed workpiece. The images of the tools after machining show very significant debris accumulation inside the enclosed wall perimeter. This is the same scenario that happens in high density patterns. The images in Fig. 3-18 show the

workpiece from a further distance. The debris inside the perimeter is stuck to the top surface in several places whereas the top surface of the flushed workpiece is clean. A view of a concave corner feature of the workpiece shows some pits in the sidewall and debris on the top surface of the control workpiece in Fig. 3-19. The flushed workpiece has a smooth surface like the convex feature in Fig. 3-17B and sharp edges.

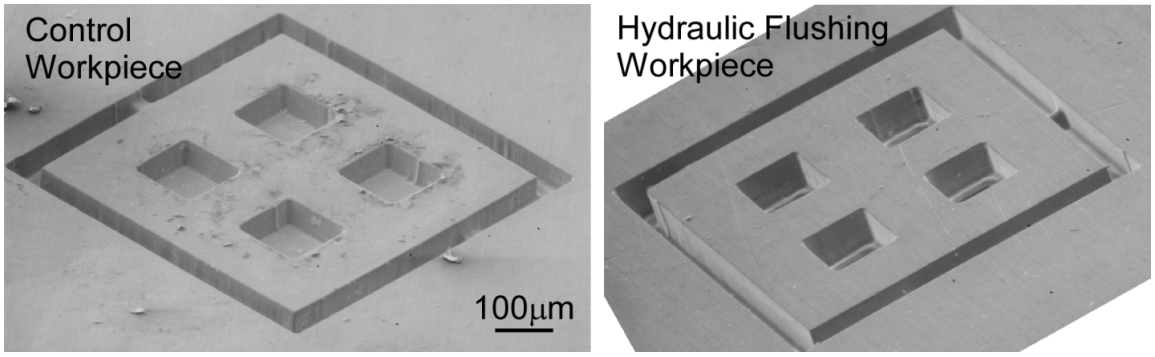

Fig. 3-18: Workpiece after machining for Left: regular flushing had debris fused to the surface and Right: hydraulic flushing had very clean, sharp surfaces.

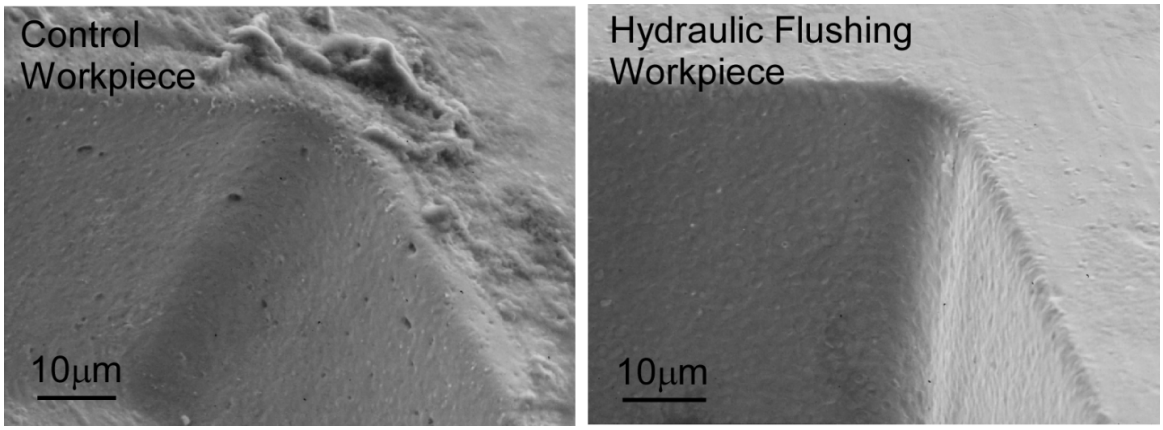

Fig. 3-19: Workpiece detail shows Left: pits in the sidewall of the control workpiece from spurious discharges and debris on the surface. Right: smooth sidewalls and clean top surface.

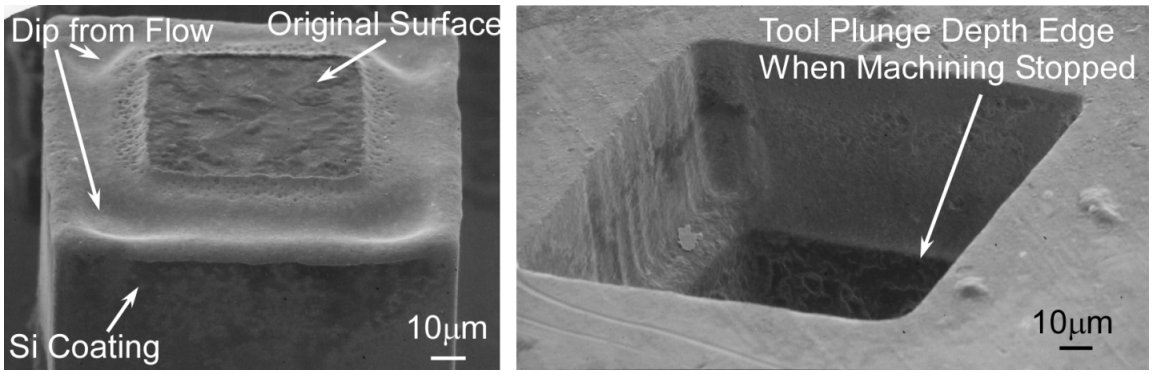

Fig. 3-20: Left: hydraulic flushing inner tool detail shows the silicon coating starting to erode and some reshaping from the debris flow pattern. Right: corresponding workpiece hole shows the ridge at the point where machining was purposely stopped.

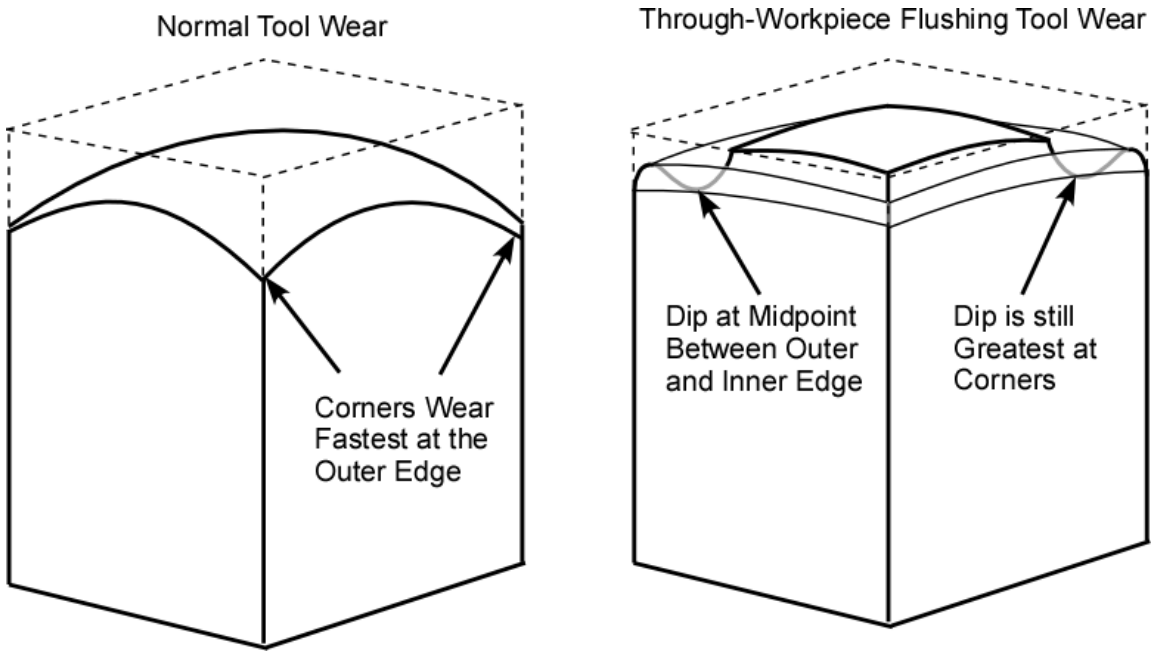

Fig. 3-21: Tool wear for a normal tool is greatest at the edges of the feature at the corners. The through-workpiece finishing tool had a different patter with a dip between the outer and inner edges of the machining area. The dip was largest at the corners.

A closer look at one of the inner finishing tools for the flushing case shows some interesting detail on the wear pattern (Fig. 3-20). There is a dip in the middle of the ring area that is doing the machining and it is deepest at the four corners where the flow should be the highest according to Fluent simulation from chapter two. What is interesting is that the edges on tools normally are rounded out after machining because

the electric field is highest at those points and normally initiates the discharges. These corners however had less wear than the high flow area as diagramed in Fig. 3-21. The corners of the regular tool in 3-17C and the left image of 3-21 had the normal wear pattern because the debris was escaping down the sides. If this wear pattern is consistent, it could mean that tools with hydraulic flushing would not need to advance as far beyond the finished hole in order to remove burrs. The corresponding workpiece hole for this tool is shown at the right of Fig. 3-20. The ridge where machining was purposely stopped is visible at the bottom.

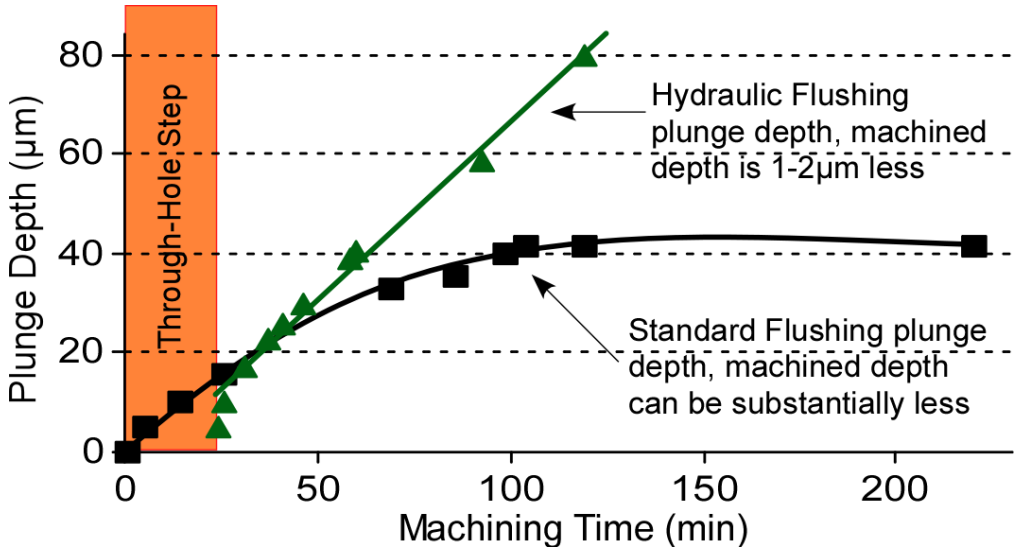

Fig. 3-22: Plunge depth vs. machining time for standard flushing and two-step hydraulic flushing. The standard walled pattern self terminates at 40 µm. Two-step process required an initial through-hole step but eventually surpassed the plunge depth of the standard case and maintained a linear trend for each step.

Figure 3-22 plots the plunge depth over time for the two flushing methods. Despite machining twice as deep, the two-step flushing method progressed much faster. According to the model in section 3.2.2, the hydraulic resistance R_{HY} decreases with increasing depth while the standard flushing resistance R_{ST} increases with increasing

depth. The standard method follows a 3rd power trend while the two-step hydraulic flushing method follows a linear trend for both steps.

3.2.4 Discussion

Debris accumulation is a problem not only for high fill factor patterns, but also for enclosed patterns with smaller fill factors. A hydraulic flushing method utilizing self generated bubbles for debris entrainment was investigated. A rough hydraulic resistance estimate obtained using a static uniaxial model predicted a 53x reduction with the new method. Significant improvements in surface and edge finish as well as machining time and depth were observed. The technique does require a pattern that allows through-holes to be machined first and also therefore a tool height exceeding the thickness of the workpiece. More die area is required, but if the location of the through-holes is kept constant, the through-hole pattern dies could be reused many times. The reduced edge wear also extends the lifetime of the finishing tools.

CHAPTER 4

WIRELESS RF SENSING OF DISCHARGES IN μEDM

Wireless signals are inherently generated with each discharge in micro-electro-discharge machining (μEDM), providing an opportunity to directly monitor discharge quality. Unlike traditional methods of monitoring progress in machining, which rely on electrical characteristics at the discharge supply terminals, this method is less affected by parasitics. The depth location of a metal-metal interface can be distinguished in the wireless signal. This is useful for determining the stop depth in certain processes. As debris accumulate in the discharge gaps, shifts in the wireless spectra can also indicate spurious discharges that could damage workpiece and tool.

Section 4.1 motivates the use of wireless signals for monitoring machining performance. Section 4.2 presents experiments on sensing the interface between two metals. Section 4.3 investigates the use of wireless signals for monitoring debris accumulation and the chapter is wrapped up with conclusions in section 4.4.

4.1 Wireless Discharge Sensing Background

A common challenge in μEDM (and other micromachining technologies) is determining how deep to advance the tool in order to achieve the desired depth. For example, to machine through the full thickness of a workpiece, it is necessary to account for the tool wear and tool rounding effects during machining [El-Ho05]. Since tool wear

varies with workpiece material as well as from pattern to pattern, a certain amount of characterization may be required [Bro98]. This is especially true for high density batch mode μEDM where debris accumulation can cause spurious discharges.

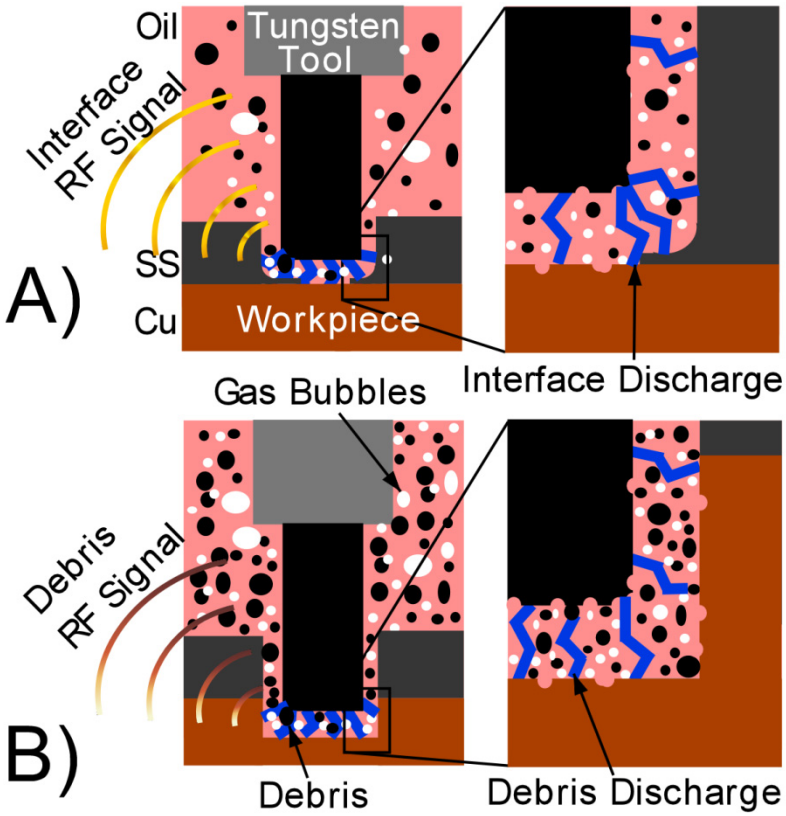

Fig. 4-1: (A) A 300 μm diameter tungsten tool produces different wireless signals at the interface of stainless steel and copper. (B) Signal from debris discharges also differs. Blue: Electrodischarges Black: debris, White: Bubbles

During the machining process, there are many cases in which the device layer is backed by another conductive layer. A thin device layer may need to be bonded to a handle wafer to prevent deformation. For very small dimensions, traditional solutions such as adding stabilizing tabs to the design are not practical. A better solution is to back the device layer with a layer of electroplated metal to form a restraining layer. Alternatively, if the pattern is not released during machining, the device layer could

simply be physically secured to a dummy metal layer. A backing layer prevents excessive widening at the exit hole as well as machining into the stage. For precision machining, real-time information about when the cutting tool reaches the interface of metals would prevent unnecessary damage (Fig. 4-1) to the tool and workpiece as well as reduce machining and characterization time.

The SEM images in Fig. 4-2 are an example of this problem. The pattern comes from a high density antenna stent in [Tak05]. The copper tool on top has very close, high density features which cause debris accumulation but spurious discharges cause a different failure mode in this machining. The problem is that when the workpiece has been fully machined in any particular area, the recast on the surfaces is uneven and there is a stress distribution that is relieved through bending. The bending of the beam in the corner is compounded as more areas are released and eventually bends so much that it contacts the tool, perpetually short circuiting. Another consideration is that discharge energy and bubble generation are greater as the tool punches through to the bottom of the workpiece due to concentrated discharges at the edges. The machining cannot be continued without destroying this bent part and so must be stopped, leaving almost the entire pattern unfinished. Characterizing the stress that causes this bending is the topic of chapter 5.

A solution to the problem is shown in Fig. 4-3. The 25 μm thick stainless steel device layer in was initially backed by 30 μm of electroplated copper for rigid support during machining. The same antenna stent pattern from Fig. 4-2 was batch machined with a silicon sidewall passivated tool until there was too much debris accumulation stuck in the tool to continue. The copper was subsequently etched with nitric acid, releasing the

stainless steel structure. Without the copper support layer, the device layer would have been free to move like before. (Of course, this also occurs if machining continues through the entire thickness of a copper backing layer.)

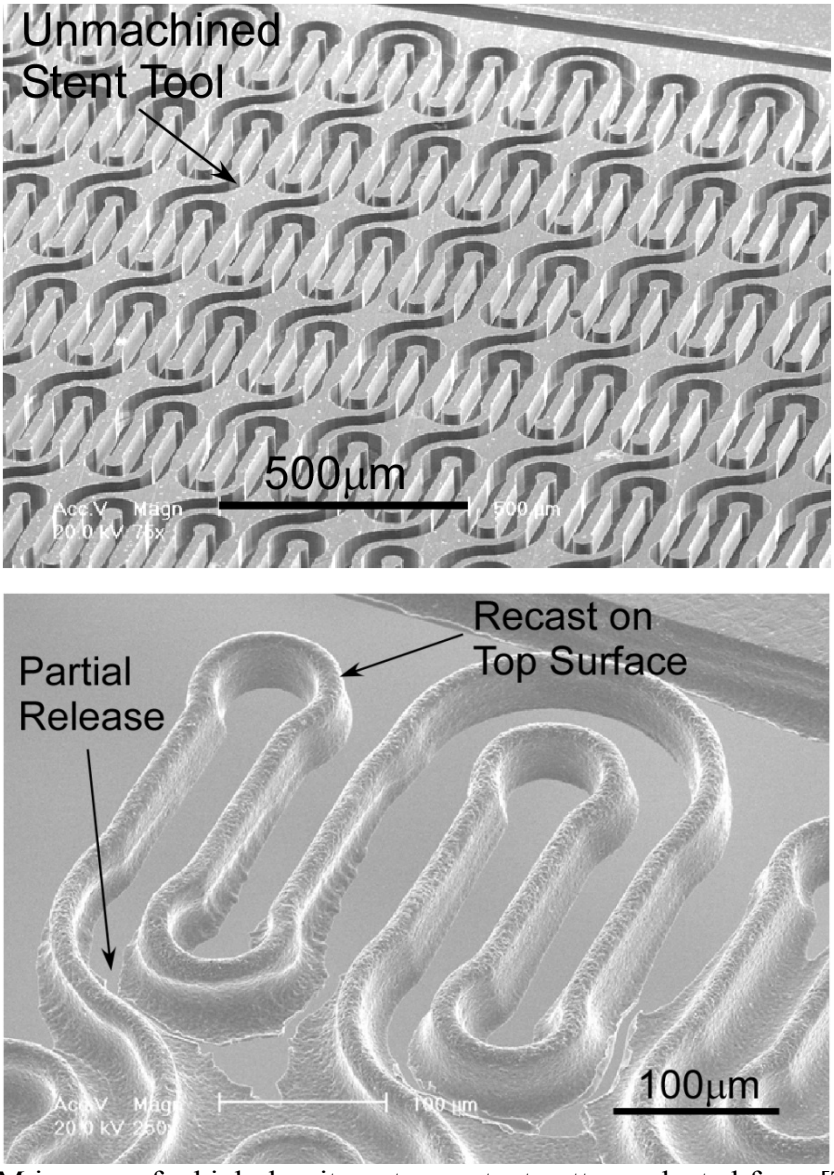

Fig. 4-2: SEM images of a high density antenna stent pattern adapted from [Tak05]. The top pattern is the copper tool and the bottom is the corner of the stainless steel workpiece. The machining stalls when the beam is released, bends to relieve stress and short circuits to the tool.

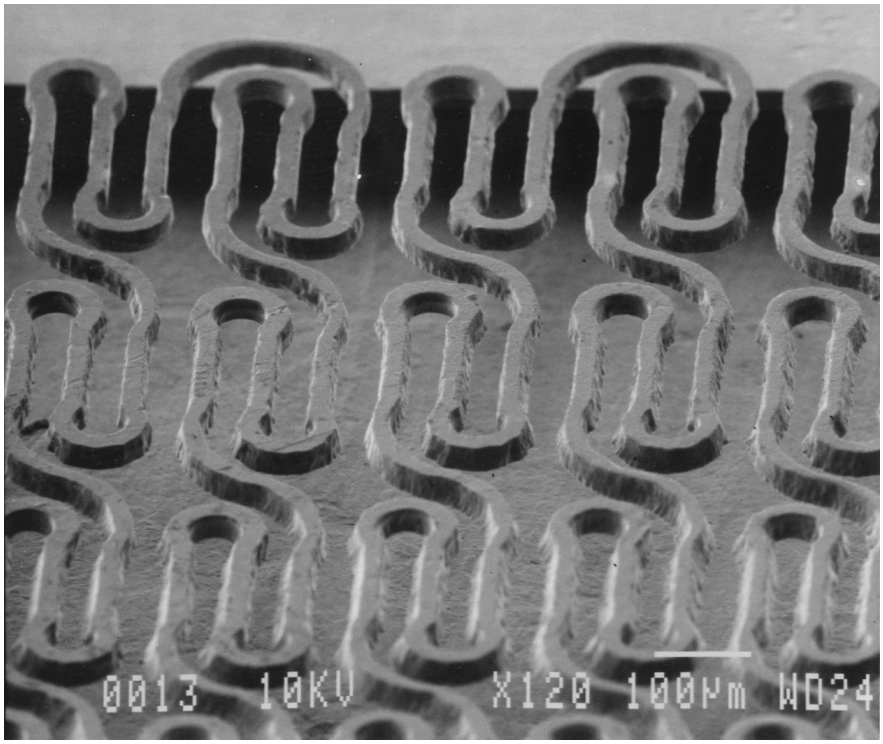

Fig. 4-3: Example of antenna stent pattern for batch µEDM. The 25 µm stainless steel foil is electroplated with thick (~30 µm) copper to prevent movement during machining. It is then released with nitric acid.

The equivalent of a silicon electro-chemical etch-stop signal for µEDM would be useful for determining the actual machined depth, irrespective of tool wear [Klo89]. Automated detection would reduce the need for detailed characterization when machining a new pattern, changing individual machining steps within a multi-step process, and accounting for wear rate after multiple uses of the same tool.

4.1.1 Discharge Monitoring

Discharge quality monitoring techniques for EDM typically use analysis of voltage and current waveforms on the workpiece (anode) and tool (cathode) side [Cab08, Liu97]. Since the discharge process is stochastic, the shape of these waveforms can vary widely

from discharge to discharge, making it difficult to reliably derive information from them. As will be shown later, the variability increases if effects like debris accumulation occur. These methods generally categorize the waveforms into spark discharge, arc dicharge, open circuit, or short circuit. Some also track discharge frequency. Recently, fuzzy analysis and neural network process control methods have been applied to macro-scale EDM [Cab08, Kao08, Lia08]. These methods require their own sample size and window calibration in order to filter out noise from the desired trends.

In this chapter we explore using wireless signals inherently generated by μEDM discharges to monitor the machining process. Specifically, we investigate a) the detection of an interface of two metals (Fig. 4-1A) and b) discharge quality when debris accumulation occurs during deep machining or in enclosed patterns (Fig. 4-1B). A view toward monitoring large-scale production by μEDM is considered.

4.1.2 Wireless Monitoring

Attaching a dipole antenna to a spectrum analyzer enables direct measurement of discharge behavior unaffected by terminal parasitics. The addition of a voltage/current probe to the terminals could in-itself potentially influence the accuracy of the measurements. Micro-EDM discharges with very low energy cause less residual damage to the finished workpiece surface, enabling smaller features and finer tolerances. Minimizing parasitics can be valuable in controlling discharge energy [Mas90] and part of this consideration is minimizing the parasitic load due to an observation probe at the discharge terminals.

Wireless signals generated from fast current spikes have been studied in the past [Ishi96, Kad91,Tom99]. Marconi utilized spark discharges similar to those found in EDM for wireless communication in the 1890s. It has also been shown that the noise waveform of discharges between switch contacts is influenced by the choice of material [Eba99] and electrode area [Eba00]. In the late 1970s, early work showed that it was possible to use RF transmissions to distinguish between open circuit, spark, arc, and short circuit conditions in macro-scale, serial mode EDM [Bhat78, Bhat80]. At the micro scale, particularly for batch mode, process monitoring is even more critical. Due to the smaller dimensions, tighter tolerances, and electrode multiplicity, the role of debris accumulation and gas evolution can have a much larger impact on discharge quality, which may appear in the wireless spectra. The role of tool wear on depth accuracy is also much more pronounced.

In the following sections, experimental results for wireless sensing of metal-metal interfaces and debris accumulation during μEDM are presented.

4.2 Metal Interface Sensing

The detection of a metal-metal interface during machining would be beneficial for machining a device layer that is backed by a metal restraining layer. Tool wear, characterization time, and total machining time would all be improved. In batch μEDM, this interface is obscured from visual inspection since the tool remains stationary and is larger than a serial mode tool. Wireless detection of μEDM discharges is attractive because the measurement is less affected by terminal parasitics and also has less effect on terminal parasitics.

The wireless RF discharge spectra at the interface between #304 stainless steel and copper was investigated during machining with a Panasonic© ED-72 μEDM. Approximately 60 μm of copper was electroplated on the backside of 100 μm stainless steel foil and repeatedly machined on the steel side with a 300 μm diameter circular tungsten tool at different discharge energies. Machining parameters are listed in Table 4.1. The presented data is for 80 V and 100 pF, but the other configurations gave similar results. Vertical stage vibration (~10 μm) was used for debris flushing, which was not allowed to accumulate significantly.

Table 4.1: Wireless Sensing Machining Conditions

Tool Diameter	300 μm
Voltage	70, 80, 110 V
Capacitor	100 pF, 3.3 nF
Resistor	1 kΩ
Z-Feed	0.2, 0.3 μm/s

The experiment setup is shown in Fig. 4-4. An Agilent ESA4405B spectrum analyzer with a dipole antenna was used to periodically monitor the wireless spectrum of the discharges at a distance of 40 cm from the machining area. Measurements covered a bandwidth from 9 kHz to 1 GHz with 10 kHz resolution and 5 dB attenuation. Since there are thousands of discharges per second, varying amounts of debris and gas bubbles, the spectra have some random variation. The max-hold setting was used over 30 sec. intervals, selecting the maximum value from ~232 samples per data point. Tool plunge depth information was recorded from the μEDM controller at the same time spectra data points were recorded.

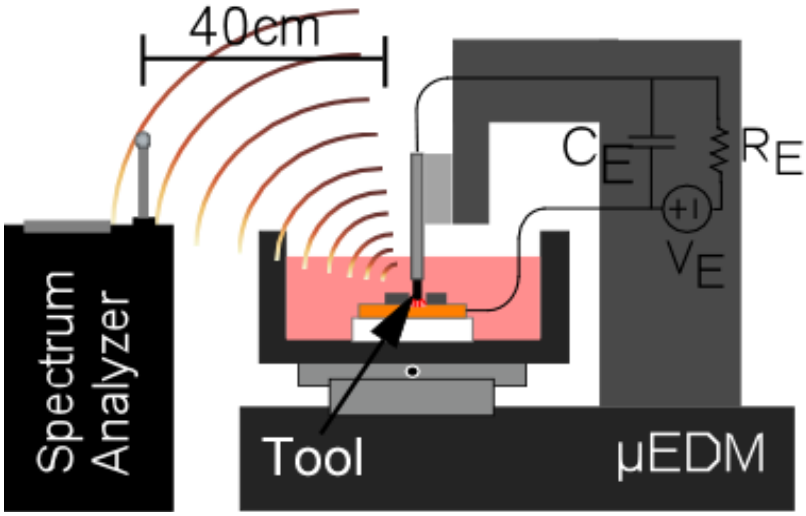

Fig. 4-4: Experiment setup for wireless monitoring (tool on top)

4.2.1 Results

The plot of tool plunge depth vs. time in Fig. 4-5 does not readily indicate the interface depth, which is often difficult to judge blindly for deep machining. This is because tool plunge depth is affected by tool wear and does not always represent the true machined depth. Since the machining is relatively shallow and the pattern is simple in this experiment, there should be little tool wear except for edge rounding. The spectrogram for the stainless steel/copper interface in Figs. 4-6 shows a 10 dBm disturbance at around 100 μm in the 300-350 MHz band and a 5 dBm average change across the entire 1 GHz bandwidth. The transition region indicates when the interface is completely past. Tool rounding at the edges requires machining deeper than the interface to remove burrs at the bottom of the workpiece (Fig. 4-1). This effect is a simple amplitude shift that occurs across almost the entire bandwidth. The tool plunge rate plot indicates that the machining was smooth through the entire thickness of the experiment. If there were debris effects, there would have been a noticeable decrease in plunge rate.

The shift in amplitude across the band therefore must have been caused by the interface of materials.

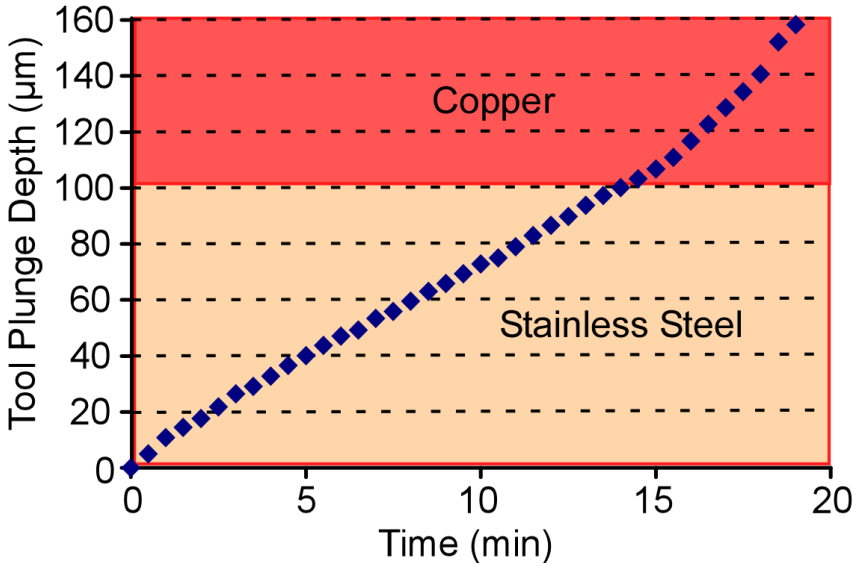

Fig. 4-5: Traditional way for monitoring machining progress. Tool plunge depth vs. time does not unambiguously indicate the location of the interface between steel and copper.

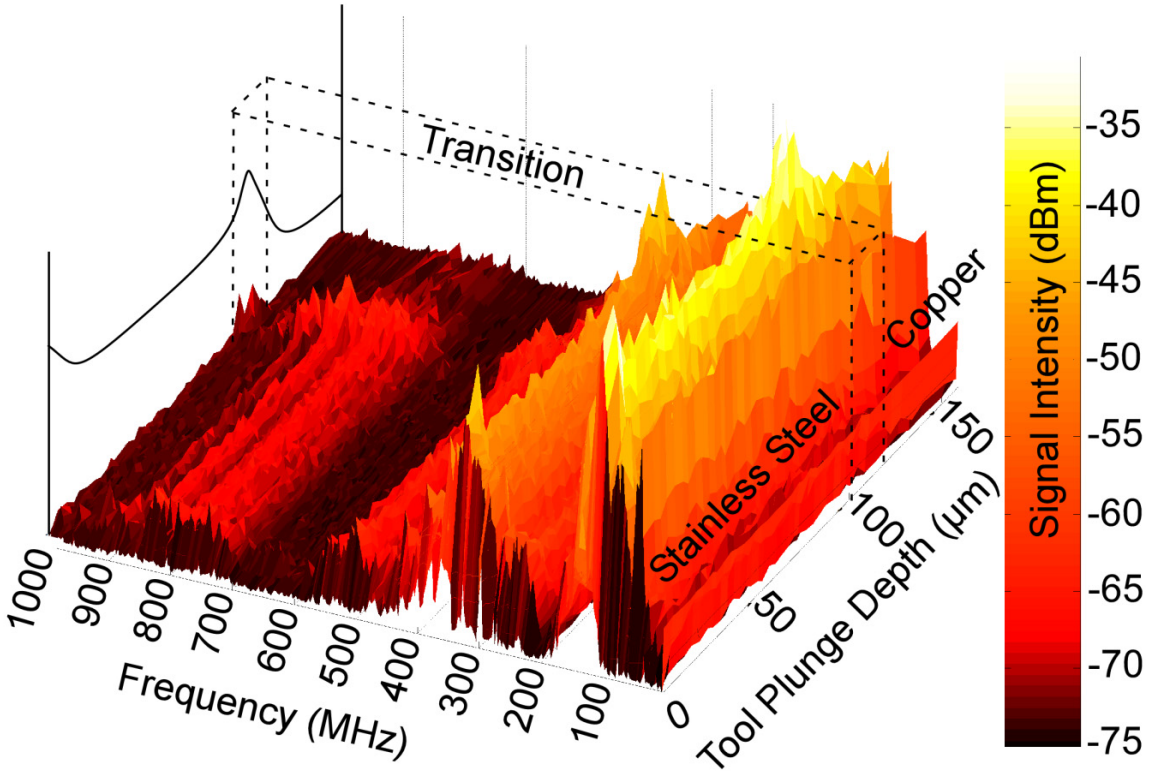

Fig. 4-6: 3D plot of received wireless RF signal intensity from machining 100 µm thick stainless steel with electroplated copper on the backside shows a disturbance across the entire bandwidth at the interface depth.

In order to further investigate the stainless steel/copper interface, SEM images were taken shortly after the transition of one of the runs. As can be seen in Fig. 4-7, the steel is machined through the entire thickness and the copper has signs of discharges. There is a slight separation between the copper and steel around the edges. The SEM image in Fig. 4-8 shows an opening in the steel device layer just after the machining has penetrated to the copper backing layer. This technique enables blind monitoring of actual machined depth, reducing the time required for process characterization of complex patterns.

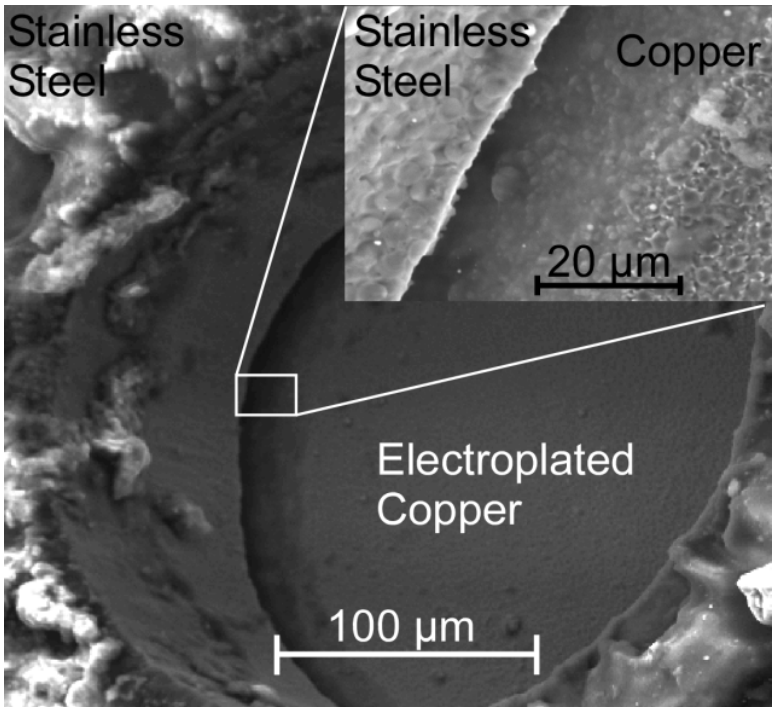

Fig. 4-7: SEM images of stainless steel/copper interface. Machining was stopped before the full thickness of copper.

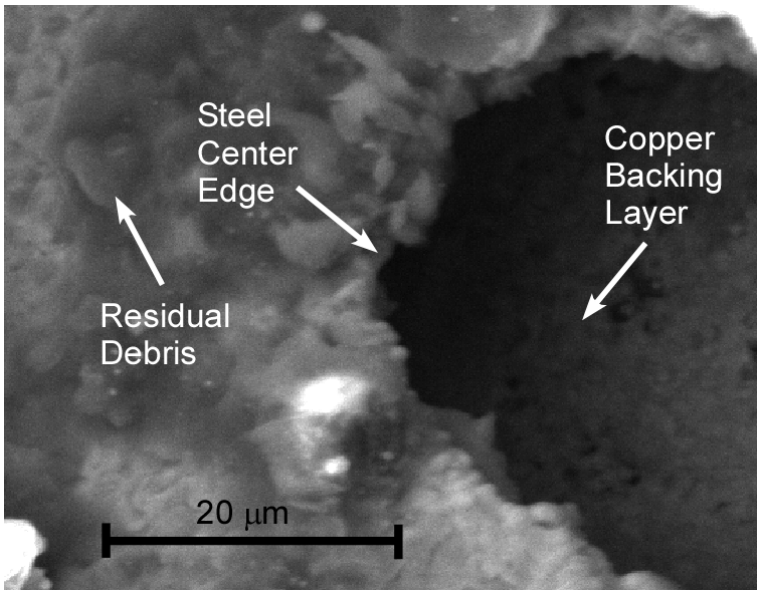

Fig. 4-8: Image of steel opening at the center of machining area just after penetration to the copper backing layer. The exposed steel edge concentrates the electric field and attracts discharges, widening the opening until it reaches the full diameter.

4.2.2 Discussion and Simulations

By the time the tool machines through first layer of metal the edges are rounded through normal tool wear [Kur08]. The rounded shape is transferred to the workpiece and so 'punches through' at the center of the metal before the outer edges as diagramed in Fig. 4-9. The discontinuity between the metals forms an edge that concentrates the electric field. Discharges will preferentially occur at the edges of the opening and with higher current until it has reached the full diameter of the tool plus the discharge gap. Since the wireless measurements use the max-hold function or a 232 sample window, these discharges are captured and dominate the spectrum. If an averaged signal were to be used, these spectra would not stand out as readily since normal discharges still occur.

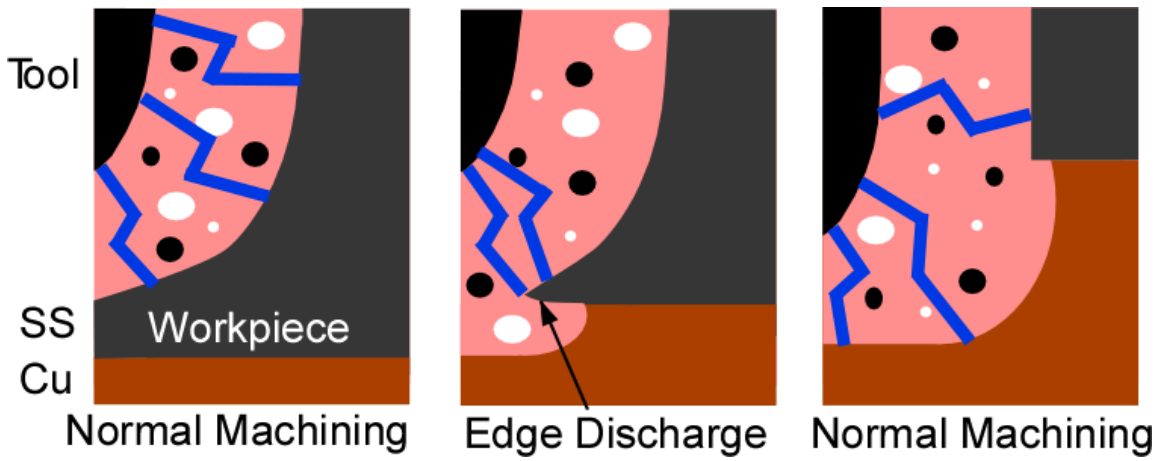

Fig. 4-9: Hypothesis of machining progression at the interface of two metals. Normal machining leads to wear that rounds out the tool. Then the first layer is punched through in the middle and discharges concentrate at the edges. Finally, the edge is levels out and normal machining resumes.

Electric field simulations in Fig. 4-10 were done using Comsol Multiphysics at four stages of the machining. In part A the tool is rounded (70 µm radius [Kur08]) from machining the steel and approaches the copper interface. To start, an even 5 µm gap gives a uniform electric field between the tool and workpiece. When the tool is advanced in part B the gap is smaller at the end of the tool (2.5 µm) and consequently has double the electric field (400 V/m instead of 200 V/m). This is the normal machining operation and demonstrates why discharges are focused at the tip of the tool. As each new layer of material is removed, the controller advances the tool to maintain the difference in electric field. Debris accumulation in the discharge gap can change this condition along the sides.

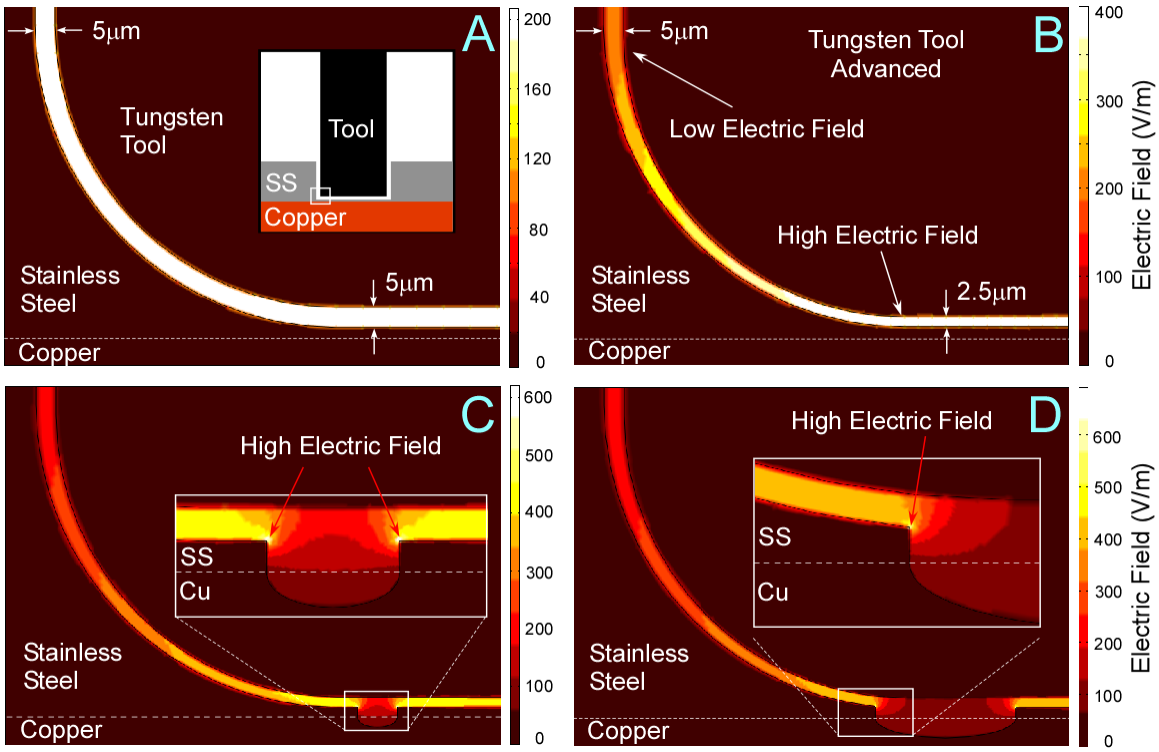

Fig. 4-10: Electric field simulation A: with 5 µm separation between workpiece and tool B: after advancing tool to 2.5µm separation electric field is much higher at bottom of tool C: higher field at opening of stainless steel D: opening widens to full tool diameter.

Once the steel is penetrated in a small area shown in part C (by removing a section of the simulation modeldd), the new edge has a much higher (600+ V/m instead of 400 V/m) electric field than just a flat surface. This also occurs to a small degree when pits are formed during normal machining, but the effect is much larger at the interface. The discharge gap changes based on the geometry of the hole at the interface.

The higher electric field lowers the breakdown voltage, increasing the current in each discharge which translates to the wireless signal. As machining continues in part D, the hole becomes wider and wider with the same high electric field at the edge. Once the edge is gone, machining returns to the normal electric field strength.

This effect can be confirmed by observing the machining of a slot in serial mode µEDM. During slot machining, the workpiece stage is dithered along one axis while the

tool remains stationary, allowing observation of the machined area with each pass. When the tool has some wear at the edges, it penetrates through the center of the workpiece first and the discharges visibly concentrate at the newly formed edges. The opening then becomes larger and larger until it is the same diameter as the tool plus the discharge gap. The higher energy edge discharges are audibly louder than normal discharges at high (110V) voltages. A similar effect recorded in terminal probe traces was also independently reported in [Kao07].

The elevated electric field from the edge of the steel opening shown in 4-10 can explain the higher amplitude in the wireless signature. The advantage of this approach for interface detection is that an amplitude disturbance across the entire wireless spectra is a simple signal to detect even with significant variation from discharge to discharge. While this signal should also be visible in terminal probe measurements, wireless detection has inherent benefits. Wireless detection has potential to enable monitoring of multiple machines in parallel while decoupled from the discharge process.

The underlying assumption of this technique is that tool edges will become rounded by the time the metal interface is reached, creating a transition region until the maximum diameter is reached as shown in Fig. 4-11. After the bottom surface of the stainless steel is penetrated, a small circumference edge is opened up which has a much stronger electric field than the rest of the surfaces that forms stronger discharges and therefore a higher amplitude wireless signal. As the hole expands, there are many more edges discharges and the wireless signal amplitude increases. Eventually, the edge reaches its maximum perimeter and starts to decrease and the wireless signal follows, lowering in amplitude.

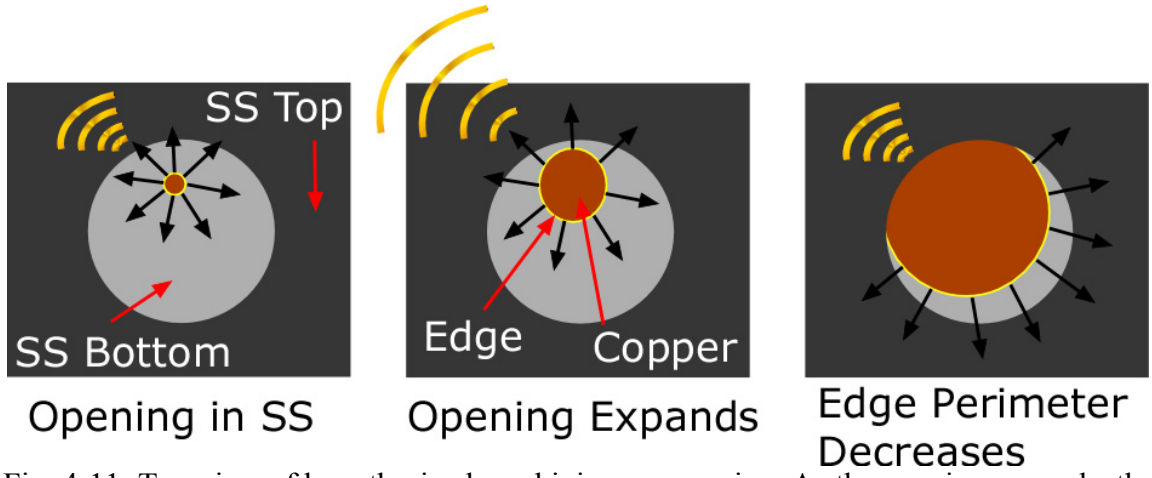

Fig. 4-11: Top view of hypothesized machining progression. As the opening expands, the wireless signal amplitude increases. As the edge perimeter decreases, normal discharges return and the wireless signal amplitude declines.

The edge discharge effect occurs when a tool penetrates through the bottom surface of a workpiece, even if there is nothing underneath or if the workpiece is simply stacked on top of another piece of metal. The higher electric field can also be used to fabricate a negative taper at the end of a deep micro-hole [Kao07].

4.3 Sensing Debris Dominated Machining

Debris accumulation can severely degrade machining performance for high density patterns, enclosed patterns, or deep machining. Debris is created naturally during the discharge process but problems occur when it is not flushed out of the discharge gap efficiently. In batch mode μEDM this is very problematic because the path for debris to escape can be quite long and becomes worse as feature density is scaled up. Discharge gap, tool wear, and machined workpiece dimensions are all degraded when there is debris accumulation.

Various methods of debris flushing have been attempted in the past. In serial mode, rotation and direct oil flushing are the traditional techniques and are effective for most

features. High aspect ratio machining and batch mode operation are more difficult to flush. In the last 15 years, vertical stage vibration from Hz to MHz frequencies has been developed and is the best option for batch mode flushing. Orbital (vertical + lateral) stage movement has also been used but increases minimum spacing between features.

Monitoring debris accumulation visually in batch mode is not possible because the tool obscures the view of the discharge gap. To investigate whether performance degradation from debris could be monitored wirelessly, a series of experiments were conducted by machining deep into thick copper at various discharge energies while recording the wireless spectra. The tool was 300 μm diameter circular tungsten and the stage was dithered vertically by ~10 μm to provide flushing. For comparison purposes, voltage and current terminal probes were monitored concurrently (Fig. 4-12) along with tool plunge depth (Figs. 4-13, 4-15). The data presented here contrasts runs with low energy (80 V, 100 pF) and high energy (110 V, 3.3 nF) micro-discharges.

Debris was allowed to accumulate on the surface of the workpiece without flushing it away. Thick pieces of copper surrounded the tool and machining site to set a finite volume of oil available to flush the discharge gap. Eventually, the volume was saturated with debris. This simulates situations where debris is trapped within the discharge gap due to dense or enclosed patterns or deep machining. The Panasonic™ MG-ED72W μEDM controller detects debris accumulation as a short circuit and retracts the tool well past the point that the short is removed. It then progresses again until another short circuit is encountered, repeating the process. This routine allows machining to progress at a lower plunge rate but does not eliminate the underlying cause of debris accumulation.

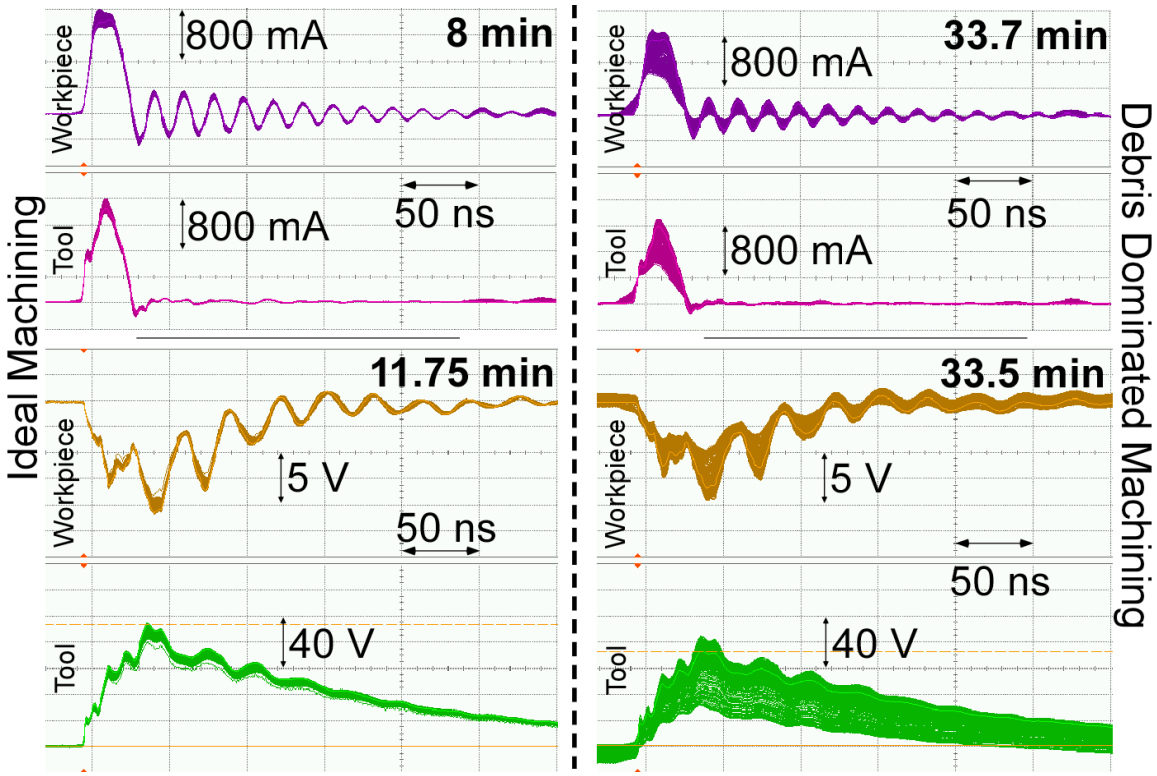

Fig. 4-12: Current (top) and Voltage (bottom) traces for a tool cathode and workpiece anode during (Left) ideal machining and (Right) debris dominated machining.

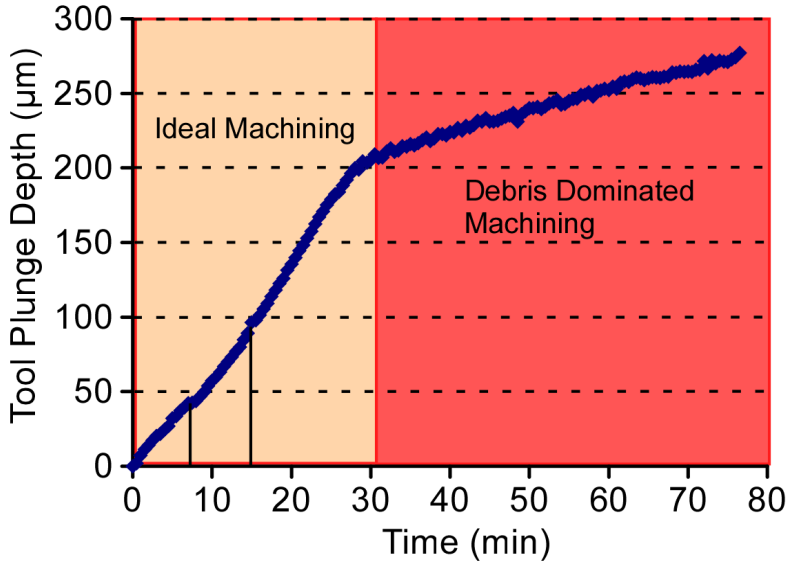

Fig. 4-13: Tool plunge depth vs. time shows debris effects on machining at 30 min.

4.3.1 Results

For low energy discharges there was a significant decrease in plunge rate at around 30 min that indicates debris dominated machining (Fig. 4-13). This is a typical sequence of events for normal batch mode µEDM. The current and voltage traces in Fig. 4-12 show discharges before and after this decrease. Each trace is the average of 16 samples but in this plot, multiple traces are shown by using the persistence mode for approximately 30 second intervals. The traces for debris dominated machining show significant instability compared to ideal machining, even with averaging. These are the spurious discharge documented in the earlier chapters.

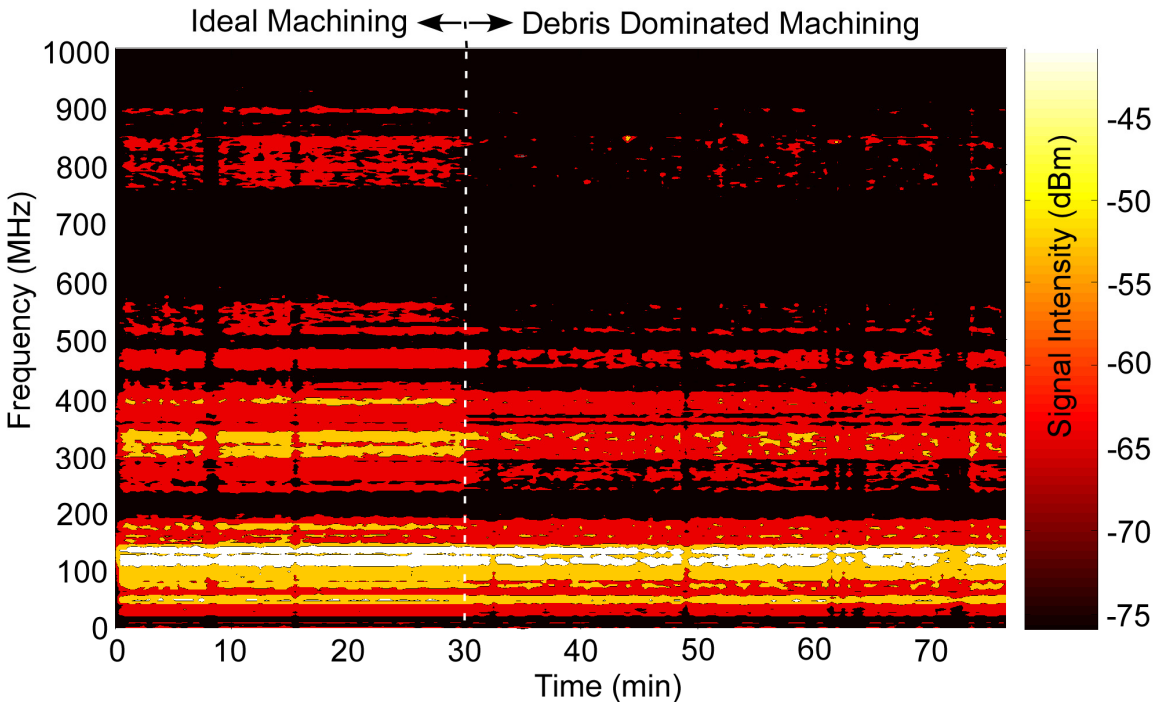

Fig. 4-14: Received RF with a Cu sample and 300µm W tool machining with 80V and 100pF. At 30 min a significant signal drop (7.4 dBm max) is detected, indicating debris dominated machining.

The spectrogram in Fig. 4-14 confirms that there is a significant disturbance in the wireless spectra at the same time. For example, the 800-850 MHz band dropped 4 dBm in signal strength when machining became debris dominated. There was a 2.2 dBm average drop across the full 1 GHz bandwidth. There were also several smaller changes in plunge rate that appear in the spectra.

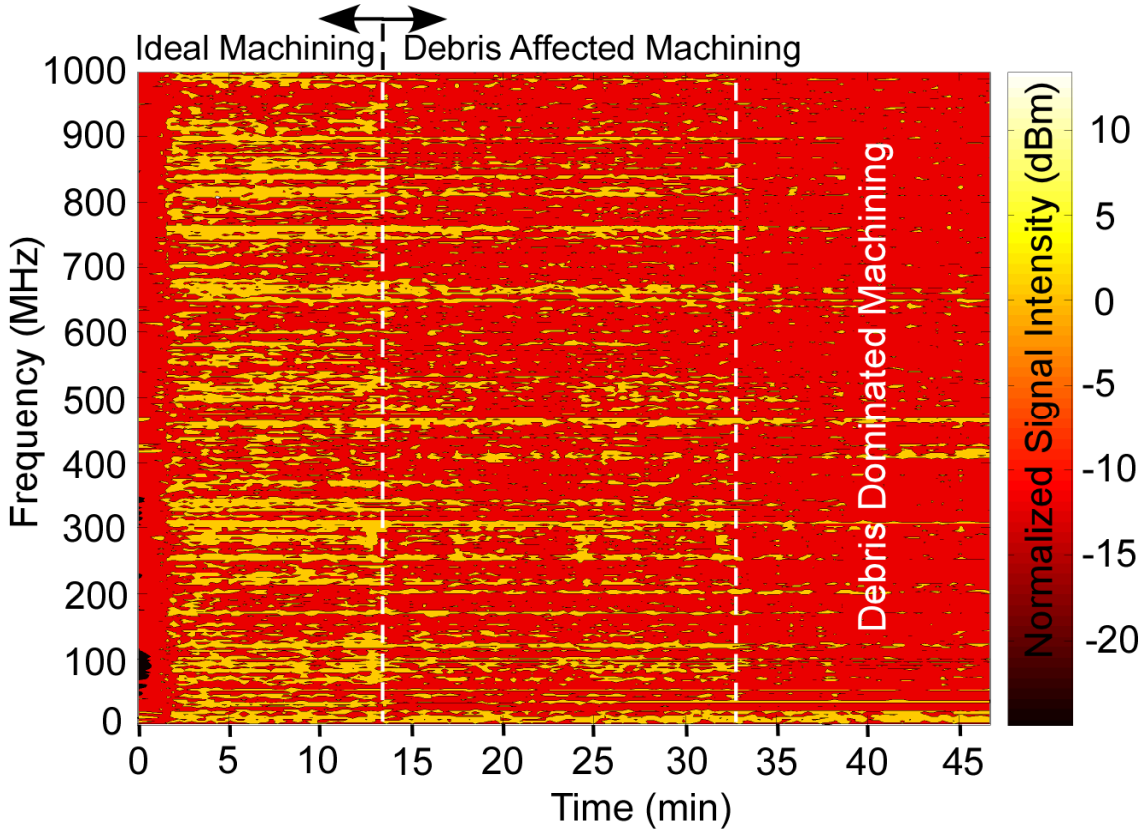

Fig. 4-15: Received RF signal of high energy discharges normalized to initial intensity. At 14 min and 33 min. there are significant signal drops indicating debris dominated machining.

The spectrogram data in Fig. 4-15 for high energy discharges was normalized to the first few spectra to show an alternative form of the data. There was a sharp drop in signal intensity around 14 min across almost the whole bandwidth. This was not visible in the tool plunge rate plot of Fig. 4-16. At around 33 min the plunge rate decreased which

was also recorded in the spectra. This indicates that for higher energy discharges, there can be changes visible in the wireless spectra before short circuits are detected that slow the plunge rate.

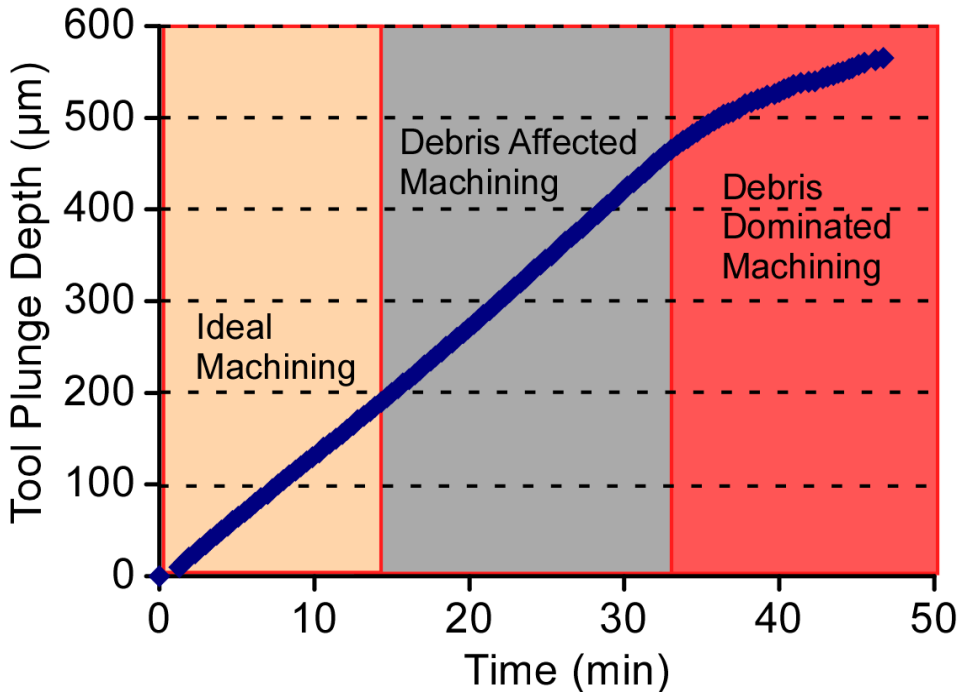

Fig. 4-16: Tool plunge depth vs. time shows debris effects on machining only at 33 min. This is later than 14 min in Fig. 14.

4.3.2 Discussion

The detection of debris accumulation is essential to high quality machining in batch mode µEDM. One effort used a pulse discrimination algorithm to determine the percentage of complex (spurious) discharges over the course of machining [Lia08]. The resulting information has the same pattern as the amplitude of the spectrogram in Fig. 4-15. While direct waveform measurement has been used to detect the various discharge states, it is also subject to changing parasitics from different patterns, materials, etc. For very low discharge energies, wireless sensing could provide an advantage.

Wireless measurement directly measures the discharge. Changes in the wireless spectra may provide an early warning before debris dominated machining occurs. Dynamically adjusting machining parameters and flushing based on this feedback could then potentially improve machining efficiency and prevent workpiece and tool damage.

The formulation of a model for the discharge process and for the wireless spectrum of fast moving current pulses such as those present in EDM are the subjects of constant experimentation and research [Dha05, Fuj03, Grea98, Kang98, Nai99, Sha97, Take96, Wil91]. A working model would enable reconstruction of the current pulse that the discharge consisted of without the influence of a physical probe. The instability of the current pulses at the terminals in Fig. 4-12 is certainly related to the wireless signature, but the transformation between the two is still under investigation. The changes in current and voltage discharge shape could possibly be affected by a shift in breakdown voltage, pulse resistance R_p and pulse inductance L_p for the approach described in Figs. 1-2, 3-2 and 4-17. Further investigation is needed to determine if additional modeling parameters are needed. It would also be useful to know what impact the differences in the terminal probe measurements on the workpiece and tool side have on the wireless signal and therefore the discharge itself. Understanding these relationships would provide a more detailed interpretation of the received data.

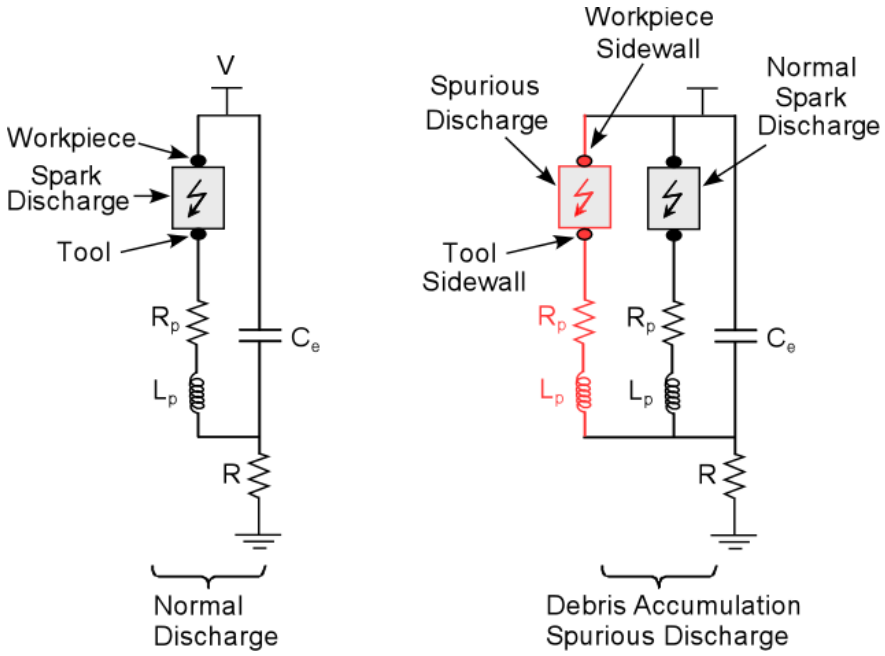

Fig. 4-17: Model for normal and debris accumulation spark discharges. Changes in the breakdown voltage, R_p and L_p could have an impact on the current pulse shape and in turn, the generated wireless signal.

In recent work from our group, wireless monitoring with spark discharges has been used in microfabricated Geiger radiation detectors [Eun08]. Tuning the discharge characteristics would allow a network of ultra wide band sensors. Wirelessly sensing of multiple circuits or a network of EDM machines in parallel could enable scaling up operations less expensively while improving machining quality.

4.4 Conclusions

Inherent wireless signal information from the discharges in μEDM can be very helpful in monitoring machining progress and discharge quality. The information gathered is directly related to the discharge and complements information from terminal probe measurements. The metal-metal interface transition between stainless steel and electroplated copper showed a 10 dBm shift in intensity for the 300-350 MHz band and a

5 dBm average change across the full 1 GHz bandwidth. This technique can be applied to separate, stacked metals as well. As debris accumulate in batch mode μEDM, the signal amplitude decreases across the spectrum. Experiments typically showed a 4 dBm drop in the 800-850 MHz band with a 2.2 dBm average drop across the full 1 GHz bandwidth. Wireless monitoring could potentially be used with μEDM control hardware to monitor multiple circuits or machines at once.

CHAPTER 5

STRESS AND RECOMPOSITION OF MICRO-EDM RECAST LAYERS IN BIOCOMPATIBLE 316L STAINLESS STEEL

Managing residual stress is one of the most pervasive challenges in MEMS fabrication. Significant effort has been put into the deposition of low stress films, particularly polysilicon, which enabled reliable surface micromachining. This chapter is the first study to explore residual tensile stress in 316L stainless steel after micro-electrodischarge machining (μEDM). This particular stainless steel is an important medical implant material due to its biocompatibility and corrosion resistance. It is used in most commercial cardiovascular stents.

Section 5.1 begins with some background on μEDM recast formation and stress measurement. The experiment methods are outlined in section 5.2 and the corresponding results are in section 5.3. Finally, section 5.4 contains analysis and discussion.

5.1 Background

Since μEDM is an electrothermal process, it has the capability to machine any conductive material, including bulk metals alloys like 316L stainless steel and hard materials like W-C-Co. However, after machining, a thin recast layer (sometimes called a white layer) of melted metal and debris remains on the surface of the workpiece with a small heat affected zone underneath that can impart stress on the finished features. When

machined structures are released, the stress differentials may be relieved through bending. If this bending occurs during machining, both the workpiece and the tool could be damaged. This is an important concern for small features (<30 μm) because even minor deformations can have a large impact on performance.

Past work has covered stress levels of this recast in macro-scale EDM at 5-10x higher currents, and micro-hardness of the heat affected zone in deep EDM holes [Tha08, Gha03]. The X-ray diffraction residual stress profile of the recast and heat affected zone for 316L stainless steel using 5 A, 5 μs, 46 V macro-EDM is shown in Fig. 5-1 [Gha03]. The recast layer is optically visible while the heat affected is not.

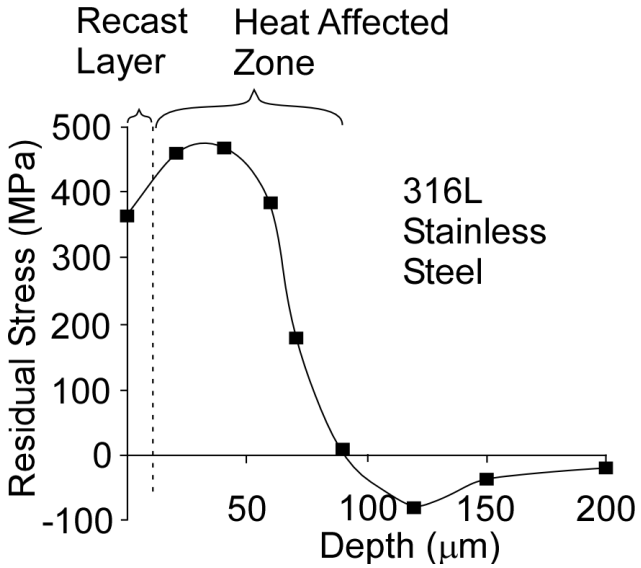

Fig. 5-1: Residual stress profile of stainless steel after macro-EDM. The recast layer is about 5-10 μm while the heat affected zone extends around 100 μm below the surface. Adapted from [Gha03].

This work examines the stress levels at discharge energies starting at the lowest levels of past studies (20 μJ) down to 1000x smaller (32 nJ). Once characterized, these residual

stresses could be avoided, compensated for, or exploited in the microfabrication of MEMS sensors and actuators.

There are several techniques for measuring residual stress in metals but options are limited when the desired resolution is less than 5 μm, as is common in many MEMS thin films [Prev08, Wit01]. The X-ray diffraction method measures the strain in the crystal structure to determine the stress at a 5 μm depth slice from the surface. A thin layer can be removed by electrochemical polishing to measure subsequent slices, but it destroys the sample [Ekme07]. This is appropriate when the recast layer is 10-20 μm for high energy EDM [Ekme07], or for measuring a heat affected zone. The recast is expected to be on the order of 1 μm for μEDM potentially with a small heat affected zone.

Another method is to use the Stoney equation to convert the geometry of a stressed, deflected cantilever beams of different thicknesses back to the residual stress of the recast and the beam [Ston09]. This is a common technique for measuring the stress in MEMS thin films which we will also use [Jan08]. It has also been used in conjunction with electrochemical polishing [Ekme06]. Since the recast layer is thin, for the purposes of this study, it is treated as a thin film at the surface of the bulk steel while recognizing there could be a heat affected zone underneath.

5.2 Experiment Definition

The process flow in Fig. 5-2 shows how cantilevers can be formed to characterize the residual tensile stress of the recast layer. A stress field is first machined in 50 μm-thick or 100 μm-thick 316L stainless steel foil from Goodfellow Corp. with a 300 μm diameter serial mode tungsten tool by rastering across a large area down to a target depth of 10 or

25 µm. Varying the voltage and capacitance controls the energy per discharge and affects the recast thickness, surface roughness, and residual stress level. Machining Conditions are listed in Table 5.1.

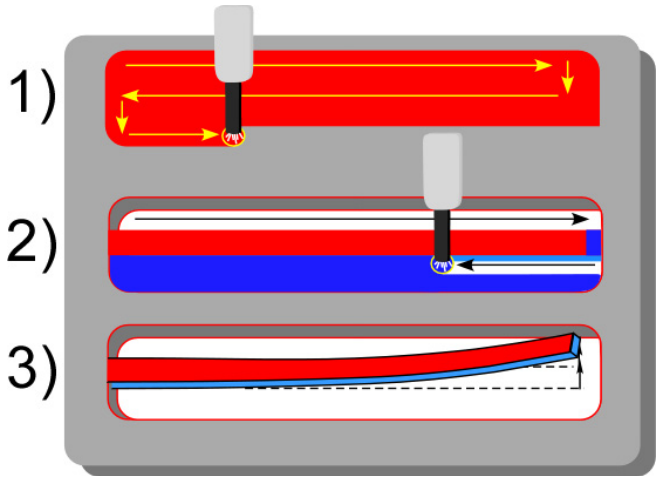

Fig. 5-2: Cantilever beams with varying amounts of stress are fabricated by 1) machining a stress field, 2) patterning the beam, and 3) releasing the end to allow the beam to bend. Stress is controlled by varying the discharge energy which changes the recast left after machining.

Table 5.1: Stress Study Machining Conditions

Voltage	80-110V
Capacitance	10-3300pF
Resistance	1 kΩ
Z Feed Rate	0.2 µm /s
Stress Field Depth	10,25 µm
Beam Cut Energy	90V 220pF
Workpiece Thickness	50, 100 µm
Tool Diameter	300 µm
Beam Length	4 mm

A cantilever is cut from each stress field with a consistent discharge energy for comparison between recast layers. The sides of the beam are cut first to prevent any vertical bending during machining. The workpiece is clamped to a piece of brass foil underneath. When the end of the beam is machined the beam deflects up. Debris is flushed away during machining. After machining, the workpieces are cleaned with

ultrasonic agitation in EDM oil, surfactant, acetone, IPA, and DI water. A separate set of 6 stress fields is machined to allow further investigation of the recast layer without destroying the cantilever beams.

Deflection, surface roughness, and machined depth of the stress field are recorded with an interferometer. Imaging and measurement of the beams and recast layers is done with an FEI Quanta 200 and Nova focused ion beam (FIB) instruments, scanning electron microscope (SEM), and EDX.

5.3 Results

5.3.1 Cantilever Beam Measurements

Sets of 4mm X 80μm cantilever beams were machined with 6 different recast layers each at 3 different final thicknesses, 40 μm, 75 μm and 90 μm. Tables 5.2-5.4 list the recorded dimensional data. The optical photos in Figs. 5-3 to 5-5 display the vertical deflections for each recast and thickness as measured on a Zygo NewView 5000 interferometer. Higher voltage and capacitance delivered higher energy discharges, which translated into rougher surfaces and larger residual stresses. The control beams, which had no recast layer on the top, did not deflect, proving the test structure is valid.

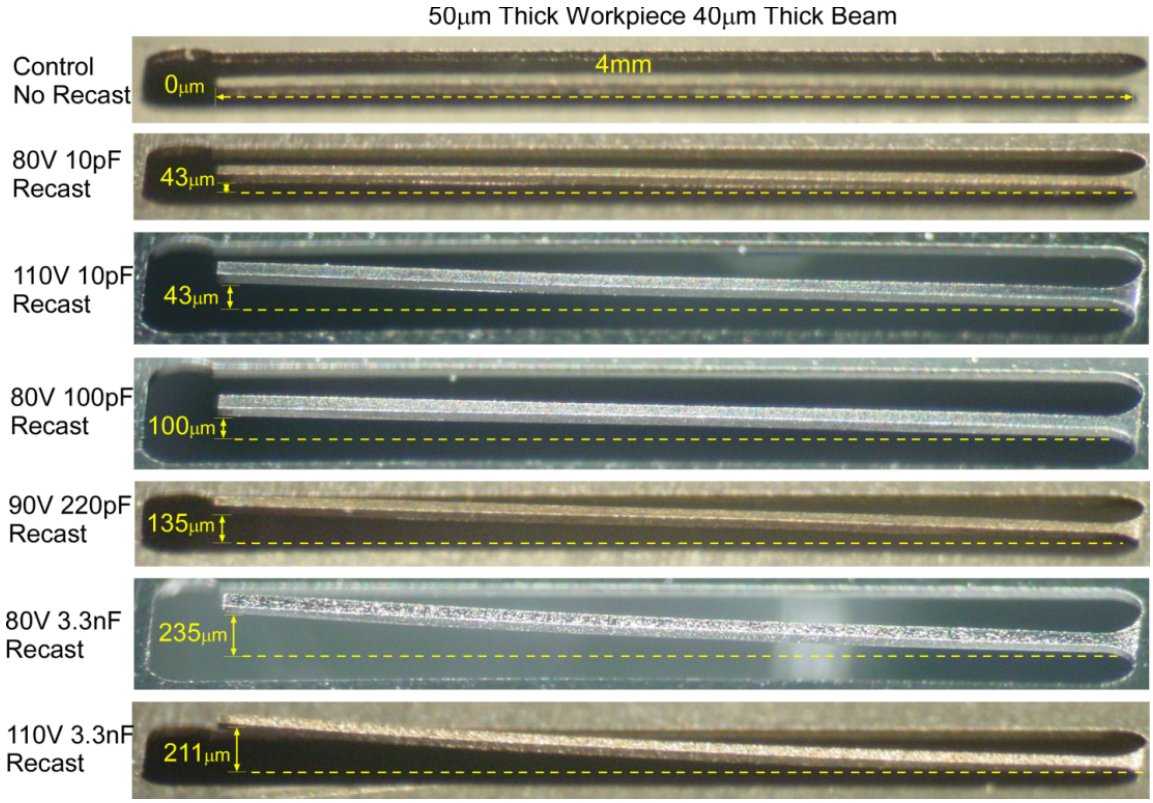

Fig. 5-3: Optical photos of 4mmX80μmX40μm cantilever beams under 7 different stress conditions. Deflection, average surface roughness, and machined depth were measured with a Zygo NewView 5000 interferometer.

Table 5.2: Cantilever parameters of 50 μm thick #316L

Recast Machining Parameters	Discharge Energy $E=CV^2/2$	Beam Width W	Beam Thickness H	Beam Deflection Δz
110V 3.3nF	20.0 μJ	83.0 μm	39.3 μm	**211 μm**
80V 3.3nF	10.6 μJ	80.1 μm	40.0 μm	**235 μm**
90V 220pF	0.90 μJ	83.1 μm	41.1 μm	**135 μm**
80V 100pF	0.32 μJ	80.8 μm	43.0 μm	**107 μm**
110V 10pF	0.061 μJ	83.4 μm	41.0 μm	**43 μm**
80V 10pF	0.032μJ	84.6 μm	43.7 μm	**43 μm**
Bare	0	77.7 μm	50.0 μm	**0**

Fig. 5-4: Optical photos of 4mmX80μmX75μm cantilever beams under 7 different stress conditions.

Table 5.3: Cantilever parameters of 75 μm thick #316L

Recast Machining Parameters	Discharge Energy $E=CV^2/2$	Beam Width W	Beam Thickness H	Beam Deflection Δz
110V 3.3nF	20.0 μJ	86.4 μm	75.0 μm	**141 μm**
80V 3.3nF	10.6 μJ	81.1 μm	73.0 μm	**145 μm**
90V 220pF	0.90 μJ	87.6 μm	80.0 μm	**93 μm**
80V 100pF	0.32 μJ	87.0 μm	79.0 μm	**102 μm**
110V 10pF	0.061 μJ	89.1 μm	81.0 μm	**79 μm**
80V 10pF	0.032μJ	90.1 μm	73.0 μm	**85 μm**
Bare	0	85.0 μm	100.0 μm	**0**

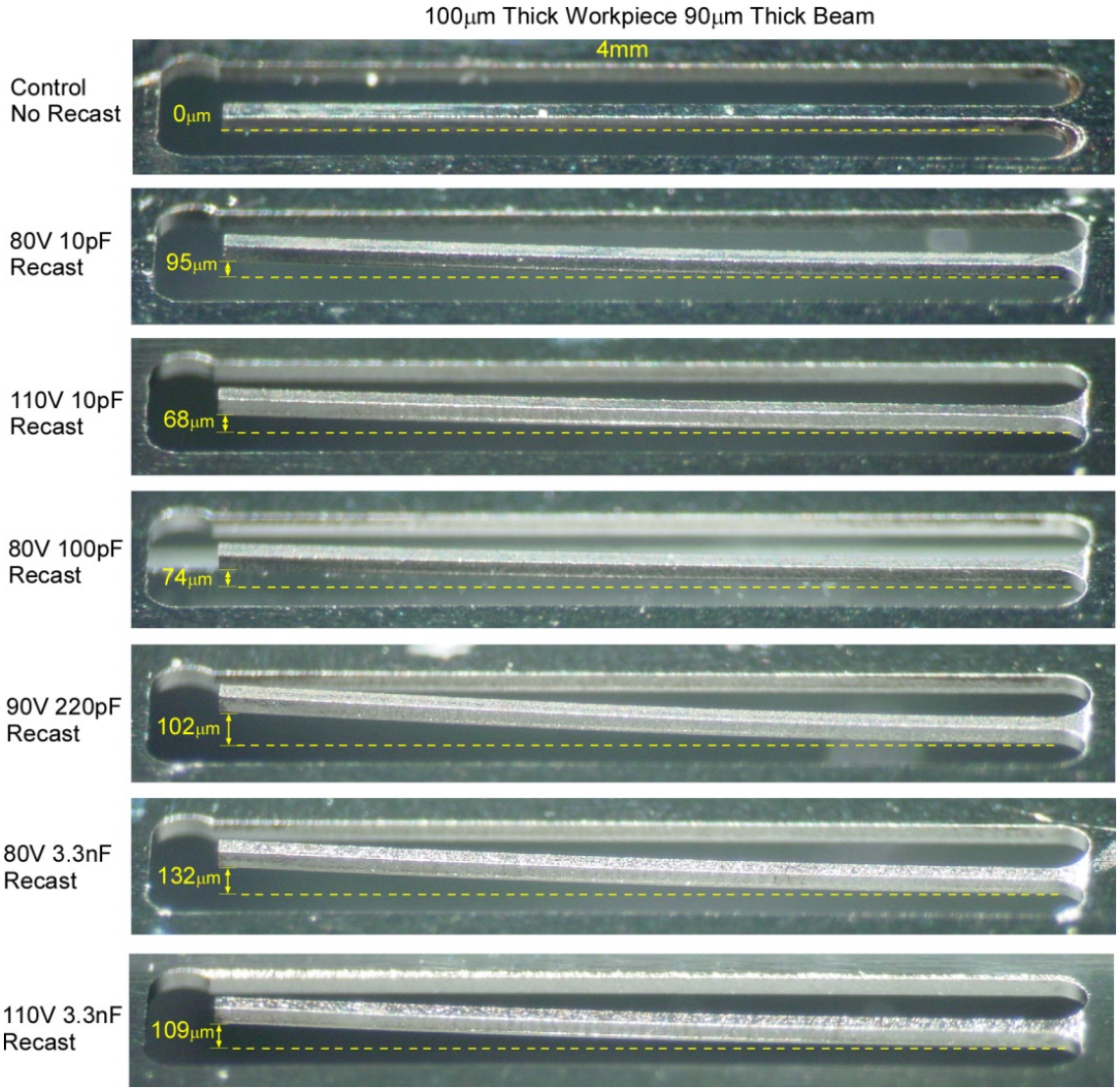

Fig. 5-5: Optical photos of 4mmX80μmX90μm cantilever beams under 7 different stress conditions.

Table 5.4: Cantilever parameters of 90 μm thick #316L beam

Recast Machining Parameters	Discharge Energy $E=CV^2/2$	Beam Width W	Beam Thickness H	Beam Deflection Δz
110V 3.3nF	20.0 μJ	84.0 μm	86.0 μm	**109 μm**
80V 3.3nF	10.6 μJ	85.2 μm	85.0 μm	**132 μm**
90V 220pF	0.90 μJ	82.9 μm	89.0 μm	**102 μm**
80V 100pF	0.32 μJ	82.1 μm	88.0 μm	**74 μm**
110V 10pF	0.061 μJ	78.7 μm	90.0 μm	**68 μm**
80V 10pF	0.032μJ	85.1 μm	85.0 μm	**95 μm**
Bare	0	85.0 μm	100.0 μm	**0**

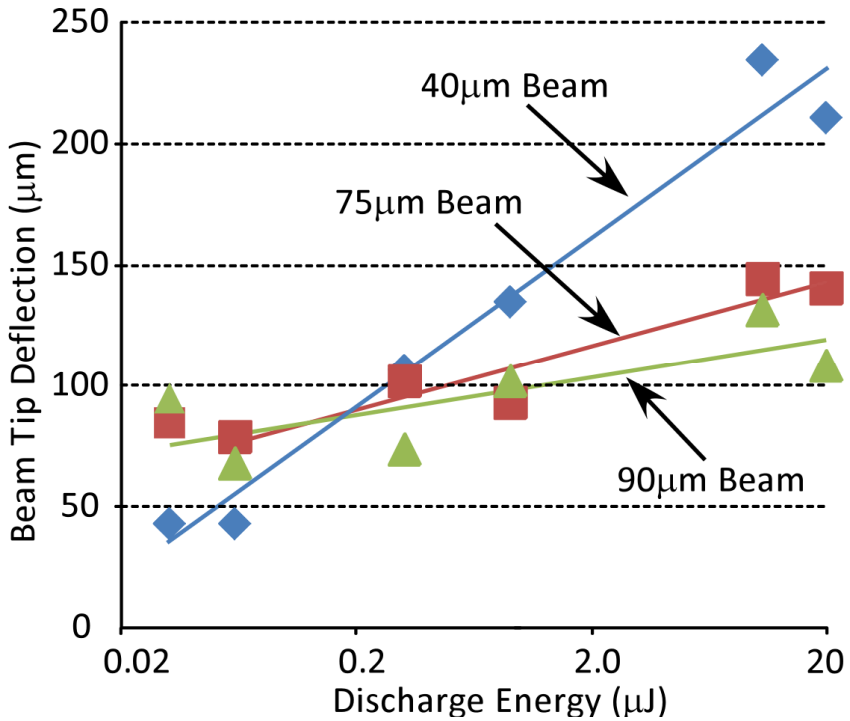

Fig. 5-6: Tip deflection is smaller for thicker beams

The tip deflection vs. discharge energy data from the interferometer is plotted in Fig. 5-6 for the three beam thicknesses and six recast conditions. As expected, the thinner the beam the larger the deflection and with a steeper slope. What is unexpected though is that the 75 and 90 µm beams deflected more than the 50 µm beams at the two lowest discharge energies. The 50 µm thick and 100 µm thick control experiment beams had no deflection so there was no residual stress in the foil itself before machining.

5.3.2 Recast Measurements

For macro-EDM of non-hardenable steels such as #316L stainless steel there is little grain size growth visible under the white layer (recast), even at high discharge energies [Gha03]. This means that the stress from the recast should be localized around the

thickness of the recast at much lower discharge energies with a small heat affected zone. Measurements of the recast layer thickness are presented in this section.

Magnified SEM images of the beam attachment points for the 90 µm thick set are shown in Fig. 5-7. The beams all have similar lateral dimensions, ensuring a fair comparison. The distinction between the recast stress field and the un-machined area is clearly visible. The surface of the beam is distinctly rougher looking for the higher discharge energy stress field. The roughness comes from the pits of the individual discharges as described in Fig. 2-1. When the plasma channel collapses, the melted or softened hot metal in a small radius is exposed to a large pressure difference, causing a portion of the surface to be ejected as debris. The larger the discharge energy, the larger the pits and greater the roughness.

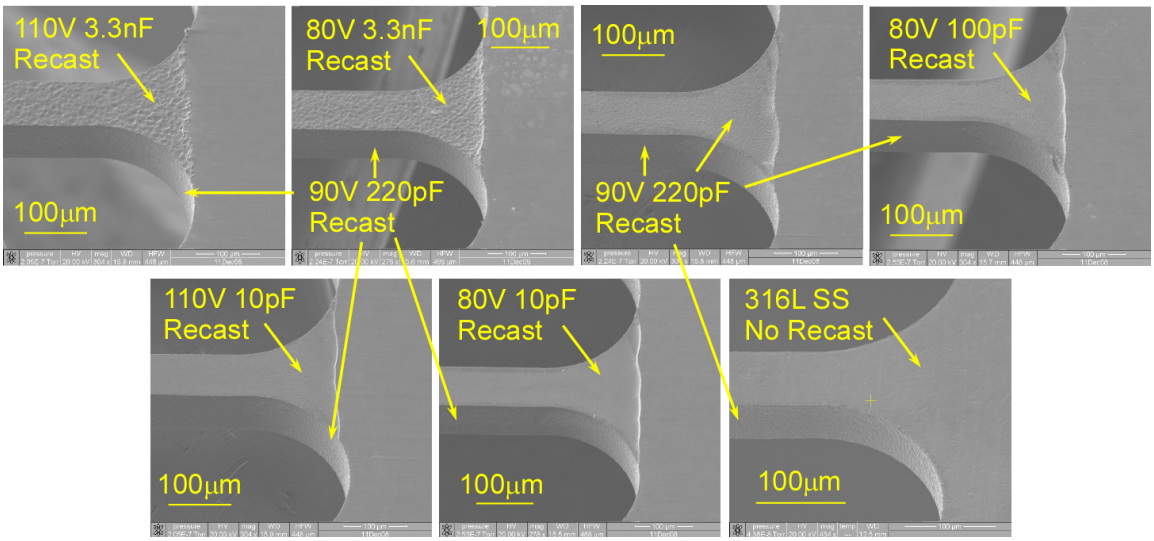

Fig. 5-7: SEM's of beam recast show increasing surface roughness with discharge energy.

A focused ion beam (FIB) was used to machine cross-sections into the stress fields to observe and measure the recast layers. A deep rough cut was followed by several

finishing cuts to provide a sharp view of the sidewall. In Fig. 5-8 the images are arranged from highest discharge energy in the top left to lowest in the bottom right. For the highest energy, the recast layer clearly extends a significant distance underneath the top surface (3.3 µm). At these energies a surface roughness measurement does not capture the full depth, only about the top 1/3. As the discharge energy is reduced, the thickness of the recast layer follows. The three lowest energies essentially were very close to the surface (<0.3 µm) and the lowest energy did not have any sharp edges on the discharge craters.

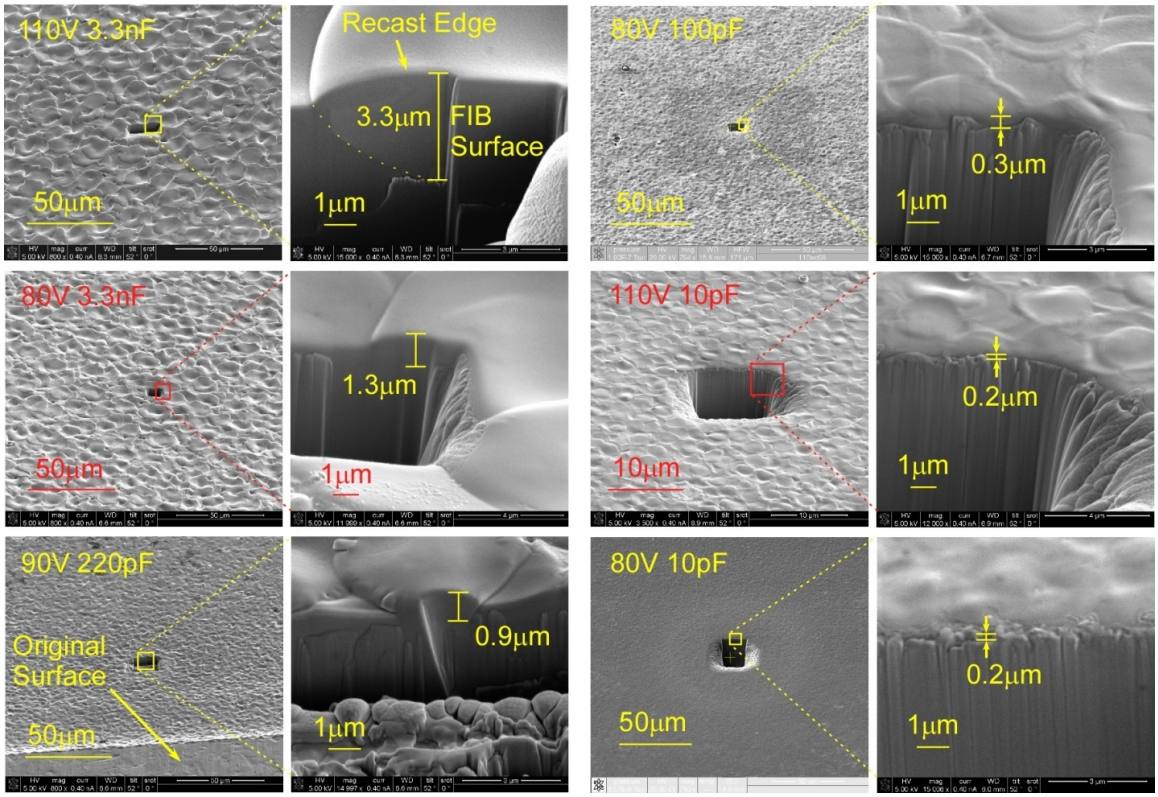

Fig. 5-8: Focused ion beam machined area of the recast is used to determine recast thickness. The 80V 10 pF recast (bottom right) was much smaller than the 110V 3.3 nF (top left). A significant amount of recast is under the surface for the high energy discharge.

Table 5.5: Recast parameters of 50 µm thick #316L

Recast Machining Parameters	Discharge Energy $E=CV^2/2$	Roughness Average Ra	Recast Thickness h
110V 3.3nF	20.0 µJ	0.40 µm	3.9 µm
80V 3.3nF	10.6 µJ	0.23 µm	1.3 µm
90V 220pF	0.90 µJ	0.20 µm	0.9 µm
80V 100pF	0.32 µJ	0.057 µm	0.3 µm
110V 10pF	0.061 µJ	0.06 µm	0.2 µm
80V 10pF	0.032µJ	0.06 µm	0.2 µm
Bare	0	0.01 µm	0

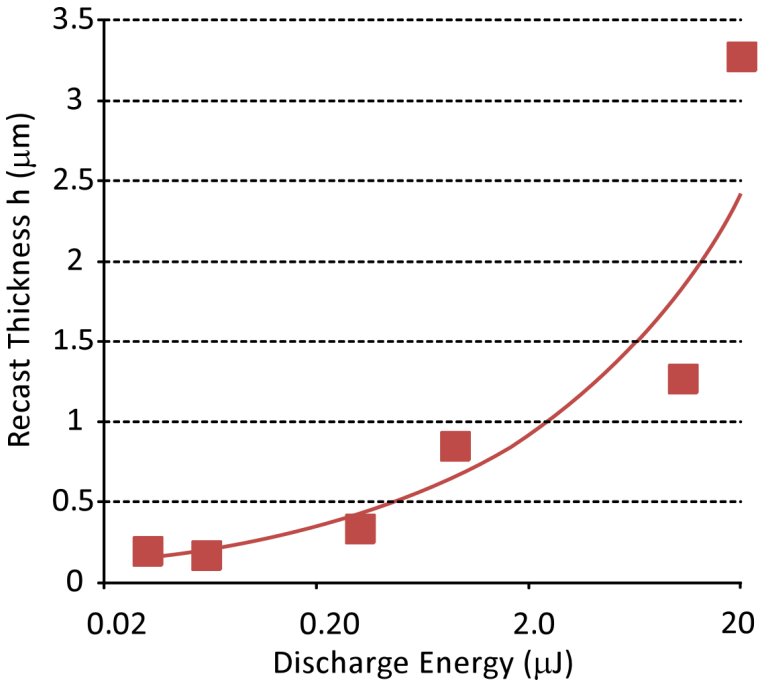

Fig. 5-9: Recast thickness measured using SEM imaging of focused ion beam machined sidewalls compared to using interferometer roughness.

The surface roughness of the stress fields was measured with the interferometer and is recorded in Table 5.5. Plots of the two sets of data are in Figs. 5-9 and 5-10. The observed recast thickness increases at a much faster rate with discharge energy than the roughness. This means that low energy machining effects are closer to the surface while high energy machining affects a layer much deeper underneath as well.

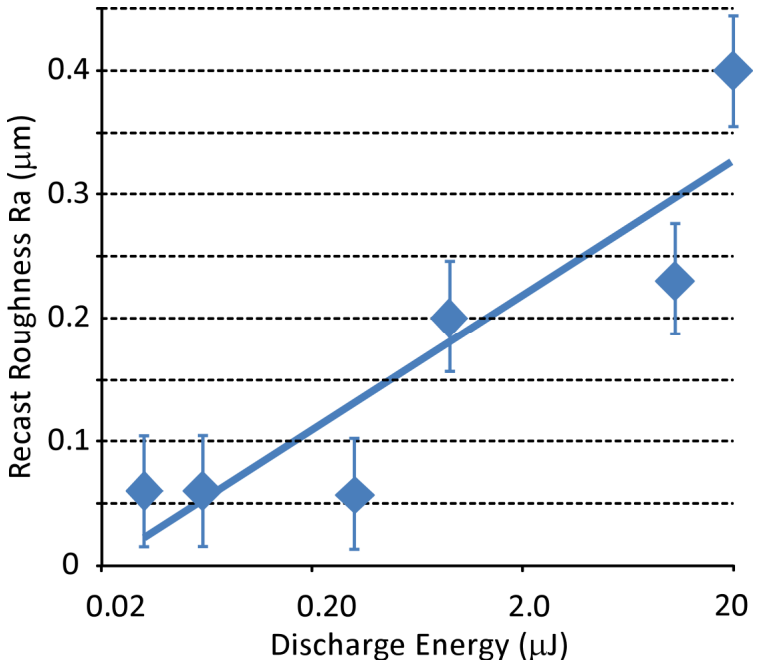

Fig. 5-10: The average recast roughness increased on a Log trend but was much lower than the observed recast thickness by FIB and SEM. Error bars are estimated measurement error for the interferometer.

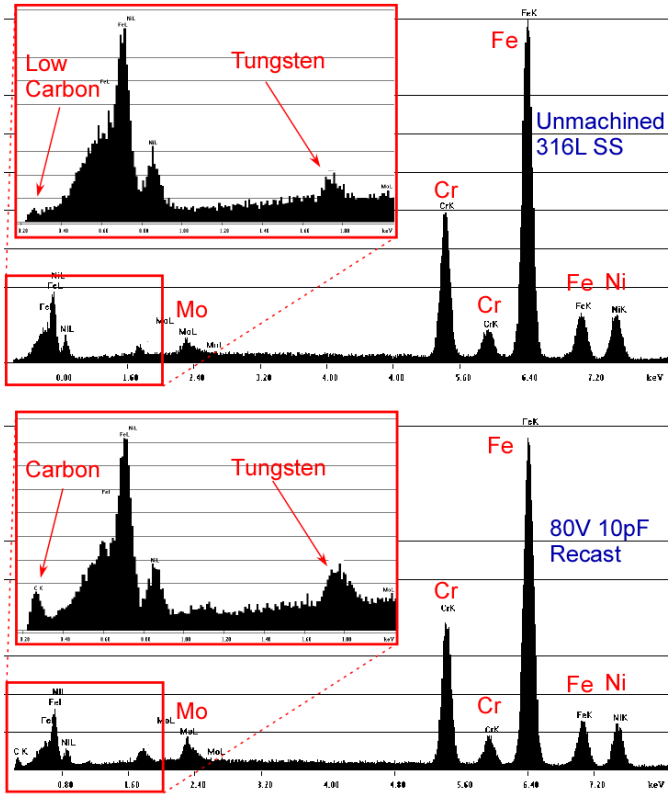

Fig. 5-11: EDX of recast composition. All recast layers had similar spectrum with elevated carbon compared to un-machined 316L SS.

The composition of the recast was recorded by EDX, showing elevated carbon content for each recast layer compared to un-machined steel, which is consistent with other studies in macro-EDM in Fig. 5-11. In those studies the concentration of austenite was significantly higher within the observed recast thickness, suggesting carbon uptake and hardening of the low carbon 316 steel [Ekme06, Ekme07]. This top 'white layer' recast is optically visible on the top surface but there is also a heat affected zone underneath that is not visible except perhaps by exposing the grain structure through etching or by X-ray diffraction stress measurement. Removing the white layer on stainless steel requires electrochemical etching because the surface quickly forms a passivation layer [Bhu05]. Removing the white layer is a common operation for stent manufacturers to do after laser machining for deburring.

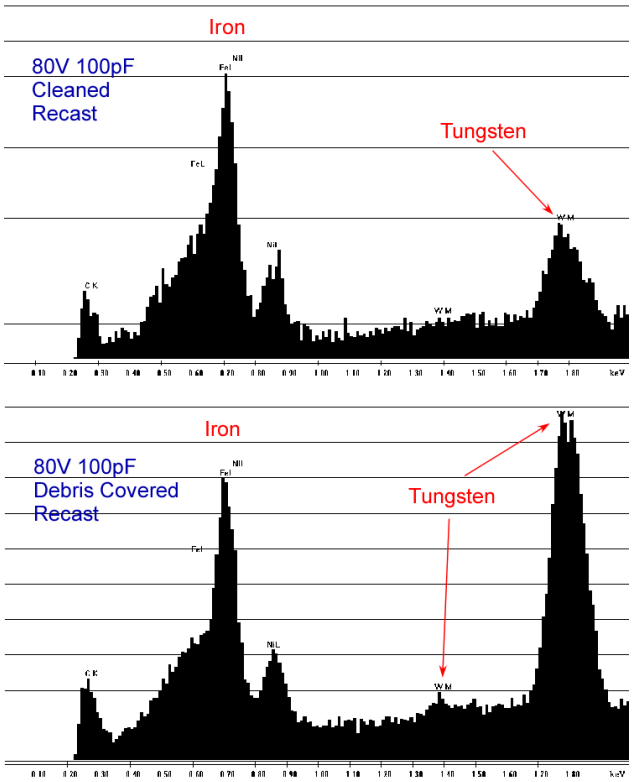

Fig. 5-12: EDX of cleaned recast surface compared to debris covered recast surface. There was a significantly higher concentration of tungsten in the debris while the other elements were about comparable.

An EDX comparison of a debris covered surface to a cleaned recast surface is shown in Fig. 5-12. There was significantly more tungsten in the debris than in the cleaned recast and un-machined surfaces.

5.3.3 Stress Analysis

By combining the collected measurements with the parameters in Tables 5.2 to 5.6, the stress of the beam and the original tensile stress of the recast can be calculated. First the modified Stoney equation is derived [Sen02, Zhao04] for the boundary conditions diagramed in Fig. 5-13.

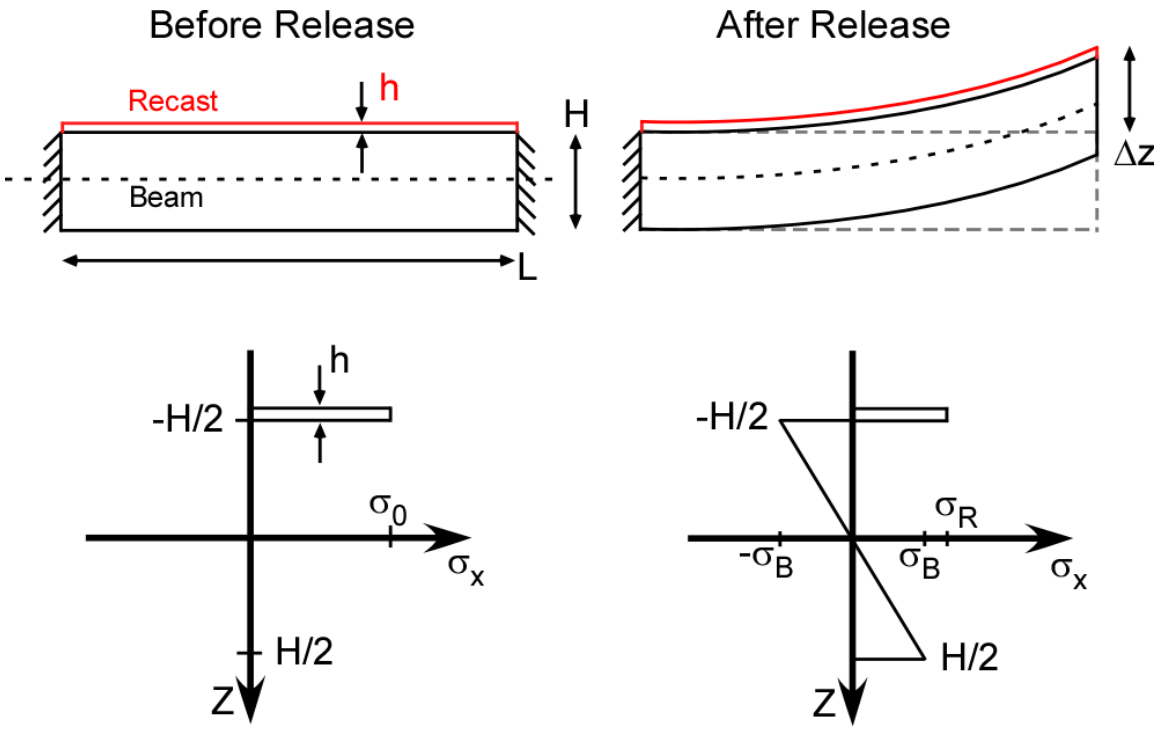

Fig. 5-13: Definition of terms for stress analysis. The cantilever beam initially is clamped at both ends with a recast thickness h and stress σ_0. After release the recast contracts axially to $\sigma_{0,Relaxed}$ then the beam deflects vertically by Δz and the recast relaxes to a stress σ_R and a stress gradient in the beam with magnitude σ_B at a z distance $\pm H/2$, which are the top and bottom surfaces.

Table 5.6: Material properties for #316L SS

Young's Modulus E	196 GPa
Poisson's Ratio υ	0.3
Beam Length	4 mm
Beam Thickness	40, 75, 90 μm

For the purposes of this study we assume that all the stress is in the 'white layer' recast, recognizing that there may be a heat affected zone that distributes it more evenly. The stress in the recast before release is σ_0 with thickness h and the biaxial Young's Modulus E_0. The thickness of the beam is H with beam biaxial Young's Modulus E_1. The Poisson ratio for the biaxial Young's Modulus is not shown until the end to simplify the algebra. We assume the biaxial Young's modulus of the recast is the same as the beam. After release there is an axial contraction strain

$$\epsilon_{ax} = \frac{\sigma_0 h}{E_0 h + E_1 H} = \frac{\sigma_0 h}{E(h+H)} \tag{5.1}$$

The stress in the recast and the beam after axial contraction are given by

$$\sigma_{0,relaxed} = \frac{E_1 H \sigma_0}{E_0 h + E_1 H} = \frac{H\sigma_0}{h+H} \tag{5.2}$$

$$\sigma_{beam,relaxed} = -\frac{h\sigma_0}{h+H} \tag{5.3}$$

After release the moment M is calculated

$$M = W \int_{-\frac{H}{2}}^{\frac{H}{2}} \sigma_{beam,relaxed} z dz + W \int_{-\frac{H}{2}-h}^{-\frac{H}{2}} \sigma_{0,relaxed} z dz \tag{5.4}$$

Since the recast is very thin compared to the beam the entire stress is effectively at –H/2

$$M = W\int_{-\frac{H}{2}}^{\frac{H}{2}} \sigma_{beam,relaxed} z dz + \sigma_{0,relaxed}\left(\frac{H}{2}\right) hW \qquad (5.5)$$

$$M = \frac{\sigma_0 H^2 hW}{2(h+H)} \qquad (5.6)$$

The moment of inertia I must be combined with the Young's Modulus E for a composite structure

$$EI = E_1 W\int_{-\frac{H}{2}}^{\frac{H}{2}} z^2\, dz + E_0 h(\tfrac{H}{2})^2 W \qquad (5.7)$$

But we assume the Young's Modulus of the recast is close to that of un-machined #316L stainless steel.

$$EI = \tfrac{1}{12}H^2(E_1 H + 3E_0 h)W = \tfrac{1}{12}H^2 E(H+3h)W \qquad (5.8)$$

The radius of curvature ρ for a thin film on a cantilever beam is given by

$$\rho = \frac{EI}{\mathrm{M}} \qquad (5.9)$$

Substituting the Moment M, Young's Modulus, and Moment of Inertia

$$\rho = \frac{\frac{1}{12}H^2 E(H+3h)W}{\frac{\sigma_0 H^2 hW}{2(h+H)}} \qquad (5.10)$$

Rearranging to solve for the original stress of the recast and inserting the Poisson ratio to account for the biaxial Young's Modulus is the modified Stoney equation.

$$\sigma_0 = \frac{E(H+3h)(H+h)}{6\rho h(1-\upsilon)} \qquad (5.11)$$

The radius of curvature can be approximated when Δz is much smaller than the beam length L by

$$\rho \approx \frac{L^2}{2\Delta z} \qquad (5.12)$$

allowing the original recast stress to be approximated [Hua04]. The maximum stress in the beam after bending is found at Z=±H/2 giving

$$\sigma_B = -\frac{3\sigma_0 h}{H+4h} \qquad (5.13)$$

Substituting for σ_0 and ρ

$$\sigma_B = -\frac{E(h+H)\Delta z}{2L^2(1-\gamma)} \qquad (5.14)$$

The stress gradient in the beam is given by

$$\frac{d\sigma_B}{dz} = \frac{E(h+H)\Delta z}{HL^2(1-\gamma)} \qquad (5.15)$$

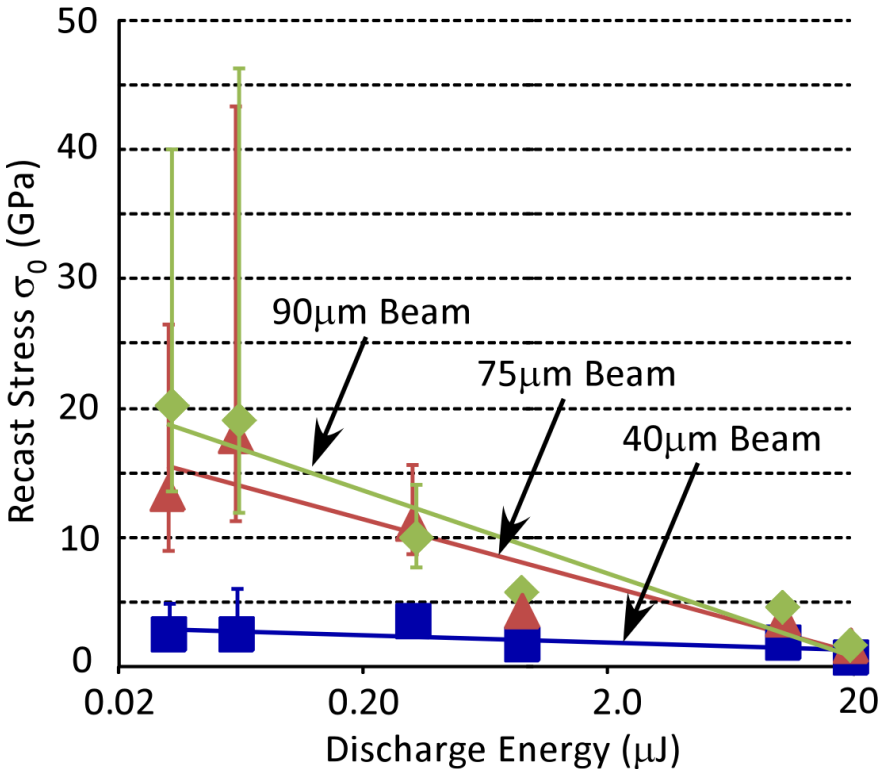

Fig. 5-14: Recast stress is higher at lower discharge energies but is concentrated into a smaller thickness. The higher discharge energy recast stress is distributed over a larger thickness. Thicker beams had higher stress. Error bars are the combined measurement error for all recorded data used in the calculation.

The recast stress vs. discharge energy is plotted in Fig. 5-14 has a range from 0.8-20 GPa for discharge energies from 0.03-20 μJ. The calculated stress of the low discharge energy is higher than the high energy discharges. Stress is also higher for the thicker beams than the thinner. Error bars were much higher for the two lowest energy discharges because the recast thickness was so small. The measurement error used was ± 0.1 μm for recast thickness and ± 1 μm for tip deflection, beam thickness, and beam length.

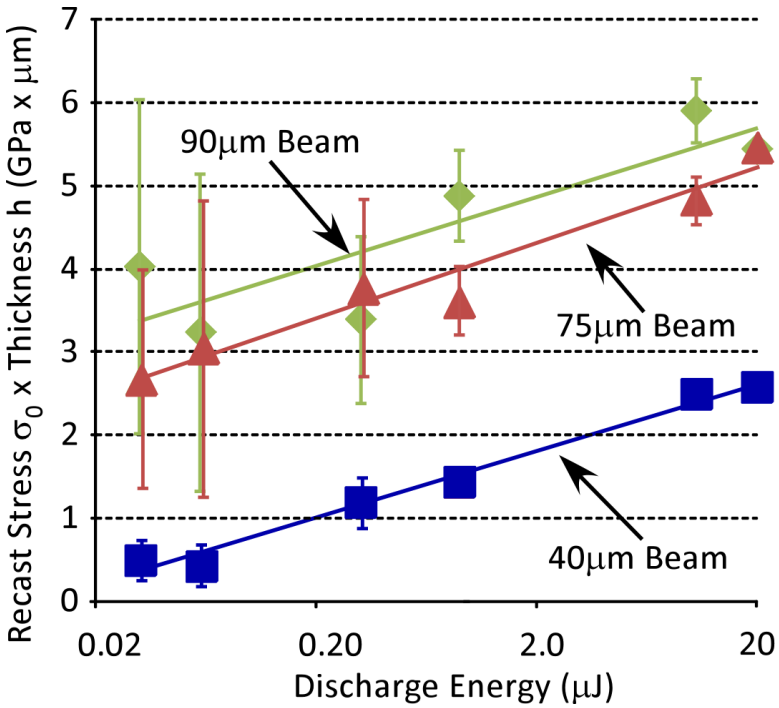

Fig. 5-15: Recast Stress x Thickness has the same slope for each beam thickness.

Figure 5-15 plots the recast stress x thickness vs. discharge energy. It is essentially Fig. 5-9 combined with Fig. 5-14. Since the discharge energy affects both the stress and thickness of the recast this plot shows the total impact of the recast layer. This plot enables comparison with residual stress studies that include a heat affected zone. A minimum stress thickness product of 430 MPa-µm to 3.3 GPa-µm was found for the 61 nJ discharge recast. Regular EDM is 25 GPa-µm which is 7.5 to 50x larger. Note that while the trend lines don't overlap each other, the slopes are parallel for each thickness and in ascending order, showing consistency. This suggests that there may be further beam thickness related trends at work. Even though there was no intrinsic residual stress as demonstrated by the control structure, one possible factor is that the 75 and 90 µm

beams were machined from 100 μm foil while the 40 μm beam was machined from 50 μm foil.

Figure 5-16 plots the stress gradient in the beam vs. discharge energy. The thicker the beam the lower the stress gradient because the stress is further distributed. A beam stress gradient of 1.5-3.5 MPa/μm is found for the 32 nJ discharge energy recast layer. The calculated maximum stress and stress gradient in the beam have low measurement error because they are less affected by error in the recast thickness measurement.

By comparison, a macro-scale EDM study using discharges at 5x current and 1000x discharge pulse time on #316L stainless steel had a gradient of 20 MPa/ μm [Gha03]. In that study, residual stress was measured using the X-ray diffraction method up to 90 μm below the surface. A maximum stress of 475 MPa was 40 μm below the surface but the sample was fix and unable to bend. Surface cracks observed in the recast at those energies could have contributed to a relieved stress of 360 MPa at the surface [Gha03].

The maximum stress imparted on the beam vs. discharge energy for the current work is plotted in Fig. 5-17. Even though the calculated stress of the recast was much higher than that measured in the cited study, all the points on the plot for stress imparted on the beam are much lower. A beam stress of 112 MPa was generated by the 61 nJ discharge energy recast layer. The 40 μm beam had the lowest stress at 33 MPa but it is also the most compliant and could bend the most to relieve stress.

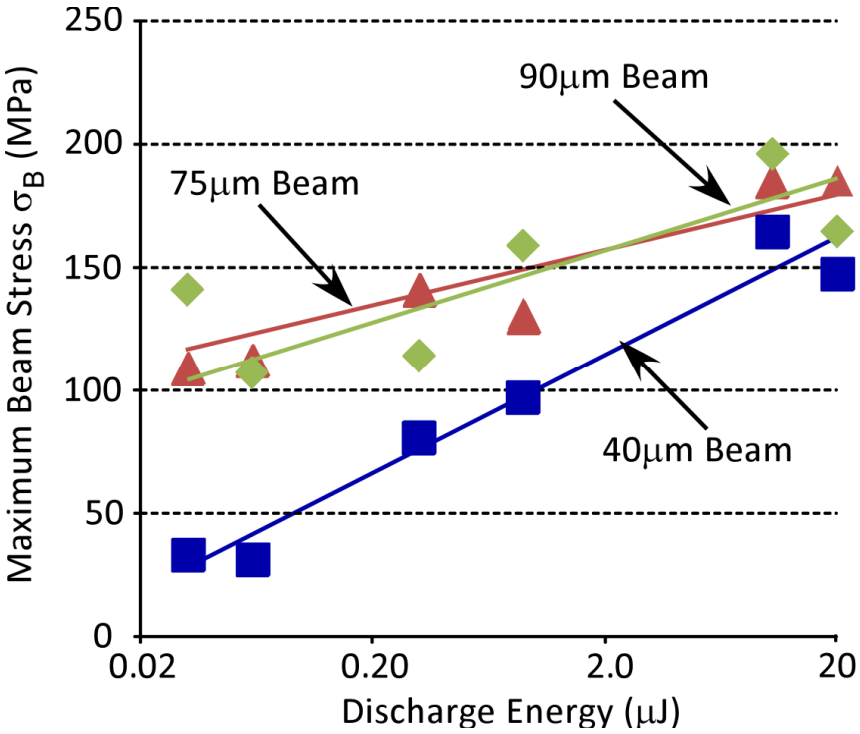

Fig. 5-16: Beam stress after bending is much lower than the recast stress. A minimum stress of 33 MPa is found.

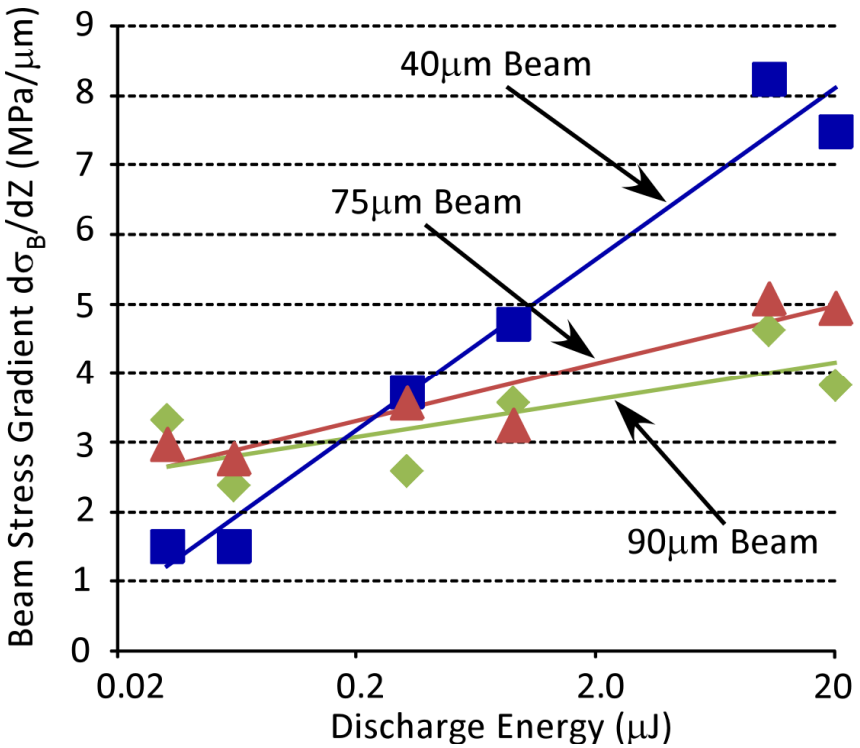

Fig. 5-17: The stress gradient $d\sigma_s/dz$ vs discharge energy has the same shape as tip deflection. The thicker the beam, the lower the stress gradient.

5.4 Discussion

Machining beams of three different thicknesses (40, 75, 90 μm) gives different deflections for a given recast. The diagram in Fig. 5-18 shows a cross-section of the released beams. The control structure has recast layers on the sidewalls but nothing on the top surface, keeping it in plane with the surrounding workpiece. The low energy discharge recast causes a small deflection while the higher energy discharge recast causes a larger deflection. Using high energy discharges for a thin beam causes an even greater deflection.

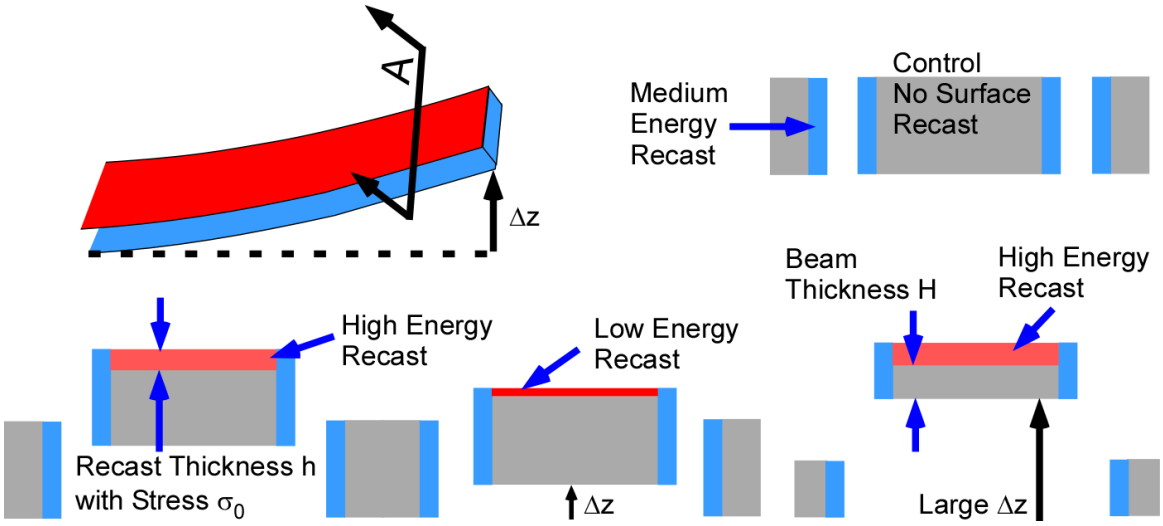

Fig. 5-18: Beam thickness and recast stress/thickness both affect the final deflection height. The control structure has balanced recast layers and so does not deflect at all.

The calculated stress levels of recast layer in Fig. 5-14 are beyond the 485 MPa bulk tensile strength of #316L stainless steel. One factor that may help explain this is that past studies have shown an uptake of carbon and hydrogen during machining that hardens the recast significantly compared to an un-machined surface [Ekme07, Gha03]. The EDX plots in the previous section did show elevated carbon levels on the surface. Work on

nanocystalline #316L austenitic stainless steel has shown that yield strengths of 1.45 GPa and tensile strengths of 1.55 GPa are possible [Che05].

A more likely scenario is that there is in fact a small heat affected zone that distributes the stress more evenly. Future work could use the X-ray diffraction method to check if the residual stress extends beyond the low energy discharge recast layer visible by FIB. Imaging of the grain structure underneath the recast would also be useful but is difficult because the recast is thin. An insulating coating could be used to protect the top surface while a Nital etch (4% nitric acid in alcohol) is used to expose the grains on the sidewall.

A heat affected zone would also explain the unexpected higher tip deflection result for the two lowest discharge energies as well as the thickness related stress differences in Figs. 5-14 and 5-15. A hypothesized residual stress profile for these beams is diagramed in Fig. 5-19. In the ideal beam model used in this study the stress is confined to a finite recast thickness h. In this model, the entire tensile stress of the recast is in the top half of the beam.

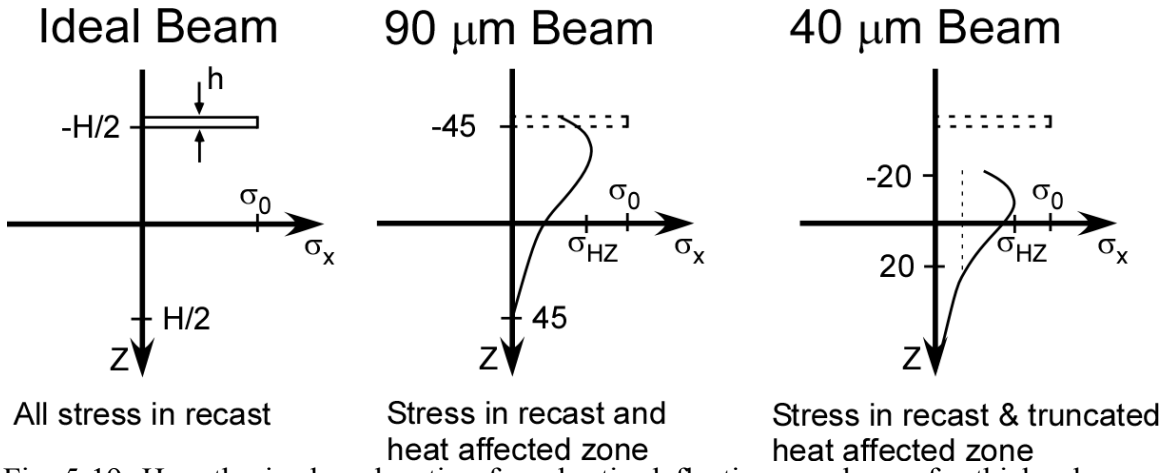

Fig. 5-19: Hypothesized explanation for why tip deflection was larger for thicker beams at low discharge energies. A heat affected zone that spans more than half a thin (40 μm) beam could partially balance out the tensile stress compared to thicker beams (75, 90 μm).

For a heat affected zone model, the 90 μm beam has a stress profile that is less than the full thickness of the beam. However, for a thin 40 μm beam, the stress profile is larger than the thickness beam. Tensile stress is added to both the top and the bottom half of the beam, reducing the stress gradient. This leads to a smaller deflection for the thin beam because the low stress regions at the bottom are removed. If this scenario is correct, it would suggest that the heat affected zone for the two lowest energy discharges is probably somewhere between 40 and 75 μm. This is significantly less than 90 μm for macro-EDM.

By selective patterning of high energy and low energy discharges, these stress levels could be used to shape metal structures. Bending of foil by EDM discharge has been demonstrated as a proof of concept [Yeo04]. Recast at these discharge energy levels is largely in the form of melted metal surface roughness. In many cases, stress from the recast will not affect the finished structure because it is balanced as in the control structure. However, in structures with long meandering patterns, even slightly unbalanced geometry can add up to a significant deformation. This was a significant challenge encountered during machining of a high density batch mode μEDM antenna stent pattern. Since the structure was essentially one long meandering 100 μm square piece of stainless steel, it was susceptible to stress bending, even machining at the lowest discharge energy. Understanding the stress contribution of recast leads to higher precision machining with μEDM [Han06].

CHAPTER 6

CONCLUSIONS & FUTURE WORK

6.1 Conclusions

High density micro-electrodischarge machining has the potential to improve throughput of precision micromachining of bulk metal foils beyond the capability of other available technologies. The goal of this work was to investigate the fundamental challenges in scaling batch mode micro-electrodischarge machining to small dimensions with high feature densities. This was accomplished through several studies into different aspects of the problem.

A parametric study showed the impact of scaling tool feature width and tool spacing on discharge gap and tool wear. Debris accumulation and gas trapping in the features can constrain precision in a significant way due to a corresponding increase in spurious discharges. For isolated features, simulations showed that the escape path for debris at the corners can cause uneven tool wear and discharge gaps. As multiple features are packed closer together, debris effects increase. The smallest features (10 μm width) required the lowest machining tolerance to produce the desired pattern but with a tradeoff in tool wear. Feature widths of 25 μm provided a compromise between tool resiliency and machining tolerance. Finally, non-uniform tool wear becomes worse as the size of the global pattern increases, even if the fill factor remains constant. These guidelines are very valuable for applying to future device machining efforts.

Since spurious discharges due to debris accumulation were suspected of causing the damage to the tool and workpiece, two debris handling techniques were developed. A tool sidewall passivation coating was used to limit the discharge location to the top surface of the tool. The 2000 Å silicon coating added a series resistance that prevented debris from triggering spurious discharges when trapped in the discharge gap. Tool wear for the test pattern improved from 34% for the uncoated tool to a typical rate of 1.7% for the coated case. Depth uniformity also improved by 78% across the pattern.

A hydraulic flushing technique used through-holes in the workpiece to allow the bubbles naturally formed during machining to pull the debris away from the discharge site. It was shown that not only high density patterns but enclosed patterns are susceptible to debris accumulation. A 2x improvement in throughput was achieved and an analysis of the hydraulic resistance showed a showed a 53x reduction.

The inherent wireless signal information generated with each discharge gives direct information on the discharge quality that is less affected by terminal parasitics. The metal-metal interface between stainless steel and electroplated copper showed a 10 dBm shift in intensity for the 300-350 MHz band and a 5 dBm average change across the full 1 GHz bandwidth. This type of metal backing layer is a convenient way of restraining micromachined structures during machining to prevent stress relieved bending that could cause damage. Debris accumulation gave a 4 dBm drop in the 800-850 MHz band and 2.2 dBm across a 1 GHz bandwidth. This type of monitoring could potentially be used to monitor multiple machines at once.

The residual stress due to the thermal recast layer left behind on the surface of the workpiece after the μEDM discharge process was investigated. This was the first

residual stress study for µEDM. The discharge energy levels used were far lower than those used in the stress studies reported in the past. The recast layer was imaged and the stress level calculated from the beam geometry and tip deflection. A clear logarithmic trend related stress to discharge energy level.

6.2 Future Work

The improved machining quality due to the tool passivation coating and hydraulic flushing demonstrated that importance of debris handling techniques. An alternative strategy is to use through-tool debris flushing as shown in Fig. 6-1 instead of through-workpiece as described in section 3.2. Since the tools for batch mode µEDM are patterned with photolithography, a natural extension would be to use DRIE to create the through-holes across the pattern. The approach is compatible with using multiple circuits in batch µEDM.

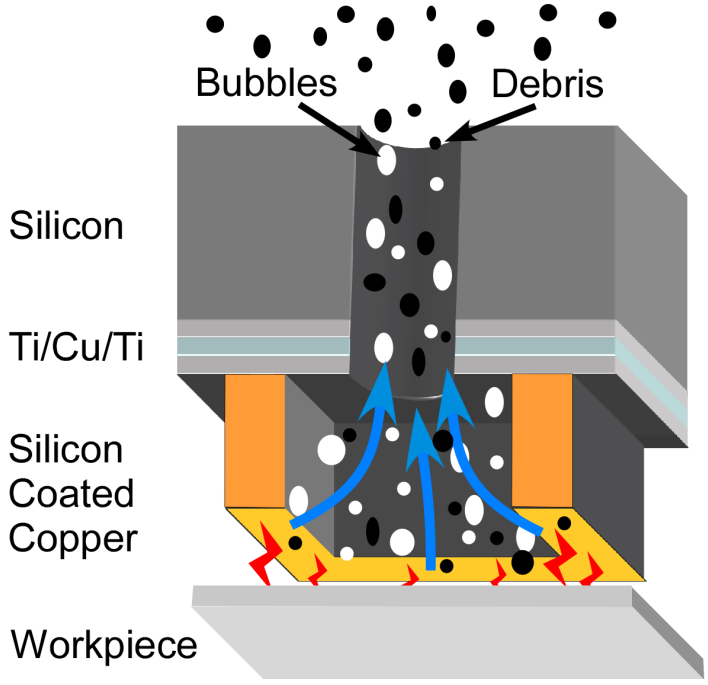

Fig. 6-1: Integrated through-tool hydraulic flushing for high density batch µEDM would allow debris to escape without requiring a through-workpiece machining step.

This would allow hydraulic flushing in workpieces that are thicker than the tool height. It also is a single step machining process since the through-workpiece step is not needed. A single step process relaxes the requirement to align the tool to the stage axis and allows the tool to be mounted on the mandrel, which is more convenient for viewing the workpiece during machining.

An alternative form of wireless interface sensing is to use a material stack designed to change the parasitic loading on the discharge terminals as machining progresses to the backing layer. For example, in Fig. 6-2, the device layer could be separated electrically from the backing layer by a thin resistive layer such as sputtered silicon (with adhesion, seed layers). If the workpiece were connected electrically only by the backing layer, the resistive layer would limit the current draw during each discharge. When the tool punches through the device layer, the thin resistive layer would also be penetrated, changing the parasitic resistance of the workpiece, the energy per discharge, and therefore the wireless spectrum.

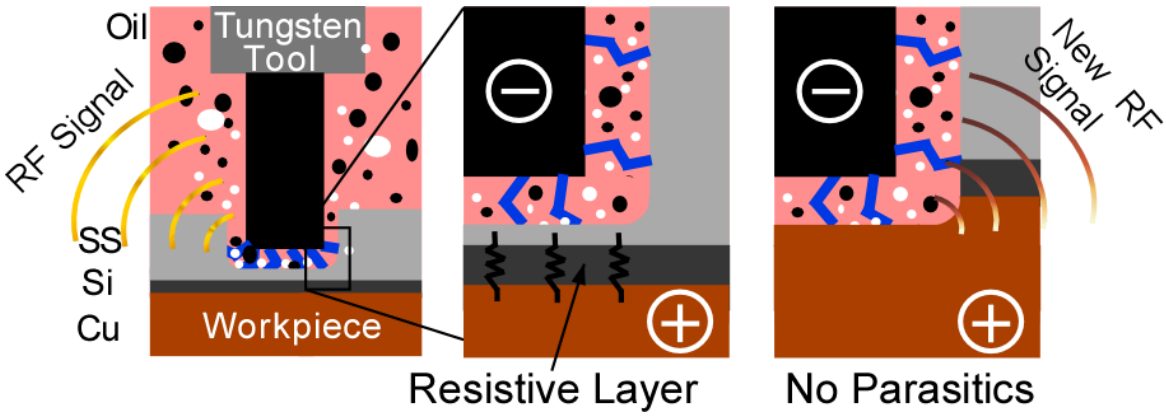

Fig. 6-2: Alternative interface sensing approach. A thin resistive silicon layer separates stainless steel device layer from copper backing layer. When the silicon layer is penetrated, the parasitic resistance is eliminated, changing the discharge energy and wireless spectrum.

One application of high density batch μEDM is the fabrication of a high-Q antenna stent for sensing on an arterial wall. The stent is used as both a mechanical scaffolding and as a wireless inductive antenna. Past work by Takahata and DeHennis showed that the pressure from an obstruction in a stent can be sensed with capacitive pressure sensors in vitro [DeH04, Tak05]. In Takahata's work the stent inductor forms an LC resonant tank with the pressure sensors. The wireless resonant frequency shifts as the pressure changes. However, the transmission distance was limited by the Q of the LC tank. Increasing the number of turns in the inductor through geometry changes and decreasing parasitic resistance would increase the transmission distance.

High density batch mode μEDM is a technique for precision machining of moderate size patterns while PCE is a lower precision technique for machining large patterns in high volumes. By using μEDM for high precision features and PCE to pattern the bulk metal substrate quickly, the advantages from both could be maximized. The work presented in appendix A is an investigation into the feasibility of fabricating a high-Q antenna stent.

Another application of the technology is a project that helped motivate this research. The bi-stable electrothermal single pole single throw stainless steel RF Switch presented in appendix B required high density features machined by batch μEDM. The use of μEDM allows many more materials than are available by thin film deposition without the difficulty of tight process control. Significantly higher power handling is also possible because the features are bulk material instead of thin films. The challenge with the design that was encountered was that at depths greater than 25 μm, the 5 μm minimum

features were very difficult to prevent from being destroyed by spurious discharges from debris. The test structures used in the passivation coating experiments were similar to those used in this project and a 4.5 μm beam was readily machined by that technique.

There are many applications where the results from this research can be applied. A CAD tool to apply the results from the parametric study in chapter two would reduce the need for process development for each new pattern.

The simple fabrication process of SU8-LIGA makes batch mode μEDM significantly more accessible than in the past. The creation of a μEDM controller that can handle natively handle multiple discharge circuits would further increase its adoption.

APPENDIX A

A HIGH-Q INTEGRATED ANTENNA STENT SENSING PLATFORM

In order for batch mode μEDM to gain acceptance in industry it is critical to demonstrate its advantages through targeted applications. The patterns where batch mode μEDM may be viable are in large, high resolution patterns manufactured in high volumes. One potential application that will be investigated here is in cardiovascular stents.

The widespread adoption of stents has had a large impact on cardiovascular intervention over the last 15 years [Col02, Pal04]. Since around 2003, drug coated metal stents have been used to minimize restenosis, which is a re-narrowing of the vessel lumen and the primary side effect of balloon angioplasty and stent placement. However the long term effects are still being studied and there is still a small percentage of patients whose vessels do not respond as expected and restenose.

Past work in our group has shown that capacitive pressure sensors can be used to wirelessly detect an in vitro blockage in a stent which also acts as an antenna. In this work we investigate the feasibility of fabrication and in vivo testing of a high-Q antenna stent using a hybrid μEDM and PCE process. A new pressure sensor concept is also presented. The chapter is broken down into an introduction to stent technology (6.1), pressure sensing feasibility (6.2) fabrication and design of the proposed device (6.3), and pressure sensor design (6.4).

A.1 Stent Background

Stents are structures used to scaffold an artery (or other vessel) open after balloon angioplasty, relieving a constriction (stenosis) and improving flow. A wide range of vessels, tubes, and ducts in the body can be stented to relieve constriction including the coronary, pulmonary, and carotid arteries, biliary duct, and esophagus [Al-M04, Serr98, Sest04]. Stents are most often constructed from biocompatible stainless steel and permanently expanded by a balloon to the proper diameter during a procedure called percutaneous transluminal angioplasty [Col02]. A common problem with standard bare metal stents is that the healing response of the artery is often overcompensated to the point of re-narrowing the vessel back to a much smaller diameter (restenosis) [Fax02]. An artery may narrow by up to 70% before symptoms of fatigue and chest pains are detected, which can be catastrophic.

Recently, drug-eluting stents (DES) have reduced the occurrence of restenosis [Berg07], but studies have reported an elevated risk if late stent thrombosis (blood clotting in the stent long after insertion) occurs. Patients are temporarily put on anti-platelet (or anti-clotting) medication after the procedure but the thrombosis symptoms begin to occur when the medication is stopped [Cam07, Ell06]. Bare metal stents have a thrombosis rate of 0.6-0.8% but are fatal in 16.7-20.8% of those cases. In DES, the rate is 0.27-0.7% but is fatal in 45% of those cases, with the majority of the remaining surviving a myocardial infarction (heart attack) [Jon06]. These results have called into question the long term viability of DES to minimize risk.

The long term effects are still being studied but unfortunately, there currently is no non-invasive way to follow-up and monitor the environment around the stent after it has

been implanted. Traditional x-ray angiography cannot provide the necessary resolution and requires percutaneous catheterization to inject contrast solution. Catheter based pressure sensors can be inserted but also require angiography to guide to the proper location [Chau87, Chan02]. The results cited in the previous paragraph were from an autopsy study.

It would be beneficial to have a long term sensor to detect if/when there is restenosis before intervention becomes critical. In addition to improved patient care [Pal04], it would help in the evaluation of new stent technologies [LaD05] and intervention techniques. Also, in the event of a critical intervention such as a myocardial infarction, if the time between first symptoms to reopening the vessel with balloon angioplasty is greater than 4 hours, the 1 year mortality rate doubles from 5% to 10% [DeLu03]. An embedded sensor could help quickly diagnose if the cause is in the vicinity of the stent while en route to the hospital.

A.2 Stent Fabrication and Design

Stent fabrication is traditionally performed by laser cutting slots into 100-200 μm thick #316L stainless steel tubes. A carefully pleated angioplasty balloon is then inserted into the stent which is firmly crimped (compressed) onto the balloon. The pleating of the balloon ensures the balloon deflates to the original shape and does not snag on the stent struts. Crimping ensures a low profile as the stent traverses the arterial system to the deployment site. When the balloon is expanded, the slots enable significant radial expansion that is maintained after deflation due to plastic deformation of the steel.

A different approach, starting with a planar foil instead of a tube, enables sensors to be integrated into the stent in ways that would be difficult otherwise. The planar approach also allows more machining technologies to be used to batch fabricate many stents in parallel.

A drawback of laser machining is that it is a serial process, limiting throughput and design complexity. In past work from our group, it was demonstrated that a planar approach using batch mode (μEDM) could increase throughput, design complexity, and feature density [Tak02]. The drawbacks of using a planar approach are added complexity for balloon mounting and crimping, and depending on the pattern, lower feature density. Thinner struts have been shown to reduce restenosis but have lower mechanical performance [Brig02]. Therefore the goal should be to have a high density of thin struts to compensate. High density batch μEDM is a good candidate for this machining process because it has high precision at high throughput and can machine biocompatible #316L stainless steel.

The additional process steps for creating a sensor directly on a stent introduces a risk of deforming the structure simply by handling the device. The over sized stent pattern can be surrounded by a handling ring connected with tabs that support the stent during cleanroom processing. For example, Cr/Au deposition and the sensor fabrication and mounting can be done with less risk of deformation. The tabs are machined with EDM as needed for each step in the process.

The approach that should be used in designing new planar stents is to include as many interchangeable features as possible to increase the likelihood that there will be useable

stents in a single run. Features that are useful can be utilized while those that are not needed can be easily removed with EDM.

The next section is a new investigation into the complications of implanting sensors in the vascular system with a focus on the environment for pressure sensing. Monitored blockages in stents in vivo would give physicians critical information that could prevent dangerous patient complications.

A.3 Stents as a Pressure Sensing Platform

Traditional stent monitoring techniques are either incapable (angiography) or too invasive and costly (intravascular ultrasound) to use repeatedly after a stent has been deployed. Using a non-traditional planar approach to stent fabrication enables the integration of sensors that could provide information about the conditions directly surrounding the stent [DeH04, Tak05]. Wireless interrogation of proximal and distal pressure sensors to determine the severity of restenosis has been investigated in past work, shown bellow in Fig. A-1 [Tak05]. Implantable pressure sensors have also been investigated for other uses such as in abdominal aortic aneurysms [Fon06, Mok07, Naj04]. However, for application to sensing in an artery near a stent, a pressure sensor approach may be subject to large amounts of signal drift due to endothelial tissue growth on the sensors.

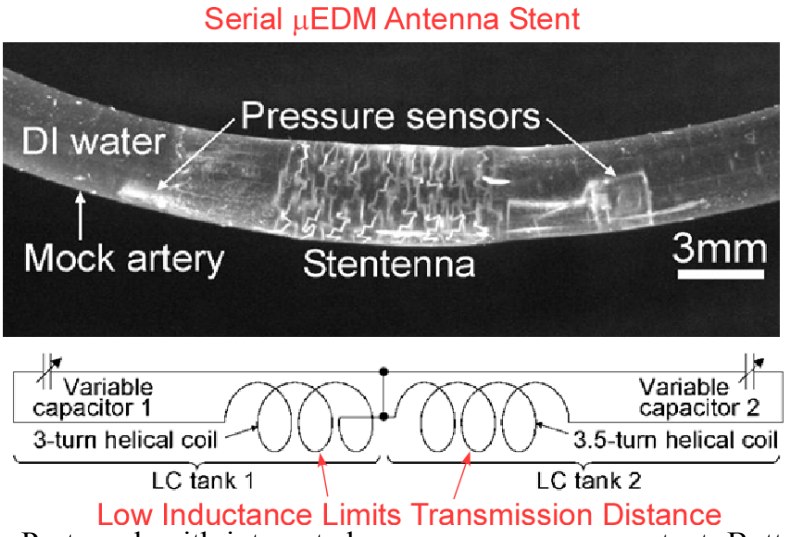

Fig. A-1: Top: Past work with integrated pressure sensors on a stent; Bottom: equivalent circuit [Tak05].

The sensing environment for an implantable pressure sensor on a stent is determined by the foreign body response of the surrounding tissue. In catheter based pressure sensors, sometimes used during stent placement to determine the degree of stenosis, the body does not have time to respond in a way that may impact the performance of the sensor. However, for permanent implantation, the sensor is subject to whatever reaction occurs. There may be no reaction or it may be completely encapsulated. The images in Figs. A-2 show the impact of drug eluting stents on neointimal growth (new tissue) and restenosis [Serr05]. The amount of tissue growth varies widely depending on the patient (age, diet, medication etc), the particular vessel (location, size/shape, %stretch, %stenosis, constitution), and the physician (technique, stent selection).

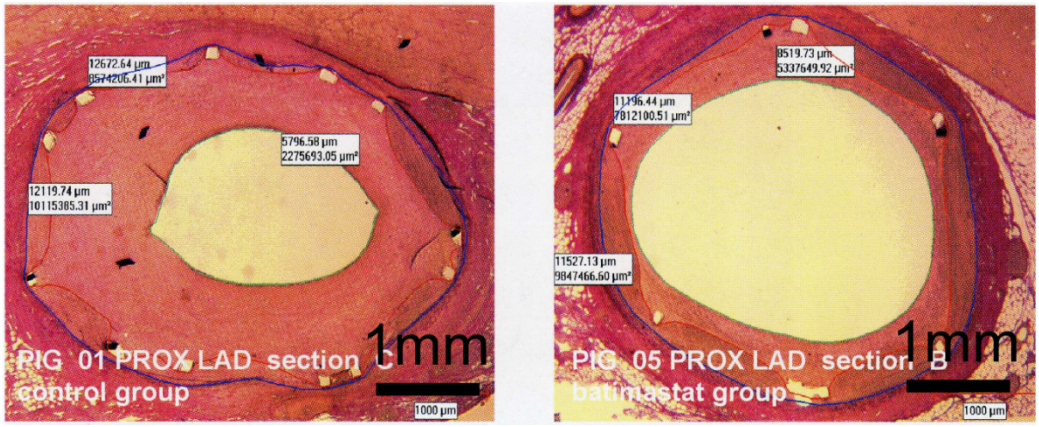

Fig. A-2: Bare metal stent (left) compared to batimastat coated stent (right). Adapted from [Serr05].

When a stent is first implanted, the artery is over-stretched and there is a natural healing response [Ell06]. The patient is put on anti-clotting medication to prevent catastrophic clots. Thrombus (blood clot) does form locally around the stent struts but is gradually taken up by the formation of new tissue [Serr05]. There may also be an inflammation response and injury response sue to the overstretch of the artery during balloon angioplasty [Korn98, Schw92]. At the end of this process there will ideally be around 50-200 µm of endothelial growth covering the stent but could be more in an abnormal response. The healing process begins immediately after stent deployment and concludes after around 6-12 months.

This ideal tissue layer thickness is also valid for drug eluting stents and at locations away from the occlusion site. The layer is desirable because it indicates a healthy healing process. If this layer is not present, as in overdosing of DES or brachytherapy (radiation), there is an elevated risk of late stent thrombosis (clotting) when the patient is taken off the anti-clotting medication [Ell06]. A DES essentially slows down or prevents the normal healing response of the artery [Jon06]. There is no way to tell if the stent has been fully endothelialized except possibly with intravascular ultrasound, which is invasive.

Proper sensor operation after partial and complete endothelialization must be seen as a critical design specification for a usable system. The sensor operating environment for various outcomes of endothelial growth as determined by this investigation is diagramed in Fig. A-3.

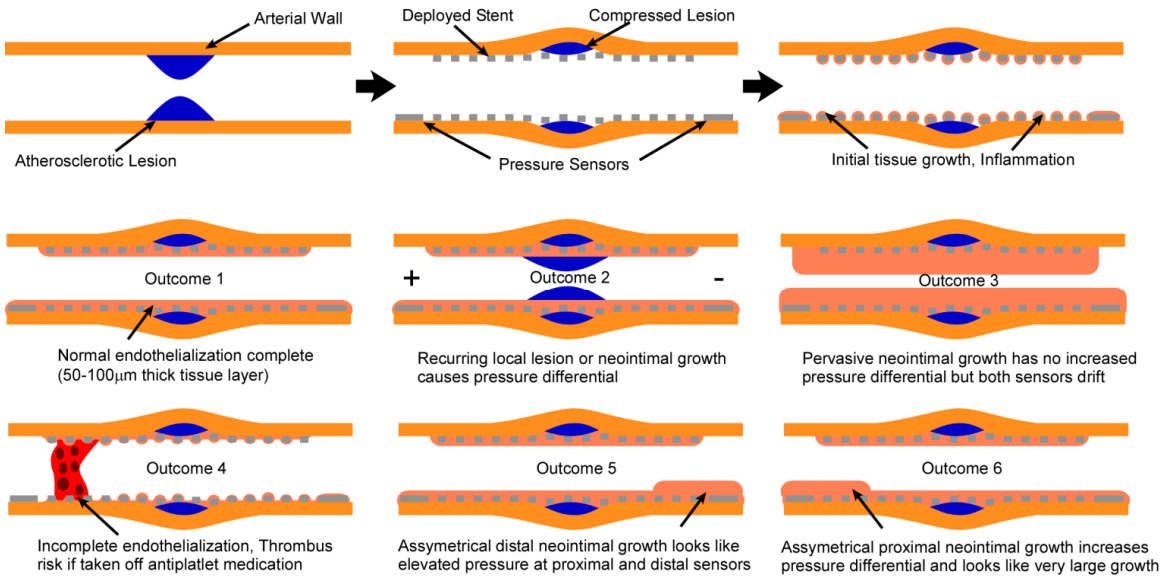

Fig. A-3: Operating environment for stent platform based sensors. Top row shows stent placement while bottom row shows 6 potential outcomes that would affect the sensor response differently.

The problem with variation in endothelial growth outcomes is that this can lead to variation in sensor readings. Without prior knowledge of the pattern of tissue growth, which currently is not possible except invasively, the interpretation of the sensor data could lead to a misdiagnosis.

This concept can be explored by looking at the impact of depositing tissue-like substances on a diaphragm based pressure sensor. Figure A-4 is from a theoretical model for determining the impact of atheromous plaque growth on an implanted pressure sensor

[Ste07]. As can be seen, the greater the thickness, the less the radial stress applied on the pressure sensor.

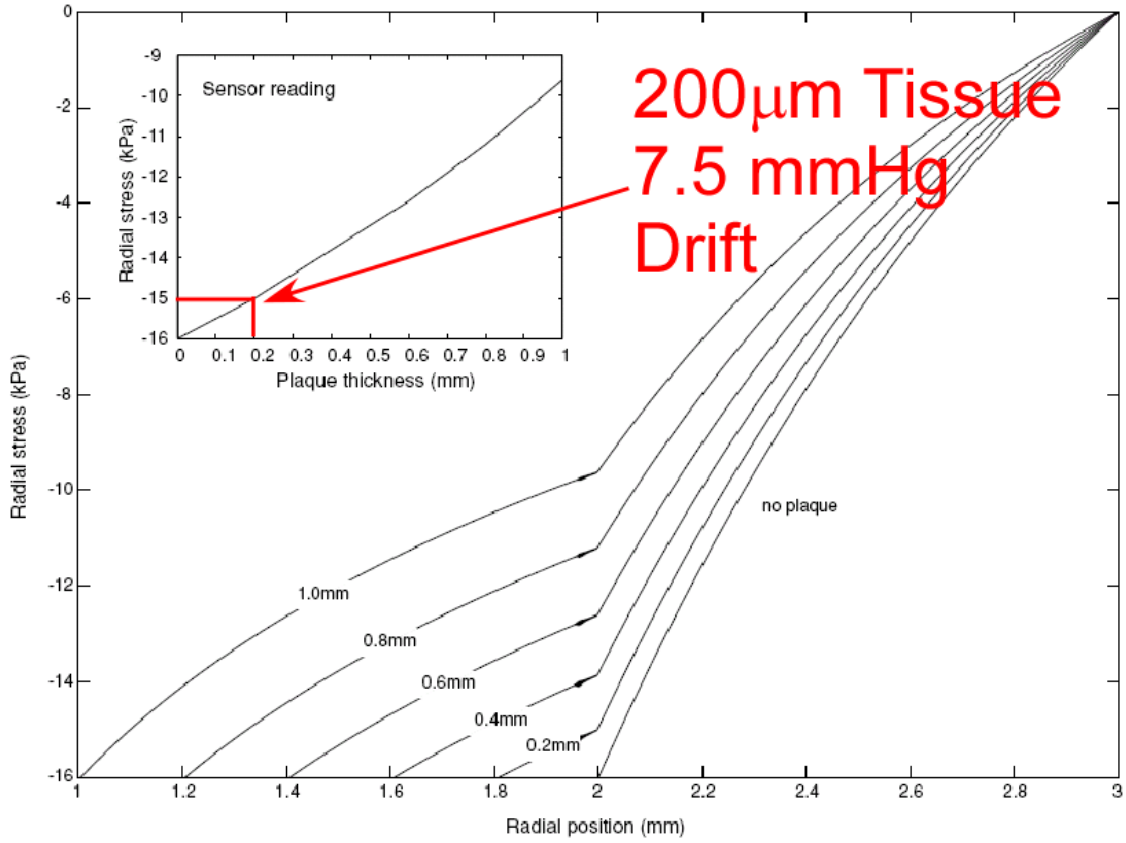

Fig. A-4: Distribution of radial stress through the thickness of the plaque and arterial wall for various thicknesses of atheromous plaque on a 1mm thick artery with 2mm internal radius. The inset shows the radial stress at the interface between the plaque and the arterial wall. Adapted from [Ste07]

The inset of Fig. A-4 gives the stress seen by the pressure sensor as a function of tissue thickness. The 1mm thickness corresponds to a 45 mmHg drift. The 200 μm thickness, which is a reasonable amount of growth, corresponds to a drift of 7.5 mmHg. For a maximum 200 mmHg dynamic range this is significant. At rest, for a normal pressure range of 40-60 mmHg that is a very large drift. The authors go on to conclude that the pressure sensor still provides intelligible data even with the plaque for pressure vs time [Ste07]. This is true to a limited extent, but the assumption is that the plaque will

grow uniformly and on top of the sensor. The images in Fig. A-5 clearly show that this assumption will not hold in many cases. In outcomes 5 and 6 in Fig. A-3, asymmetric tissue growth such as this can either mask or exaggerate the true condition of the artery. In outcome 3, large tissue growth over both sensors could be misinterpreted as an obstruction in the artery further upstream.

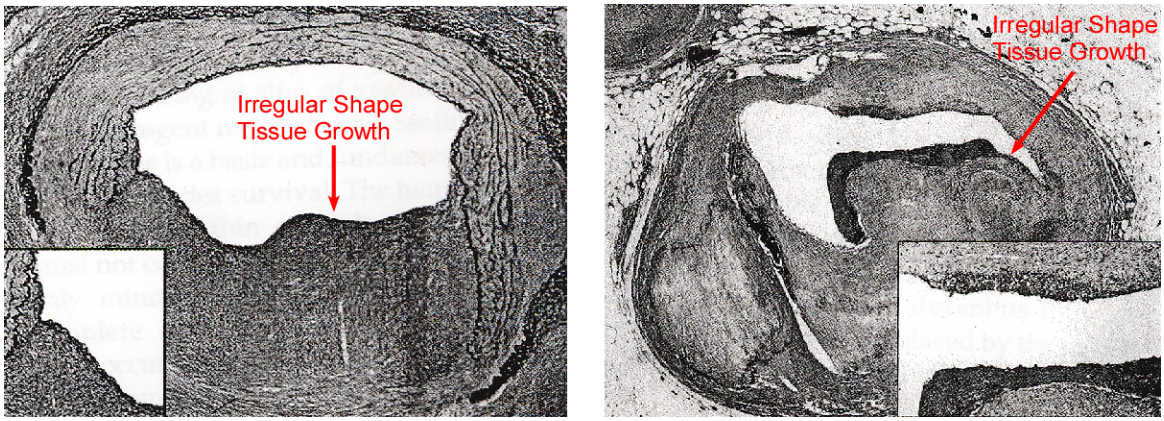

Fig. A-5: External radius of an artery of 2mm initial internal radius and 3mm initial external radius, subjected to a range of internal pressures and obstructed by stenoses of various thicknesses. Adapted from [Serr05].

The work by Schnakenberg shown in Fig. A-6 below inadvertently demonstrates the impact of this tissue growth on a pressure sensor [Schn00, Schn05] (red lines added for clarity). The mechanical characteristics of PDMS are similar to that of vascular smooth muscle. In this work, PDMS [Schn00] and parylene [Schn05] were used as insulating layers for the pressure sensor. The 0.5-1 mm of Sylgard 184 PDMS did not change sensitivity of the pressure sensor but did add a large offset drift. To put the figure into numbers in Table A.1, it is at worst a 0.06 mmHg/μm drift.

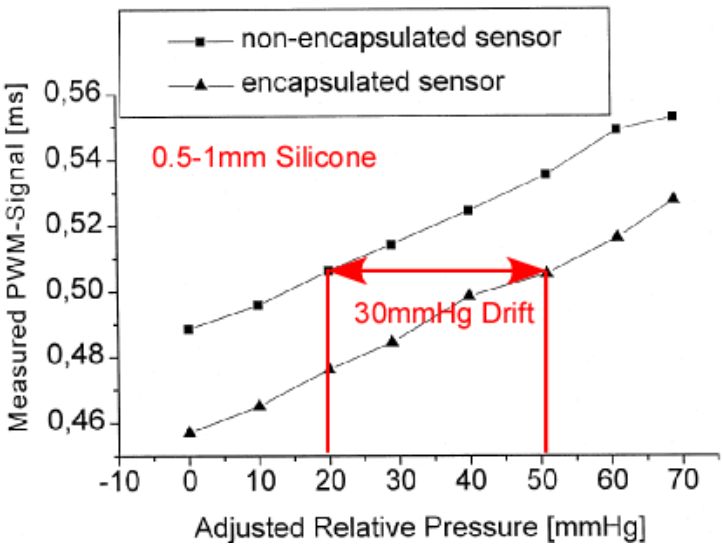

Fig. A-6: Pulse-width-modulated pressure signal of an encapsulated and a non-encapsulated pressure signal with respect to the relative pressure for a wire-bonded pressure sensor. adapted from [Schn00]).

Table A.1: Impact of tissue thickness on pressure sensor drift

Tissue Thickness	Pressure Drift
17 µm	1 mmHg
50 µm	3 mmHg
100 µm	6 mmHg
200 µm	12 mmHg
500 µm	30 mmHg

The minimum design target for a pressure sensor approach is to sense a 60-70% occlusion, which corresponds to just before the threshold for angina (chest pain). The pressure difference between the proximal and distal ends for this size occlusion is about 5-10 mmHg [DeH04]. The drift is then 50-200% for a nominal level of endothelial growth.

The diaphragm pressure sensor approach to sensing blockage will have significant challenges in resolution and reliability for diagnosing occlusions in an in vivo setting without knowledge of the amount of tissue growth causing sensor drift. Another issue is

size. In the work by DeHennis and Takahata, the pressure sensors used 200 μm thick pressure sensors. Mounting on a 100 μm stent pad brings the thickness to 300 μm which increases the thrombus risk and likely limit deployment to 3 mm diameter vessels. Direct process integration into the stent is an option but would require significant development. An alternative diaphragmless pressure sensing approach is investigated in the next section to see if some of the tradeoffs outlined above can be mitigated.

A.4 A Flexible Sidewall Pressure Sensor

In this section a new flexible sidewall approach is presented and compared with the traditional diaphragm design. The original design requirements for an implantable pressure sensor are high sensitivity and resolution, large dynamic range, low drift, biocompatible materials, and small in size. The threshold for intervention of a coronary artery is a 70-80% stenosis (narrowing). In order to sense a 60% stenosis, a pressure resolution of about 1 mmHg is needed [DeH04]. The target sensor drift should therefore either be less than 1 mmHg for the duration of the sensor measurements, or to drift in a controlled way that can be calibrated for.

The dynamic range for sensing pressure in the body is from 800 to 960 mmHg (106-128 kPa) where atmosphere is 760 mmHg (101 kPa). In order to cover this large range a compromise with sensitivity and linearity is often necessary. For higher sensitivity the dynamic range must be lower because the diaphragm material is typically made more flexible while the sense gap remains the same. Design tricks such as adding a boss, using multiple shaped diaphragms, and adjusting the residual stress can be used to tailor the sensor for a specific application. However, for implantable applications, size often cannot be compromised in order to improve performance without adverse biological effects.

The size requirements for an implantable coronary artery pressure sensor are around 1 mm x 1-2 mm x 100-150 μm. The sensor must be small enough to hug the wall of a 3 mm diameter artery and not disrupt the flow of blood. If blood flow is disturbed, there is a higher risk of thrombus (clot) formation. Stainless steel stent struts are typically 100-200 μm thick and so the sensor should not be much thicker. In addition, stents are delivered using catheter based balloon expansion. The device must small enough to be threaded from the femoral artery in the leg up to the coronary artery near the heart.

There has been an enormous amount of work done in the field of MEMS based pressure sensors. Capacitive pressure sensors scale more favorably than piezoresistive, can be connected to an inductor to form a passive wireless LC tank sensor, but are not as linear. The majority of capacitive pressure sensor designs use a flexible diaphragm top electrode that changes distance from a rigid bottom electrode and thus changes capacitance. The sensitivity of capacitive diaphragm pressure sensors is around 1000 ppm/mmHg and minimum resolution around 1 mmHg is common. The smaller the gap between the electrodes, the more sensitive it is, but the dynamic range and linearity are reduced.

Unfortunately as area is scaled down, the electrode spacing and diaphragm thickness must also be scaled down to maintain sensitivity. Fabrication and packaging are also much more challenging. A new flexible sidewall pressure sensor concept is investigated to see if better design tradeoffs can be made.

A.4.1 Sensor Design

Two rigid circular plates of radius *r* are supported by flexible parylene-C sidewalls of height *h* and thickness *t* (Fig. A-7). An incompressible fluid (silicone oil) translates pressure on the plates to the sidewalls (Fig A-8). Due to the larger area of the rigid plates compared to the area of the sidewalls, the internal pressure on the sidewalls from the fluid is much larger than the external pressure.

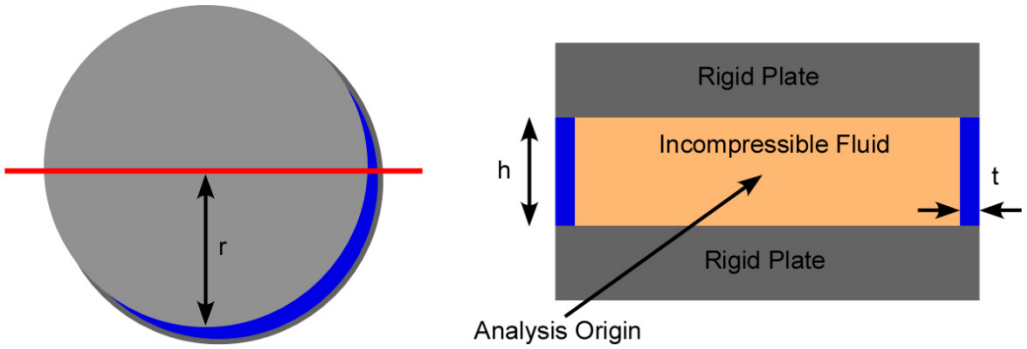

Fig. A-7: Construction of a flexible sidewall pressure sensor.

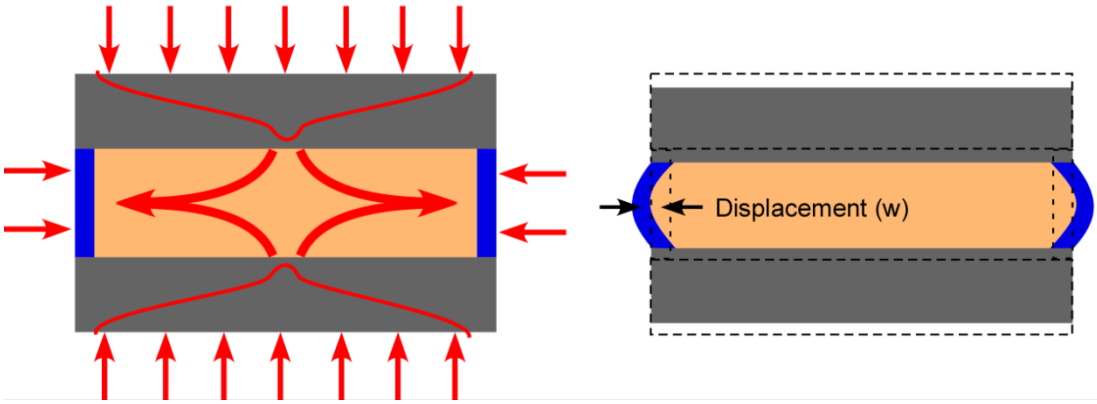

Fig. A-8: Operating mechanism of a flexible sidewall pressure sensor. Pressure is transferred from the rigid plates to the sidewalls by the fluid.

As pressure increases the sidewalls bow out. Since the fluid is incompressible the volume must remain constant. The rigid plates consequently become closer together and

the overall capacitance change is detected. Note that the fluid has a higher dielectric constant than air, increasing the sensitivity.

The proposed fabrication process is based around the finding in [Yos08] that parylene can be deposited directly on silicone oil which has a low vapor pressure. The oil is held in place by the surface tension of two rigid stainless steel plates. The space between is defined by kapton spacers. After the parylene deposition the support arms can be removed mechanically or with EDM. The arms can also form connections to an inductor antenna stent, eliminating the need for conductive epoxy or solder. The parylene serves not only as the mechanical purpose of translating pressure to deflection, but also provides electrical isolation of the electrodes from the environment.

Initially, the net pressure p exerted on the sidewall is found by converting the external applied pressure P_e to forces (F=PA) using the areas of the rigid plates A_p and the area of the sidewall A_s.

$$pA_s = 2P_eA_p - PA_s \qquad (A.1)$$

Substituting for the area, the pressure is put in terms of plate height h and radius r.

$$p = P_e(2\frac{A_p}{A_s} - 1) = P_e(\frac{2\pi r^2}{2\pi rh} - 1) = P_e(\frac{r}{h} - 1) \qquad (A.2)$$

As the radius of the plates increase and the plate height decreases, the force applied from the inside of the sidewall increases. The sidewall deflection profile is found from the shell theory for a pressurized cylinder [Gib65, Jaw04, Tim59].

The sidewall profile is plotted below in Fig. A-9 for a radius of 1 mm, sidewall thickness of 1 μm, and height of 80 μm. The figure on the left shows the profile for

several pressures from atmosphere to 960mmHg. The maximum deflection is about ½ the deformed gap spacing for a 200 mmHg pressure differential. The plot on the right shows how much the plates move vertically to maintain a constant volume for a given lateral sidewall deflection. The sidewall thickness has a large impact on the magnitude of deflection.

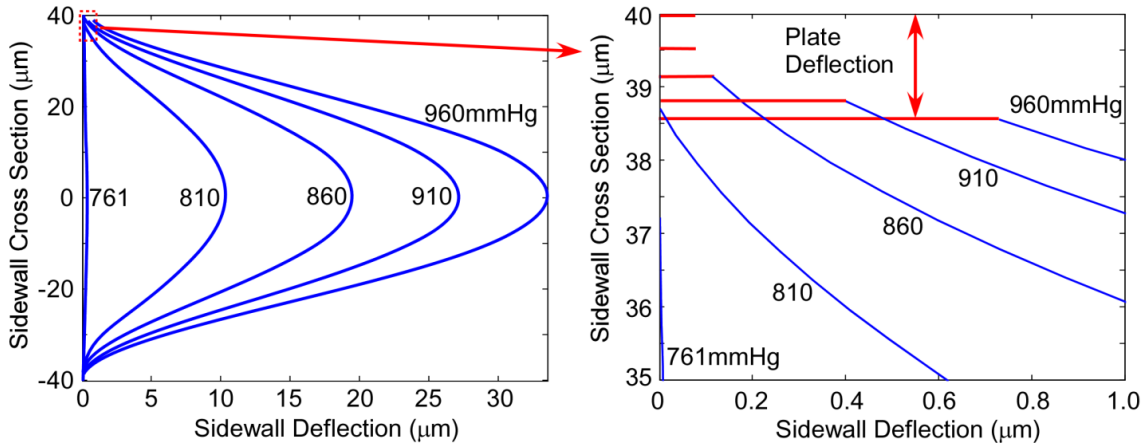

Fig. A-9: Sidewall deflection profile for increasing applied pressures. Right: corresponding vertical deflection of the rigid plates.

The rigid plate displacement is found using the fact that the fluid is incompressible. Since the volume must remain constant, dividing the sidewall volume displacement by the area of the plate (πr^2) gives the total displacement of the rigid plates *z*. Reasonable dimensions (r=1mm, t=1μm, h=80μm) give a sensitivity of 0.29 fF/mmHg or 1.25 ppm/mmHg normalized. Increasing the radius lowers the utility of the sensor for cardiovascular applications and decreasing the sidewall thickness makes the fabrication much more challenging. For a plate thickness of 50 μm, the total height of the sensor would be approximately 180μm.

The sensitivity of the sensor is defined in equation A.3 and normalized sensitivity is additionally divided by C_0. The following equations are needed to solve for the sensitivity:

$$\frac{dC}{dP} = \frac{dC}{dz}\frac{dz}{dP} \quad \text{where} \quad \frac{dC}{dz} = \frac{\varepsilon_r \varepsilon_0 \pi r^2}{(z-h)^2} \quad \text{and} \quad \frac{dz}{dP} = \frac{2}{r}\frac{dArea}{dP}$$

(A.3,A.4,A.5)

$$\frac{dArea}{dP} = \left[\frac{dA_1}{dP}(...) + \frac{dA_4}{dP}(...) - \left(\frac{dp}{dP}\frac{r^2}{Et}x \right) \right]_{-h/2}^{h/2} \quad \text{where}$$

$$\frac{dp}{dP} = \left(\frac{r}{2\sqrt{(h/2)^2 + (\frac{dA_4}{dP} - \frac{dp}{dP}\frac{r^2}{Et})^2}} - 1 \right)$$

(A.6,A.7)

$$\frac{dA_1}{dP_1} = \frac{dp}{dP}\frac{2r^2}{Et}\left[\frac{\sin\alpha\cosh\alpha - \cos\alpha\sinh\alpha}{\sin 2\alpha + \sinh 2\alpha} \right] \quad \text{and}$$

$$\frac{dA_4}{dP} = \frac{dp}{dP}\frac{2r^2}{Et}\left[\frac{\cos\alpha\cosh\alpha + \sin\alpha\cosh\alpha}{\sin 2\alpha + \sinh 2\alpha} \right]$$

(A.8,A.9)

$$A_1 = \frac{2pr^2}{Et}\left[\frac{\sin\alpha\cosh\alpha - \cos\alpha\sinh\alpha}{\sin 2\alpha + \sinh 2\alpha} \right] \text{ and } A_4 = \frac{2pr^2}{Et}\left[\frac{\cos\alpha\cosh\alpha + \sin\alpha\cosh\alpha}{\sin 2\alpha + \sinh 2\alpha} \right]$$

(A.10,A.11)

$$\alpha = \frac{\beta h}{2} \quad \text{and} \quad D = \frac{Et^3}{12(1-v^2)} \quad \text{and} \quad \beta^4 = \frac{Et}{4Dr^2} = \frac{3(1-v^2)}{r^2 t^2}$$

(A.12,A.13,A.14)

Where *E* is the young's modulus and υ is the poisson's ratio, r is the plate radius, h is plate separation, t is sidewall thickness, p is the pressure differential and P is external pressure.

The sensitivity of the sensor for varying dimensions is plotted in Fig. A-10. The sensitivity vs. plate spacing has an interesting trend. For small plate spacing the sidewalls are not flexible enough to displace large volumes and therefore achieve large vertical movement. However when the plates are further and further apart, the sensitivity eventually decreases because the capacitance has an inverse square trend with plate height. The maximum sensitivity at 80 μm can be moved left or right depending on the chosen radius and sidewall thickness. The sensitivity plots for sidewall thickness and plate radius behave as expected. As sidewall thickness decreases and plate radius increases, the sensitivity increases. All three sensitivity plots are interdependent.

The main advantage of the flexible sidewall design is the fabrication process is very simple compared to traditional bulk silicon micromachining. There is one critical step, parylene deposition. Another advantage of the flexible sidewall approach is that there is no sealed gas to worry about for thermal expansion. There will be some expansion of the silicone (~1.5×10^{-5}/K), but it is much less than air (3.2×10^{-3}/K). The sidewall design should also handle residual stress better than a traditional diaphragm approach.

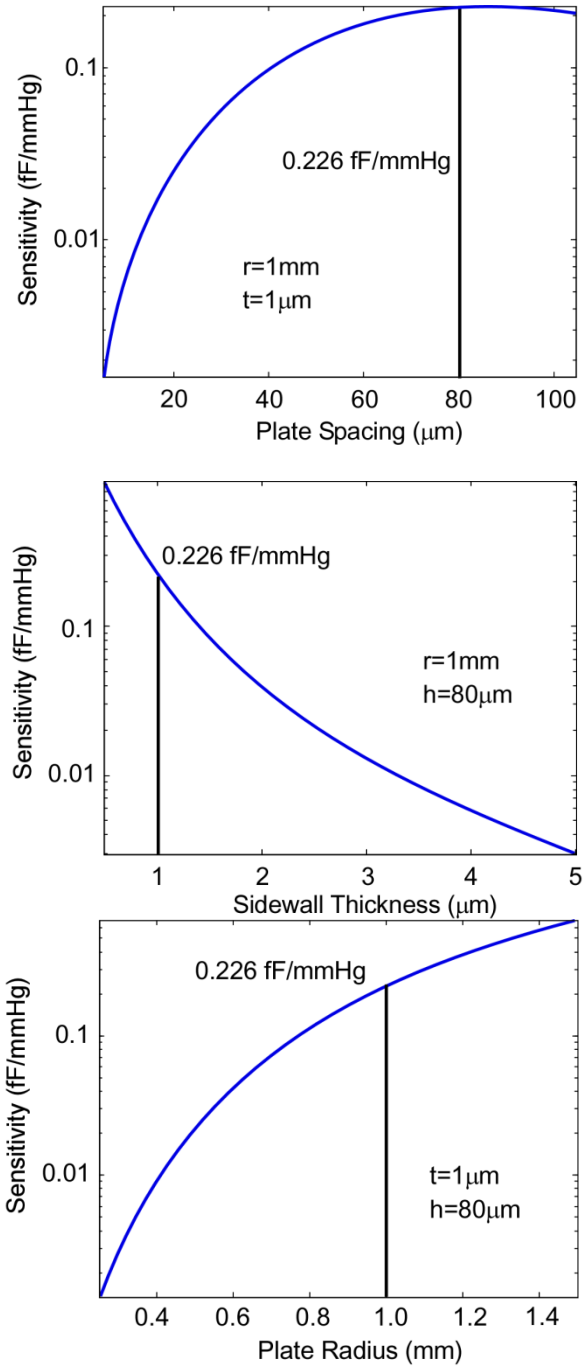

Fig. A-10: Top: Sensitivity vs. plate spacing (*h*) for fixed radius and thickness. There is a maximum point where increased flexibility is offset by decreasing change in capacitance. Bottom: As sidewall thickness decreases or radius increases, sensitivity increases.

A flexible sidewall diaphragmless pressure sensor was designed in an effort to address concerns with sensor drift and reliability upon deployment in an artery. While the

fabrication process is easier to integrate directly on a stent it was found that the approach did not have sufficient sensitivity and so fabrication was delayed until further study can be performed.

APPENDIX B

A #302 STAINLESS STEEL BI-STABLE RF SWITCH

The majority of MEMS RF switches utilize silicon wafer based thin film microfabrication, typically with gold contacts and electrostatic actuation. The advantage of this approach is the strong base of process technology and knowledge available. However, a thin film approach has limitations in lifetime, power handling capability, parasitic capacitance, and standoff voltage. Thin film electrostatic switches are more susceptible to corrosion effects because the switch closing force is much smaller than macro scale switches. It is also an additive approach, requiring meticulous process characterization to ensure consistent material properties. High aspect ratio technologies such as DRIE and LIGA also do not have a broad material selection.

An alternative approach is to use batch mode μEDM to fabricate an electrothermally actuated switch. Since μEDM is a subtractive process, the suite of material is expanded to alloys such as stainless steel, platinum-rhodium, and silicon carbide. The device thickness is also significantly increased compared to thin film deposition. In this work, a 25 μm thick bistable RF switch is fabricated from #302 stainless steel foil with 5 μm minimum features. This application is another potential high volume device which had a large pattern and requires high resolution.

The fabrication challenges encountered in this work motivated the parametric study and debris handling techniques presented in chapters 2 and 3.[1]

B.1 Switch Design

The design concept of the bistable electrothermal switch is shown in Fig. B-1 below. Two signal lines are connected at disconnected by a bi-stable structure in the middle. Two opposing electrothermal actuators control the position of the switch. The high throw and force of electrothermal actuators allow for larger stand-off voltage than a thin film approach. Since the switch is bi-stable there is no holding power necessary to keep the switch closed.

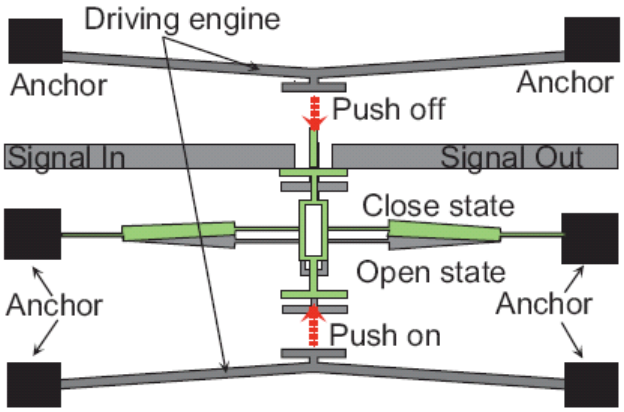

Fig. B-1: Bi-stable RF switch from [2] consists of two electro thermal actuators that flip the bi-stable structure in the middle, making or braking contact with the signal lines.

An analytical approximation of the force and displacement of a cosine shaped bi-stable structure of uniform width w, length l, and uniform thickness t can be found using the model from [Qiu04] shown in Fig. B-2. The f_{top} equation is the maximum force to change mode shapes and d_{mid} is the necessary displacement to reach the second stable

[1] Design and fabrication of the switch was by M. Richardson, L. Que, K. Udeshi, working under the guidance of Y.B. Gianchandani. RF analysis was by J.-J. Hung working under the guidance of G.M. Rebeiz [Que04,Ude05].

position. The other parameters are Young's modulus E, moment of inertia I and cosine shape amplitude h. These approximations allow us to consider the impact of different geometries. Figure B-3 from [Shi06] shows the force displacement curve for a typical electrothermal actuator.

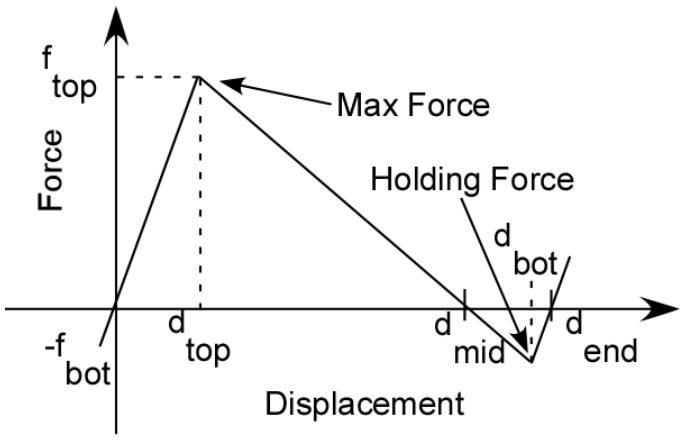

Fig. B-2: Force and displacement model of a cosine shaped bi-stable structure (adapted from [Qiu04]).

$$f_{\text{top}} \approx 740\frac{EIh}{l^3}, \quad f_{\text{bot}} \approx 370\frac{EIh}{l^3}, \quad d_{\text{mid}} = \frac{4}{3}h,$$

$$d_{\text{top}} \approx 0.16h, \quad d_{\text{bot}} \approx 1.92h, \quad d_{\text{end}} \approx 1.99h$$

where $I = \frac{t\,w^3}{12}$

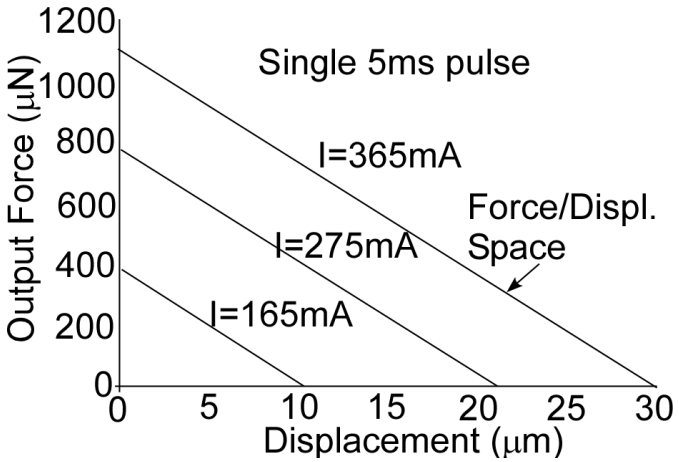

Fig. B-3: Force displacement curve for copper bent beam electrothermal actuator shows mN forces and 30μm displacements are readily achievable (adapted from [Shi06]). These values can be increased further through force displacement multiplication geometries.

For two parallel plates with linear spring constant, the pull-in voltage is reached at a displacement of 2/3 the starting gap. However, since the spring constant for this bi-stable structure is not linear, as seen in Fig. B-2, the pull-in voltage is the voltage needed to exceed f_{top} at a distance of g - d_{top} because the force decreases beyond that point. The equation for force from a voltage across two parallel plates [Sen02] can be rearranged to find the pull-in voltage. The geometry for the switch design is summarized in Fig. B-4.

$$V_{pull\ in} = \sqrt{\frac{2F_{top}{d_{top}}^2}{\varepsilon A}} \qquad \text{(B.1)}$$

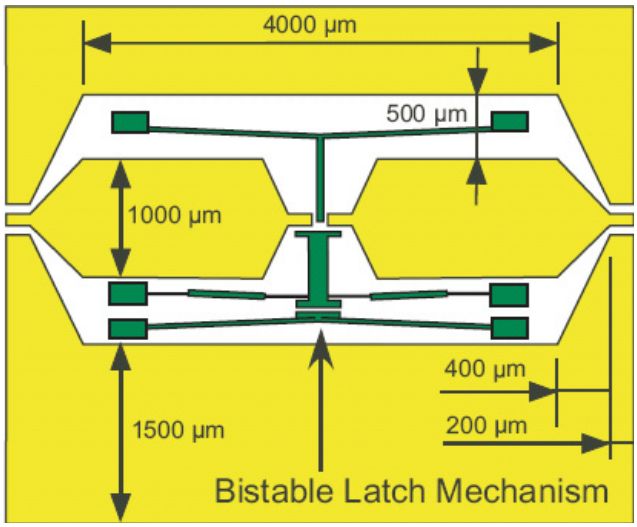

Fig. B-4: Schematic of the RF switch with dimensions of the waveguide.

B.2 Fabrication

Commercial electromechanical switches use thin film additive processes for the deposition of the contact material. Chemical vapor deposition is difficult because of the stoichiometry dependence. Coevaporation is difficult to control because of straight line evaporation patterns [Cou04, Cou06]. Sputtering has better coverage but still difficult to

control and has deposition thickness limitations. Electroplating in a LIGA type process has limited material selection. The difficulty with additive processes in general is that controlling material properties, and therefore reliability, is a significant burden. Commercial switches deposit a few microns of material at most with a thicker mechanical structure layer. For a high power switch, large amounts of material are needed to handle the high electrical current loads and thermal loads. Using one material and using a subtractive process ensures better repeatability of material properties and does not have a material interface that could present problems [Ude07].

Microfabrication with thick (>5um) alloys requires using a subtractive process such as batch μEDM from bulk metal stock. Batch μEDM offers high throughput at relatively good precision but machining thick high aspect ratio features is very difficult as feature widths decrease. The parametric study of batch mode μEDM in Chp. 2 showed that tool wear becomes significant in tool features smaller than 10 μm due to debris accumulation. However, debris mitigation techniques such as bubble assisted flushing and a tool passivation coating can lessen the impact. Since this work was done before that study, the machining depth was limited to 25 μm at which point the 5 μm minimum features began to degrade.

The reverse damascene process developed in [Ude06] was used to fabricate the switch as shown in Fig. B-5. Copper tools were fabricated using a UV-LIGA process with 100 μm height as described in chapter 1 and [Ude06]. The two tools were aligned to the stage x-axis, clamped in place with the jig in Fig. B-6, and their distances from each other were recorded. Stainless steel workpieces were cut to 1 cm x 1.2 cm pieces from #302 shim stock and burrs removed by polishing with sandpaper. The steel was attached

to a wire-EDM leveled aluminum mandrel by silver epoxy with uniform clamping pressure. The workpiece was machined first to 8μm with a shallow copper tool and then translated to the measured distance of the second deeper tool.

After machining, the gaps were filled with cyanoacrylate and lapped planar so that the features would survive the subsequent lapping steps (steps 3,4). The lapped surface is then epoxy bonded to a glass slide and lapped to expose the structure (steps 5,6). Finally, the cyanoacrylate is dissolved in acetone to release the switch structure.

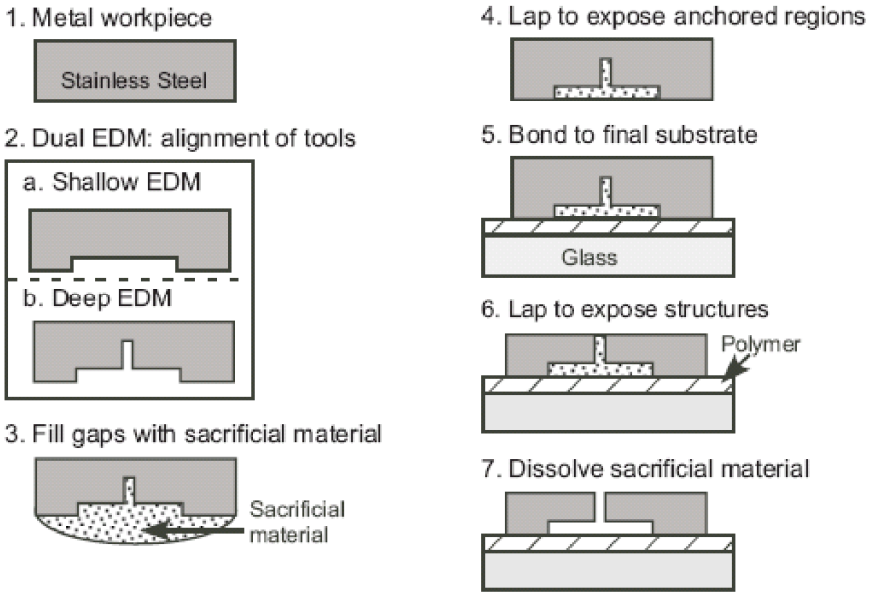

Fig. B-5: Reverse Damascene process used for fabricating the bistable RF switch in #302 stainless steel. Two aligned batch μEDM steps were used to create suspended structures.

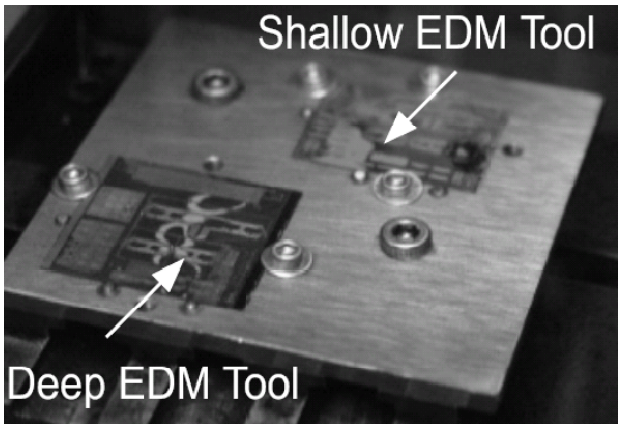

Fig. B-6: Jig for alignment of the two EDM steps.

B.3 Results

The fabrication results for the bi-stable single-pole-single-throw (SPST) RF switch for a coplanar waveguide are shown below. An SEM image of the copper tool is shown in Fig. B-7. It is the reverse image of the finished stainless steel device shown in Fig. B-8. The copper tools had minimum feature sizes of 10 μm for an aspect ratio of 10:1. The minimum feature of the bi-stable structure was a 5 μm beam in the bi-stable structure. The minimum machined trench is the width of the tool plus two 5 μm discharge gaps, which is adds up to about 20 μm. Structures less than 25 μm tall are challenging due to shearing during the final lapping step.

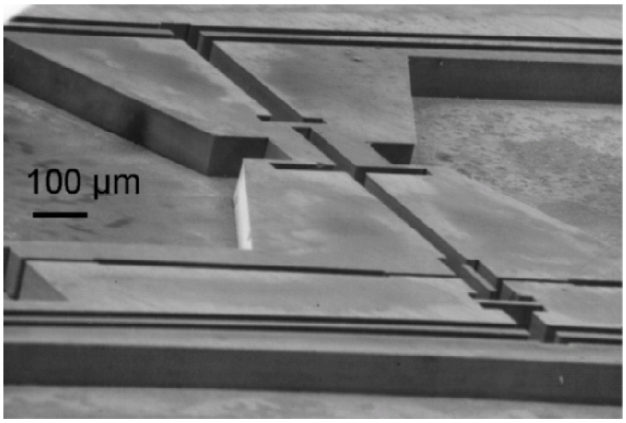

Fig. B-7: Copper tool fabricated with a UV-LIGA process to 100 μm height and 10 μm minimum features.

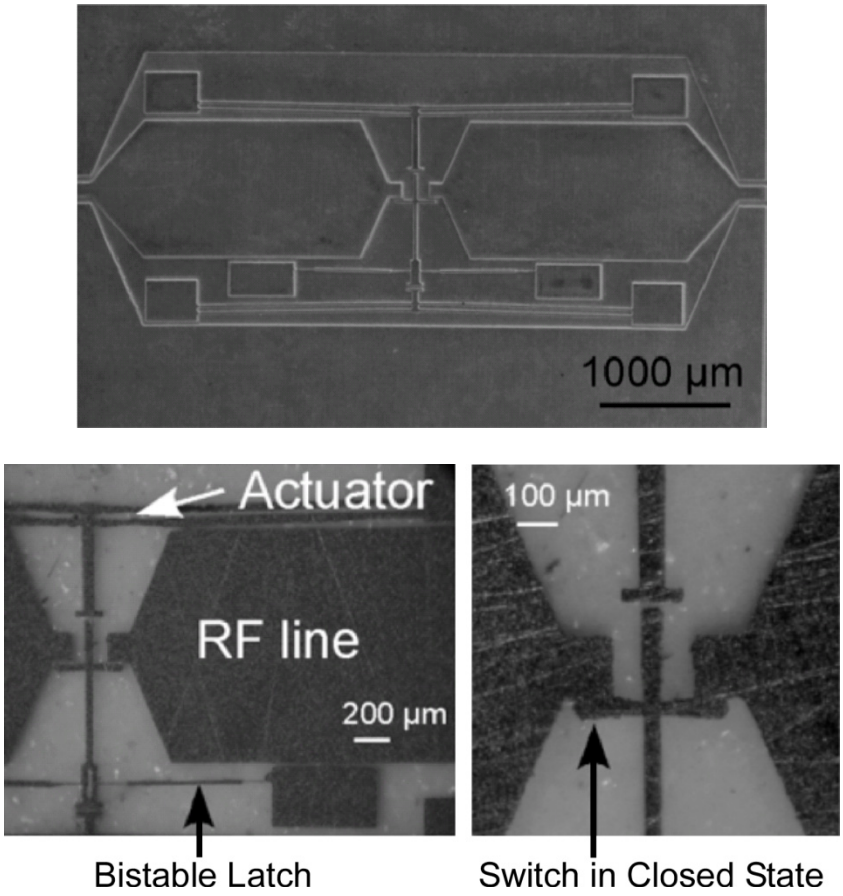

Fig. B-8: Finished #302 stainless steel bi-stable SPST RF switch.

The RF performance results of the switch are shown in Figs. B-9 to B-11. The design was simulated in SONNET and compared to measured results for isolation, insertion loss and return loss. The insertion loss is 0.7 dB at 2 GHz and could be due to the oxide on the surface of the stainless steel. The isolation is better than -30 dB at 2Ghz and the return loss is less than -10 dB from DC to 4 GHz.

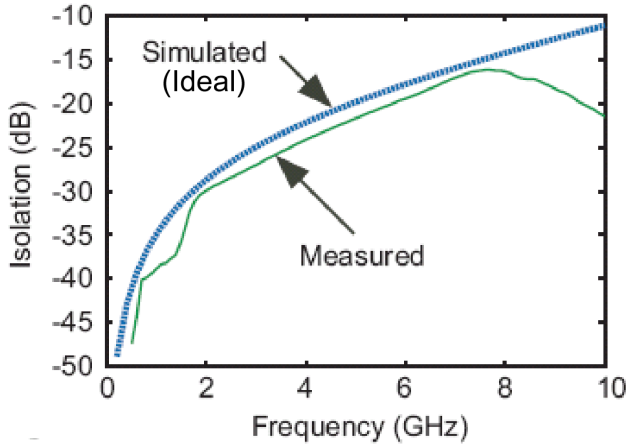

Fig. B-9: Isolation measurement for fabricated switch

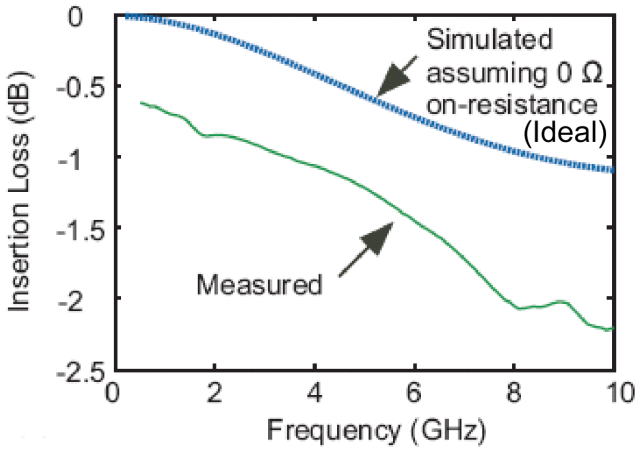

Fig. B-10: Insertion loss for fabricated switch

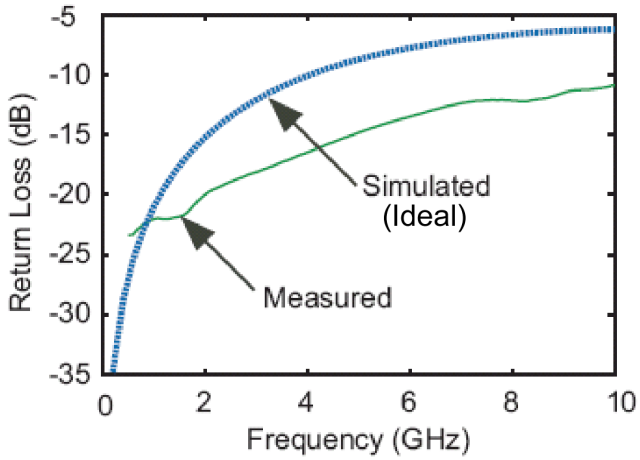

Fig. B-11: Return loss for fabricated switch

The understanding gained through the studies conducted in this research should enable higher machining performance for future designs. For example, by incorporating the debris handling techniques in chapter 3 and the tool wear information from chapter 2, higher fidelity switch designs will be possible.

REFERENCES

[Aim04] M. Aimi, M.P. Rao, N. MacDonald, A.S. Zuruzi, D.P. Bothman, "High-aspect-ratio bulk micromachining of titanium," Nature Materials, vol. 3, pp. 103-105, Feb. 2004.

[Akk09] A. Akkurt, "The effect of material type and plate thickness on drilling time of abrasive water jet drilling process," *Materials & Design*, vol. 30(3), pp. 810-815, 2009.

[Al-M04] N. Al-Mubarak, G.S. Roubin, S.S. Iyer, J.J. Vitek, Carotid artery stenting: Current Practice and Technique, Lippincott Williams and Wilkins, Philadelphia, 2004.

[Alb96] K. Albinksi, K. Musiol, A. Miernikiewicz, S. Labuz, M. Malota, "The temperature of a plasma used in electrical discharge machining," *Plasma Sources Sci. Tech*., Vol. 5, pp. 736-742, 1996.

[Amor04] F.L. Amorim, W.L. Weingaertner, "Die-sinking electrical discharge machining, of a high-strength copper-based alloy for injection molds," *J. of the Braz. Soc. Of Mech . Sci. & Eng*, Vol. XXVI, No. 2, pp. 137-144, 2004.

[Aoy99] S. Aoyama, K. Tamura, T. Sato, T. Kimura, K. Sawahata, T. Nagai, "High-performance coated wire electrodes for high-speed cutting and accurate machining," *Hitachi Cable Review*, 18, pp. 75-80, Oct. 1999.

[Berg07] R. Berg, J. Aragon, V. Royter, J.F. Shanley, G. Cogert, R. Vermani, S. Kar, N. Eigler, F. Litvack, "Pimecrolimus and dual pimecrolimus-paclitaxel eluting stents decrease neointimal proliferation in a porcine model," *Catheterization and Cardiovascular Interventions*, vol. 70, pp. 871-879, 2007.

[Bev94] H. Beving, L.E.G. Eriksson, C.L. Davey, D.B. Kell, " Dielectric properties of human blood and erythrocytes at radio frequencies (0.2–10 MHz); dependence on cell volume fraction and medium composition," *Eur. Biophys. J*, vol. 23, pp. 207-215, 1994.

[Bhat78] S.K. Bhattacharya and M.F. El-Menshawy, "Monitoring the E.D.M. process by radio signals," International Journal of Production Research, v16,5, pp. 353-363, 1978.

[Bhat80] S.K. Bhattacharyya, M.F. El-Menshawy, "Monitoring and controlling the E.D.M. process," *J. Engineering for Industry*, vol. 102, pp. 189-194, Aug. 1980.

[Bhu05] A. Bhuyan, B. Gregory, H. Lei, S.Y. Yee, Y.B. Gianchandani, "Pulse and DC electropolishing of stainless steel for stents and other devices," *Proc. of IEEE Sensors*, pp. 314-317, 2005.

[Bok02] B. Bokhonov, M. Korchagin, "In-situ investigation of the formation of eutectic alloys in the systems silicon-silver and silicon-copper," *J. Alloys and Compounds*, 335(1-2), pp. 149-156, 2002.

[Brig02] C. Briguouri, C. Sarais, P. Pagnotta, F. Liistro, M. Montorfano, A. Chieffo, F. Sgura, N. Corvaja, R. Albiero, G. Stankovic, C. Toutoutzas, E. Bonizzoni, C. Di Mario, A. Colombo, "In-stent restenosis in small coronary arteries: impact of strut thickness," *J. of American College of Cardiology*, vol. 40(3), pp. 403-409, 13-21, 2002.

[Bron87] L. Bronson, Textbook of cardiovascular technology, J.B. Lippincott Company, Philadelphia, 1987.

[Bro98] J. Brown, Advanced Machining Technology Handbook, McGraw Hill, 1998.

[Brz07] J. Brzezinski, G. Oszkinis, E. Marzee, "Dielectric relaxation of a protein–water system in atherosclerotic artery wall," *Med. Bio. Eng. Comput.*, vol. 45, pp. 525-529, 2007.

[Cab08] I. Cabanes, E. Portillo, M. Marcos, J.A. Sanchez, "An industrial application for on-line detection of instability and wire breakage in wire EDM," *J. Materials Processing Technology*, vol. 195, pp. 101-109, 2008.

[Cam07] E. Camenzind, P.G. Steg, W. Wijns, "Stent thrombosis late after implantation of first-generation drug-eluting stents: a cause for concern," *Circulation J. Amer. Heart Assoc*., 115, pp. 1440-1455, 2007.

[Cap05] C. Capaccio, N. Stoykov, F. Cortes, A. Gutierrerz, R. Sundararajan, D.A. Dean, "Parametric analysis of electric field distribution of rat vasculature using finite element time domain technique," *Proc. COMSOL Users Conf.*, Boston, 2005.

[Chan02] S-P. Chang, J-B. Lee, M.G. Allen, "Robust capacitive pressure sensor array," *Sensors and Actuators A*, 101, pp. 231-238, 2002.

[Chap02] W. Chapman, Modern Machine Shop's Handbook for the Metalworking Industries, Hanser Gardner, 2002.

[Chau87] H-L Chau, An ultraminiature solid-state pressure sensor for a cardiovascular catheter, Ph.D. Dissertation, University of Michigan, 1987.

[Chau88] H. Chau, K.D. Wise, "Scaling limits in batch-fabricated silicon pressure sensors," *IEEE Trans. on Electron Devices*, 35(12), Dec. 1988, pp. 2355-2362.

[Chav00] A.V. Chavan, An integrated high resolution barometric pressure sensing system, Ph.D. Dissertation, University of Michigan, 2000.

[Che05] X.H. Chen, J. Lu, L. Lu, K. Lu, "Tensile properties of a nanocrystalline 316L austenitic stainless steel," *Scripta Materialia*, vol. 52(10), pp. 1039-1044, 2005.

[Cho05] S. Cho, H. Thielecke, "Design of electrode array for impedance measurement of lesions in arteries," *Physiol. Meas*. vol. 26, pp. S19-S26, 2005.

[Cla79] S.K. Clark, K.D. Wise, "Pressure sensitivity in anisotropically etched thin-diaphragm pressure sensors," *IEEE Transactions on Electron Devices*, 26(12), Dec. 1979, pp. 1887-1896.

[Col02] A. Colombo, G. Stankovic, J.W. Moses, "Selection of coronary stents," *J. of Amer. Coll. Of Cardiology*, 40(6), pp. 1021-1033, 2002.

[Col06] A. Colombo, S.J. Corbett, "Drug-eluting stent thrombosis increasingly recognized but too frequently overemphasized," *J. Amer. Col. Of Card*. 48(1), pp. 203-205, Jul. 2006.

[Cou04] R.A. Coutu, P.E. Kladitis, K.D. Leedy, R.L. Crane, "Selecting metal alloy electric contact materials for MEMS switches," *J. Micromech. Microeng.* vol. 14, pp. 1157-1164, 2004.

[Cou06] H. Lee, R.A Coutu, S. mall, K.D. Leedy, "Characterization of metal and metal alloy films as contact materials in MEMS switches," *J. Micromech. Microeng.* vol. 16, pp. 557-563, 2006.

[DeLu03] G. De Luca, H. Suryapranata, F. Zijlstra, A.W.J. van't Hof, J.C.A. Hoorntje, A.T.M. Gosselink, J-H. Dambrink, M-J. de Boer, "Symptom-onset-to-balloon time and mortality in patients with acute myocardial infarction treated by primary angioplasty," J. Am. Coll. Cardiol, vol. 42, pp.991-997, 2003.

[Desc06] A. Descoeudres, Characterization of Electrical Discharge Machining Plasmas, Ph.D. Dissertation, EPFL, 2006.

[DeH04] A. DeHennis, *Remotely-Powered Wireless Monitoring Systems*, PhD Dissertation, University of Michigan, 2004.

[Dha05] S. Dhanik, S.S. Joshi, "Modeling of a single resistance capacitance pulse discharge in micro-electro-discharge machining," J. Manufacturing Science and Engineering, vol. 127, pp. 759-767, 2005.

[Eba99] Y. Ebara, T. Koizumi, H. Sone, Y. Nemoto, "Experiments on Relationship between Electromagnetic Noise and Surface Profile Change by Arc Discharge of Heterogenous Material Contacts," *IEEE Electromagnetic Compatibility Symposium*, pp. 165-170 1999.

[Eba00] Y. Ebara, H. Sone, Y. Nemoto, "Correlation between arcing phenomena and electromagnetic noise of opening electric contacts," *Proc. of IEEE Electrical Contacts,* pp. 191-197, 2000.

[Ehr96] W. Ehrfeld, H. Lehr, F. Michel, and A. Wolf, "Microelectro Discharge Machining as a Technology in Micromachining," SPIE's Symp. Micromachining and Microfabrication, v. 2879, pp. 332–337, 1996.

[Eis64] S. Eisenberg, M. Horn, N. Nelson, "Changes in blood viscosity, hematocrit value, and fibrinogen concentration in subjects with congestive heart failure," *Circulation*, vol. 30, pp. 686-693, 1964.

[Ekme06] B. Ekmekci, A.E. Tekkaya, A. Erden, "A semi-empirical approach for residual stresses in electric discharge machining (EDM)," *International J. of Machine Tools & Manufacture*, vol. 46, pp. 858-868, 2006.

[Ekme07] B. Ekmekci, "Residual stresses and white layer in electric discharge machining (EDM)," *Applied Surface Science*, vol. 253, pp. 9234-9240, 2007.

[El-Ho05] H. El-Hofy, Advanced Machining Processes: Nontraditional and Hybrid Machining Processes, McGraw Hill, 2005.

[Ell06] S.G. Ellis, D.R. Holmes Jr., Strategic approaches in coronary intervention, 3rd ed., Lippincott Williams and Wilkins, Philadelphia 2006.

[Eun08] C.K. Eun, Y.B. Gianchandani, "Exploring RF transmissions from discharge-based micromachined radiation detectors," *Proc. of IEEE Conf. on Technologies for Homeland Security*, pp. 18-23, May 2008.

[Fall93] M.A. Fallert, M.S. Mirotznik, S.W. Downing, E.B. Savage, K.R. Foster, M.E. Josephson, D.K. Bogen, "Myocardial electrical impedance mapping of ischemic sheep hearts and healing aneurysms," *Circulation*, vol. 87, pp. 199-207, 1993.

[Fax02] D.P. Faxon, Restenosis: A guide to therapy, Martin Dunitz, London, 2001.

[Fon06] M.A. Fonseca, M.G. Allen, J. Kroh, J. White, "Flexible wireless passive pressure sensors for biomedical applications," *Solid State Sensors and Actuators Workshop Hilton Head 2006,* pp. 37-42.

[Fri96] C.R. Friedrich, M.J. Vasile, "Development of the micromilling process for high-aspect-ratio microstructures," J. MEMS, 5(1), Mar. 1996.

[Fuj03] O. Fujiwara, K. Okuda, K. Fukunaga, Y. Yamanaka, "FDTD computation of electromagnetic fields caused by electrostatic discharge between charged metal spheres," *Electronics and Communications in Japan*, Part 1, vol. 86(7), pp. 54-63, 2003.

[Gab96-1] C. Gabriel, S. Gabriel, E. Corthout, "The dielectric properties of biological tissues: I. Literature survey" *Phys. Med. Biol.*, vol. 41, pp. 2231-2249, 1996.

[Gab96-2] S. Gabriel, R.W. Lau, C. Gabriel, "The dielectric properties of biological tissues: II Measurements in the frequency range 10 Hz to 20 GHz," *Phys. Med. Biol.*, vol. 41, pp. 2251-2269, 1996.

[Gab96-3] S. Gabriel, R.W. Lau, C. Gabriel, "The dielectric properties of biological tissues: III. Parametric models for the dielectric spectrum of tissues," *Phys. Med. Biol.*, vol. 41, pp. 2271-2293, 1996.

[Gabr93] T.B. Gabrielson, "Mechanical-thermal noise in micromachined acoustic and vibration sensors," *IEEE Transactions on Electron Devices*, 40(5), Mar. 1993, pp. 903-909.

[Gao03] C. Gao, Z. Liu, "A study of ultrasonically aided micro-electrical-discharge machining by the application of workpiece vibration," *J. Materials Proc. Tech*, 139, pp. 226-228, 2003.

[Gaw07-1] R.L. Gaw, B.H. Cornish, B.J. Thomas, "Comparison of a theoretical impedance model with experimental measurements of pulsatile blood flow," *Proc. of IFMBE*, vol. 17, pp. 32-35, 2007.

[Gaw07-2] R.L. Gaw, B.H. Cornish, B.J. Thomas, "The electrical impedance of pulsatile blood flowing through rigid tubes- an experimental investigation," *Proc. of IFMBE ICEBI*, vol. 17, pp. 73-76, 2007.

[Gaw08] R.L. Gaw, B.H. Cornish, B.J. Thomas, "The electrical impedance of pulsatile blood flowing through rigid tubes: a theoretical investigation," *IEEE Trans. on Biomed. Engin.*, vol. 55(2), pp. 721-727, Feb. 2008.

[Gib65] J.E. Gibson, Linear Elastic Theory of Thin Shells, *Pergamon Press*, London, 1965.

[Grea98] W.D. Greason, Z. Kucerovsky, M.W. Flatley, S. Bulach, "Non-invasive measurement of electrostatic discharge induced phenomena in electronic systems," *IEEE Trans. on Industry Applications,* vol. 34(3), pp. 571-579, 1998.

[Gre07] S.R. Green, M.T. Richardson, F.A. Shariff, Y.B. Gianchandani, "Photochemically, patterned biliary stents with integrated permanent magnets and deformable assembly features for wireless Magnetoelastic tissue growth sensing," *Proc. of IEEE Transducers2007*, pp. 213-217, 2007.

[Gia89] C. Gianturco, "Endovascular stent and delivery system," US Patent #4,800,882, Jan. 1989.

[Gha03] F. Ghanem, C. Braham, H. Sidhom, "Influence of steel type on electrical discharge machined surface integrity," *J. of Materials Processing Technology*, vol. 142, pp. 163-173, 2003.

[Han06] F. Han, Y. Yamada, T. Kawakami, M. Kunieda, "Experimental attempts of sub-micrometer order size machining using micro-EDM," *Precision Engineering*, vol. 30, pp. 123-131, 2006.

[Hirs50] F.G. Hirsch, E.C. Texter, L.A. Wood, W.C. Ballard, F.E. Horan, I.S. Wright, C. Frey, D.Starr, "The electrical conductivity of blood: I. relationship to erythrocyte concentration," *Blood*, vol. 5, pp. 1017-1035, 1950.

[Ho03] K.H. Ho, S.T. Newman, "State of the art electrical discharge machining (EDM)," *Int. J. of Machine Tools & Manufacture*, 43, pp. 1287-1300, 2003.

[Hoe04] A.E. Hoetink, Th.J.C. Faes, K.R. Visser, R.M. Hethaar, "On the flow dependency of electrical conductivity of blood," *IEEE Trans. on Biomed. Engin.*, vol. 51(7), pp. 1251-1261, Jul. 2004.

[Hu80] C. Hu, W.F. Ki, "Toward a Practical Computer-Aid for Thyristor Circuit Design," *Proc. IEEE Power Electro. Special. Conf. (PESC)*, pp. 174-179, 1980

[Hua04] C. Huang, Y.Y. Lin, T.A. Tang, "Study on the tip-deflection of a piezoelectric bimorph cantilever in the static state," *J. Micromech. Microeng.*, vol. 14, pp. 530-534, 2004.

[Ishi96] S. Ishigami, T. Iwasaki, "Evaluation of charge transition in a small gap discharge," *IEICE Trans. Commun,* 79B(4), pp. 474-82 Apr. 1996.

[Jam01] E.C. Jameson, Electrical Discharge Machining, Society of Manufacturing Engineers, 2001.

[Jan08] G.C.A.M. Janssen, M.M. Abdalla, F. van Keulen, B.R. Pujada, B. van Venrooy, "Celebrating the 100th anniversary of the Stoney equation for film stress: Developments from polycrystalline steel strips to single crystal silicon wafers," *Thin Solid Films*, doi: 10.1016/j.tsf.2008.07014, pg. 1-10, July 2008.

[Jasp03] F. Jaspard, M. Nadi, A. Rouane, "Dielectric properties of blood: an investigation of haematocrit dependence," *Physiological Measurement*, vol. 24, pp. 137-147, 2003.

[Jaw04] M.H. Jawad, Design of plate and shell structures, *American Society of Mechanical Engineers*, New York, 2004.

[Jon06] M. Joner, A.V. Finn, A. Farb, E.K. Mont, F.D. Kolodgie, E. Ladich, R. Kutys, K. Skorija, H.K. Gold, and R. Virmani, "Pathology of Drug-Eluting Stents in Humans: Delayed Healing and Late Thrombotic Risk," J. Am. Coll. Cardiol, vol 48(1), pp. 193-202, Jul 2006.

[Kad91] A. Kadish, W. B. Maier, "Electromagnetic radiation from abrupt current changes in electrical discharges," *J. Appl. Phys.* 70(11), pp. 6700-11, Dec. 1, 1991.

[Kan97] T. Kaneko, M. Tsuchiya, "Observation of behavior of machining products in die-sinking EDM by using high-speed VTR," *Int. J. Electrical Machining*, No. 2, pp. 37-42, 1997.

[Kan00] Y. Kaneko, H. Yamada, T. Toyonaga, K. Shoda, "Performance of linear motor equipped die-sinking EDM," *Int. J. of Machine Tools & Manufacture*, 5, pp. 59-64, 2000.

[Kang98] I-H. Kang, O. Fujiwara, C-B. Lee, "Spectrum distribution of electromagnetic field radiated by electrostatic discharge on the ground screen," *Int. Symp. on Electromagnetic Compatibility*, vol. 2, pp. 994-998, 1998.

[Kao04] Y.L Kao, G.C. Tu, C.A. Huang, J.H. Chang, "The annealing behaviour of copper deposit electroplated in sulfuric acid bath with various concentrations of thiourea," Mat. Sci. and Engin. A, 382(1-2), pp. 104-111, 2004.

[Kao07] C-C. Kao, *Monitoring and Control of Micro-Hole Electrical Discharge Machining*, University of Michigan, Ph.D. Dissertation, 2007.

[Kao08] C-C. Kao, A.J. Shih, S.F. Miller, "Fuzzy logic control of microhole electrical discharge machining," *J. Manufacturing Science Engineering*, vol. 130(6), pp. 064502:1-6, 2008.

[Kar08] F.B. Karp, N.A. Bernotski, T.I. Valdes, K.F. Bohringer, B.D. Ratner, "Foreign body response investigated with an impanted biosensor by in situ electrical impedance spectroscopy," *Sensors Journal*, vol. 8(1), pp. 104-112, 2008.

[Kas00] A. Kastrati, A. Schomig, J. Dirschinger, J. Mehilli, N. von Welser, J. Pache, H. Schuhlen, T. Schilling, C. Schmitt, F-J. Neumann, "Increased risk of restenosis after placement of gold-coated stents," *Circulation*, v. 101, pp. 2478-2483, 2000.

[Kas01] A. Kastrati, J. Mehilli, J. Dirschinger, F. Dotzer, H. Schuhlen, F-J. Neumann, M. Fleckenstain, C. Pfafferott, M. Seyfarth, A. Schomig, "Intracoronary stenting and angiographic results: strut thickness effect on restenosis outcome (ISAR-STEREO) trial," *Circulation*, v.103, pp. 2816-2821, 2001.

[Kim06] D.J. Kim, S.M. Yi, Y.S. Lee, C.N. Chu, "Straight hole micro EDM with a cylindrical tool using a variable capacitance method accompanied by ultrasonic vibration," *J. Micromechanics and Microengineering*, vol. 16, pp. 1092-1097, 2006.

[Klo89] B. Kloeck, S.D. Collins, N.F de Rooij, R.L. Smith, "Study of electrochemical etch-stop for high-precision thickness control of silicon membranes," *IEEE Trans. on Elec. Dev.*, 36(4) II, pp.663-9 1989.

[Koch00] O. Koch, W. Ehrfeld, F. Michel, "Micro-Electro Discharge Machining - Application, Strategy and Technology," *Proc. 2nd Int'l. Workshop Microfactories (IWMF)*, pp. 79-82, 2000

[Korn98] R. Kornowski, M.K. Hong, F.O. Tio, O. Bramwell, H. Wu, M.B. Leon, "In-stent restenosis: contributions of inflammatory responses and arterial injury to neointimal hyperplasia," *J. of American College of Cardiology*, vol. 31(1), pp. 224-230, 1998.

[Kum03] S. Kumagai, N. Misawa, K. Takeda, E.T. Abdukarimov, "Plasma-applied machining of a narrow and deep hole in a metal using a dielectric-encased wire electrode," *Thin Solid Films*, 457(1), pp. 180-185, 2003.

[Kur08] W. Kurnia, P.C. Tan, S.H. Yeo, M. Wong, "Analytical approximation of the erosion rate and electrode wear in micro electrical discharge machining," *J. Micromech. Microeng.*, vol. 18, pp. 1-8, 2008.

[LaD05] J.F. Ladisa, L.E. Olson, R.C. Molthen, D.A. Hettrick, P.F. Pratt, M.D. Hardel, J.R. Kerten, D.C. Warltier, P.S. Pagel, "Alterations in wall shear stress predict sites of neointimal hyperplasia after stent implantation in rabbit iliac arteries," *Am. J. Physiol. Heart Circ. Physiol.* 288: H2465-H2475, 2005.

[Lew03] T.J. Lewis, “Breakdown initiating mechanisms at electrode interfaces in liquids,” *IEEE Trans. on Dielectrics and Electrical Insulation,* 10(6), Dec. 2003.

[Lia08] Y.S. Liao, T.Y. Chang, T.J. Chuang, “An on-line monitoring system for a micro electrical discharge machining (micro-EDM) process,” *J. Micromech. Microeng.*, vol. 18, pp. 1-8, 2008.

[Lim03] H.S. Lim, Y.S. Wong, M. Rahman, M.K. Edwin Lee, “A study on the machining of high-aspect ratio micro-structures using micro-EDM,” *J. of Materials Proc. Tech*., 140, pp. 318-325, 2003.

[Liu97] H.S. Liu, Y.S. Tarng, “Monitoring of the electrical discharge machining process by abductive networks,” *Int. J. Advanced Manufacturing Technology*, vol 13, pp. 264-270, 1997.

[Mark99] G. H. Markx, C.L. Davey, “The dielectric properties of biological cells at radiofrequencies- applications in biotechnology,” *Enzyme and Microbial Tech.*, vol. 25, pp. 161-171, 1999.

[Mas90] T. Masaki, K. Kawata, and T. Masuzawa, “Micro electro-discharge machining and its applications,” *IEEE MEMS 1990*, pp. 21-26, 1990.

[Masu85] T. Masuzawa, M. Fujino, K. Kobayashi, T. Suzuki, “Wire electro-discharge grinding for micromachining.” *CIRP Annals*, 34(1), pp. 431-434, 1985.

[McGe88] J.A. McGeough, Advanced Methods of Machining. New York: Chapman and Hall, 1988, pp. 128-152.

[McGe02] J. McGeough, Micromachining of Engineering Materials, New York: Marcel Dekker, 2002, pp. 179-201.

[Mean03] P.M. Meaney, M.M. Doyley, S.A. Pendergrass, W.A. Wells, S. Yan, C.J. Fox, K.D. Paulsen, “Microwave, intravascular detection of vulnerable plaque,” *Proc. of IEEE EMBS*, vol. 25, pp. 3783-3786, 2003.

[Mik06] D. Miklavcic, N. Pavselj, F.X. Hart, “Electric properties of tissues,” Wiley Encyclopedia of Biomedical Engineering, pp. 1-12, 2006.

[Mok07] W. Mokwa, “Medical implants based on microsystems,” *Meas. Sci. Technol.*, 18, pp. R47-R57, 2007.

[Mor01] W.E. Morf, O.T. Guenat, N.F. de Rooij, “ Electroosmotic pumping in complex capillary systems Part 1: Principles and general theorectical approach,” *Sensors and Actuators B*, 72, pp. 266-272, 2001.

[Mur70] E.J. Murphy, "The generation of gases in the dielectric breakdown of oil," *J. Phys. D: Appl. Phys*., vol. 3, pp. 917-923, 1970.

[Nai99] G.V. Naidis, "Simulation of streamer-to-spark transition in short non-uniform air gaps," J. Phys. D: Appl. Phys. Vol 32, pp. 2659-2654, 1999.

[Naj04] N. Najafi, A. Ludomirsky, "Initial animal studies of a wireless, batteryless, MEMS implant for cardiovascular applications," *Biomedical Microdevices*, 6(1), pp. 61-65, Mar. 2004.

[Newb86] R.S. Newbower, E.D. Trautman, "Sensor for catheter-based measurements of electrical conductivity," *IEEE Trans. on Biomed. Engin.*, vol. 33(2), pp. 182-188, Feb. 1986.

[Pal04] J. Palmaz, "Intravascular stents in the last and next 10 years," *J. Endovasc. Ther.*, 11(Suppl II), pp. 200-206, 2004.

[Park05] E.R. Parker, B.J. Thibeault, M.F. Aimi, M.P. Rao, N.C. MacDonald, "Inductively coupled plasma etching of bulk titanium for MEMS applications," J. Electrochem. Soc., vol. 152 (10), pp. C675-C683, 2005.

[Peth84] R. Pethig, "Dielectric properties of biological materials: biophysical and medical applications," *IEEE Trans. on Electrical Insulation*, vol. EI-19(5), pp. 453-474, Oct. 1984.

[Peth87-1] R. Pethig, "Dielectric properties of body tissues," *Clin. Phys. Physiol. Meas.*, vol. 8(A), pp. 5-12, 1987.

[Peth87-2] R. Pethig, D.B. Kell, "The passive electrical properties of biological systems: their significance in physiology, biophysics, and biotechnology," *Phys. Med. Biol.*, vol. 32(8), pp. 933-970, 1987.

[Pij87] N. Pijsl, B. De Bruyne, Coronary Pressure 2nd ed., Kluwer Academic, Netherlands, 2000.

[Pom92] M.Pompili, C. Mazzetti, E.O. Forster, "Partial Discharge Distrubutions in Liquid dielectrics," *IEEE Trans. on Electrical Insulation*, 27(1), pp. 99-105, 1992.

[Prev08] P.S. Prevey, "X-ray diffraction residual stress techniques," *Metals Handbook,* 10. Metals Park: American Society for Metals, pp. 380-392, 1986. Viewed Dec 30 2008 at http://www.lambdatechs.com/html/resources/200.pdf

[Prod99] C. Prodan, E. Prodan, "The dielectric behaviour of living cell suspensions," *J. Phys. D: Appl. Phys.*, vol. 32, pp. 335-343, 1999.

[Que 04] L. Que, K. Udeshi, J. Park, Y.B. Gianchandani, “A bi-stable electro-thermal RF switch for high power applications,” *IEEE MEMS* 2004, pp. 797-800.

[Qiu04] J. Qiu, J.H. Lang, A.H. Slocum, “A curved-beam bistable mechanism,” *JMEMS* vol. 13(2), pp. 137-147, Apr. 2004.

[Rao07] P.N. Rao, D. Kunzru, “Fabrication of microchannels on stainless steel by wet chemical etching,” *J. Micromech. Microeng.*, vol. 17, pp. N99-N106, 2007.

[Rich05] M.T. Richardson and Y.B. Gianchandani, “A Passivated Electrode Batch μEDM Technology for Bulk Metal Transducers and Packages," *Proc. of IEEE Sensors 2005*, pp. 219-222.

[Rich06A] M.T. Richardson, Y.B. Gianchandani, D.S. Skala, “A parametric study of dimensional tolerance and hydrodynamic debris removal in micro-electro-discharge machining,” *Proc of IEEE MEMS 2006*, pp. 314-317.

[Rich06B] M.T. Richardson, R. Gharpurey, Y.B. Gianchandani, “Wireless Sensing of Discharge Characteristics for Quality Control in Batch Mode Micro-Electro-Discharge Machining,” *Solid State Sensors and Actuators Workshop Hilton Head 2006,* pp. 404-407.

[Rich08] M.T. Richardson, Y.B. Gianchandani, “Achieving, precision in high density batch mode micro-electro-discharge machining,” *J. Micromech. Microeng.*, vol. 18, pp. 1-12, 2008.

[San07] N. Sanner, N. Huot, E. Audouard, C. Larat, J.-P. Huignard “Direct ultrafast laser micro-structuring of materials using programmable beam shaping,” *Optics and Lasers in Engineering*, vol. 45(6), pp. 737-741, 2007.

[Scha02] M. Schaefer, W. Gross, J. Ackemann, M.M. Gebhard, “The complex dielectric spectrum of heart tissue during ischemia,” *Bioelectrochemistry*, vol. 58, pp. 171-180, 2002.

[Schn00] U. Schnakenberg, P. Walter, G. Vom Bogel, C. Kruger, H.C. Ludtke-Handjery, H.A. Richter, W. Specht, P. Ruokonen, W. Mokwa, “Initial investigations on systems for measuring intraocular pressure,” *Sensors and Actuators*, vol. 85, pp. 287-291, 2000.

[Schn05] R. Schlierf, M. Gortz, T.S. Rode, W. Mokwa, U. Schnakenberg, K. Trieu, “Pressure sensor capsule to control the treatment of abdominal aorta aneurisms,” *Proc. IEEE Solid-State Sensors, Actuators and Microsystems Conf.*, vol. 13, pp. 1656- 1659, 2005.

[Schul01] H.P. Schulze, M. Lauter, G. Wollenberg, M. Storr, W. Rehbein, "Investigation of the pre-ignition stage in EDM," *Proc. of 13th Int. Symp. on Electromachining*, pp. 141-152, May 2001.

[Schum04] B.M. Schumacher, "After 60 years of EDM the discharge process remains still disputed," J. Materials Proc. Tech., 149, pp. 376-381, 2004.

[Schw83] H.P. Schwan, "Electrical properties of blood and its constituents: alternating current spectroscopy," *Blut.*, vol. 46(4), pp. 185-197, 1983.

[Schw92] R.S. Schwartz, K.C. Huber, J.G. Murphy, et al. "Restenosis and the proportional neointimal response to coronary artery injury: results in a porcine model," *J Am Coll Cardiol,* vol. 19:267–74, 1992.

[Schw99] D. Schwartzman, I.Chang, J.J. Michele, M.S. Mirotznik, K.R. Foster, "Electrical Impedance Properties of Normal and Chronically Infarcted Left Ventricular Myocardium," *J. of Interventional Cardiac Electrophys.*, vol. 3, pp. 213-224, 1999.

[Schw04] R.S. Schwartz, N.A. Chronos, R. Virmani, "Preclinical restenosis models and drug-eluting stents: still important, still much to learn," *J. American College of Cardiology*, vol. 44(7), pp. 1373-85, 2004.

[Sen02] S.D. Senturia, Microsystem Design, 2nd ed. Kluwer, pp. 222-226, 2002.

[Serr98] P.W. Serruys, B.J. Rensing, Handbook of coronary stents, 4th ed., Martin Dunitz, Florence, KY 1998.

[Serr05] P.W. Serruys, A.H. Gershlick, Handbook of Drug Eluting Stents, Taylor and Francis, Boca Raton, FL 2005.

[Sest04] A.M. Sesterhenn, H-J. Wagner, H. Alfke, J.A. Werner, B.M. Lippert, "Treatment of benign tracheal stenosis utilizing self-expanding nitinol stents," *Cardiovascular Interventional Radiology,* vol. 27, pp. 355-360, 2004.

[Sha97] P. Shankar, V.K. Jain, T. Sundararajan, "Analysis of spark profiles during EDM process," *Machining Science and Technology*, vol. 1(2), pp. 195-217, 1997.

[Shi06] Y. Shimamura, K. Udeshi, L. Que, J. Park. Y.B. Gianchandani, "Impact behavior and energy transfer efficiency of pulse-driven bent beam electrothermal actuators," *JMEMS*, vol. 15(1), pp. 101-110, 2006.

[Slag92] C.J. Slager, A.C. Phaff, C.E. Essed. N. Bom, J.C.H. Schuurbiers, P.W. Serruys, "Electrical impedance of layered atherosclerotic plaques on human aortas," *IEEE Trans. on Biomed. Engin.*, vol. 39(4), pp. 411- 419, Apr. 1992.

[Sma09] http://www.smaltec.com/ viewed Jan. 29, 2009.

[Son94] J.S. Soni, "Microanalysis of debris formed during rotary EDM of titanium alloy (Ti 6Al 4V) and die steel (T 215 Cr12)," *Wear Journal*, 177, pp. 71-79, 1994.

[Stam00] J. Stampfl, R. Leitgeb, Y-L Cheng, F.B. Prinz, "Electro-discharge machining of mesoscopic parts with electroplated copper and hot-pressed silver tungsten electrodes," *J. Micromech. Microeng*., 10, pp. 1-6, 2000.

[Ste07] C.A Steeves, Y.L. Young, Z. Liu, A. Bapat, K. Bhalerao, A.B.O. Soboyejo, W.O. Soboyejo, "Membrane Thickness Design of Implantable Bio-MEMS Sensors for the In-Situ Monitoring of Blood Flow," *J. Mater. Sci.: Mater. Med.*, vol. 18, pp. 25-37, 2007.

[Stil02] D.K. Stiles, B.A. Oakley, "Simulation of electrode impedance and current densities near anatherosclerotic lesion," *Proc. of IEEE EMBS Microtech. Med. Biol.*, pp. 57-61, 2002.

[Stil03-1] D.K. Stiles, B.A. Oakley, "Comparison of conformal and nonconformal meshes in the electromagnetic simulation of atherosclerotic lesions," *Proc. of IEEE EMBS*, pp. 3005-3008, 2003.

[Stil03-2] D.K. Stiles, B.A. Oakley, "Simulated characterization of atherosclerotic lesions in the coronary arteries by measurement of bioimpedance," *IEEE Trans. on Biomed. Engin.*, vol. 50(7), pp. 916-921, Jul. 2003.

[Stil05] D.K. Stiles, B.A. Oakley, "Four-point electrode measurement of impedance in the vicinity of bovine aorta for quasi-static frequencies," *Bioelectromagnetics*, vol. 26, pp. 54-58, 2005.

[Ston09] G.G. Stoney, "The tension of metallic films deposited by electrolysis," *Proc. of the Royal Soc. of London, Series A*, vol. 82(553), pp. 172-175, 1909.

[Suro87] A. Surowiec, S.S. Stuchly, L. Eidus, A. Swarup, "In vitro dielectric properties of human tissues at radiofrequencies," *Phys. Med. Biol.*, vol. 32(5), pp. 615-621, 1987.

[Tak02] K. Takahata and Y.B. Gianchandani, "Batch mode micro-electro-discharge machining," *J. MEMS*, 11(2), pp. 102-110, 2002.

[Tak03] K. Takahata, A. DeHennis, K.D. Wise, Y.B. Gianchandani, "Stentenna: A Micromachined Antenna Stent for Wireless Monitoring of Implantable Microsensors," *IEEE Conf. EMBS*, 2003, pp. 3360-3.

[Tak05] K. Takahata, *Batch Manufacturing Technology Based on Micro-Electro-Discharge Machining and Application to Cardiovascular Stents*, PhD Dissertation, University of Michigan, 2005.

[Take96] M. Takeuchi, T. Kubono, "Experiment on the radiated magnetic field caused by a breaking arc," *IEICE Trans. Commun.*, vol. E79-B(4), pp. 503-508, 1996.

[Tha08] O. Thao, S.S. Joshi, "Analysis of heat affected zone in the micro-electric-discharge machining," *Int. J. Manuf. Tech. and Management,* vol. 13(2,3,4), pp. 201-213, 2008.

[Tim59] S. Timoshenko, S. Woinowsky-Krieger, Theory of Plates and Shells, *Mcgraw-Hill*, 1959.

[Tob96] R. Tobazeon, "Electrohydrodynamic behaviour of single spherical or cylindrical conducting particles in an insulating liquid subjected to a uniform DC field," *J. Phys. D: Appl. Phys*., 29, pp.2595-2608, 1996.

[Tom99] H. Tomita, "Dependence of current and induced voltage due to spark discharge on gap length," *Intl Sym on Emag Compatibility*, pp. 138-141, 1999.

[Treo05-1] E.F. Treo, C.J. Felice, M.C. Tirado, M.E. Valentinuzzi, D.O. Cervantes, "Hematocrit measurement by dielectric spectroscopy," *IEEE Trans. on Biomed. Engin.*, vol. 52(1), pp. 124-127, Jan. 2005.

[Treo05-2] E.F. Treo, C.J. Felice, M.C. Tirado, M.E. Valentinuzzi, D.O. Cervantes, "Comparative analysis of hematocrit measurements by dielectric and impedance techniques," *IEEE Trans. on Biomed. Engin.*, vol. 52(3), pp. 549-552, Mar. 2005.

[Tsai02] J-Z. Tsai, J.A. Will, S. Hubbard-Van Stelle, H. Cao, S. Tungjitkusolmun, Y.B. Choy, D. Haemmerich, V.R. Vorperian, J.G. Webster, "In-vivo measurement of swine myocardial resistivity," *IEEE Trans. on Biomed. Engin.*, vol. 49(5), pp. 472-483, 2002.

[Ude05] K. Udeshi, M. Richardson, J.-J. Hung, L. Que, G.M. Rebeiz, Y.B. Gianchandani, "A dual-EDM reverse damascene process for RF switches and other bulk devices," *IMECE*, Nov. 2005.

[Ude06] K. Udeshi, *On chip high voltage generation using mechanical oscillators*, University of Michigan Thesis Dissertation, pp. 88-114, 2006.

[Ude07] K. Udeshi, Y.B. Gianchandani, "A DC-powered high-voltage generator using a bulk Pt-Rh oscillating micro-relay," *IEEE Transducers 2007*, pp. 1151-1154.

[Ugu81] A.C. Ugural, Stresses in plates and shells, *McGraw-Hill*, 1981.

[Viss89] K.R. Visser, "Electric properties of flowing blood and impedance cardiography," *Annals of Biomed. Engin.* Vol. 17, pp. 463-473, 1989.

[Viss92] K.R. Visser, "Electric conductivity of stationary and flowing human blood at low frequencies," *Med. & Biol. Eng. & Comput.*, vol. 30, pp. 636-640, 1992.

[Wil91] P.F. Wilson, "Fields radiated by electrostatic discharges," *IEEE Trans. on Electromagnetic Compatibility*, vol. 33(1), pp. 10-18, Feb. 1991.

[Wit01] P.J. Withers, H.K.D.H. Bhadeshia, "Residual stress part 1 – measurement techniques," *Materials Science and Technology*, vol. 17, pp. 355-365, Apr. 2001.

[Yeo99A] S.H. Yeo and L.K. Tan, "Effects of ultrasonic vibrations in micro-electro-discharge machining of microholes," *IOP J. Micromech. Microeng.*,Vol 9, pp. 345-352, 1999.

[Yeo99B] S.H. Yeo, L.K. Tan, "Effects of ultrasonic vibrations in micro electro-discharge machining of microholes," *J. Micromech. Microeng*., 9, pp. 345-352, 1999.

[Yeo04] S.H. Yeo, K.H. Tan, "A novel approach in microfoil bending using an electrodischarge machine," *Proc. Instn Mech. Engrs.*, vol. 218 part B: J. Engineering Manufacture, pp. 1403-1407, 2004.

[Yos08] Y. Yoshihata, N. Binh-Khiem, A. Takai, E. Iwase, K. Matsumoto, I. Shimoyama, "Scanning micromirror using deformation of a parylene-encapsulated liquid structure," *Proc. of IEEE MEMS 2008*, pp. 770-773.

[You02] W.C. Young, R.G. Budynas, Roark's formulas for stress and strain 7th ed., McGraw Hill, 2002.

[Yu02] Z.Y. Yu, K.P. Rajurkar, H. Shen, "High aspect ratio and complex shaped blind micro holes by Micro EDM," *Annals of CIRP*, 50(1), pp. 359-362, 2002.

[Zha04] Y. Zhao, X. Zhang, X, Liu, K. Yamazaki, "Geometric modeling of the linear motor driven electrical discharge machine (EDM) die-sinking process," *Int. J. of Machine Tools & Manufacture*, 44, pp. 1-9, 2004.

[Zhao04] Y. Zhang, Q. Ren, Y-P. Zhao, "Modelling analysis of surface stress on a rectangular cantilever beam," *J. Phys. D: Appl. Phys.*, vol. 37, pp. 2140-2145, 2004.

[Zhan04] Q.H. Zhang, J.H. Zhang, S.F. Ren, J.X. Deng, X. Ai, "Study on technology of ultrasonic vibration aided electrical discharge machining in gas," *J. Materials Proc. Tech*., 149, 640-644, 2004.

[Zhang94] Y.Zhang, K.D. Wise, "An ultra-sensitive capacitive pressure sensor with bossed dielectric diaphragm," *Solid State Sensor and Actuator Workshop*, June 1994, pp. 205-208.